Electrical and Magnetical Modeling of Inductive Coupled Power Transfer Systems

PAR

Christophe Bruno AUVIGNE

EPFL

ÉCOLE POLYTECHNIQUE
FÉDÉRALE DE LAUSANNE

Suisse
2015

A la mémoire d'Idris Hirsch
(1991-2015)

Tout est provisoire : L'amour, l'art, la planète Terre, vous, moi
La mort est tellement inéluctable qu'elle prend tout le monde par surprise.
Comment savoir si cette journée n'est pas la dernière ?
On croit tous avoir le temps
— Idris Hirsch

C'est une triste chose de penser que la nature parle
et que le genre humain n'écoute pas
— Victor Hugo

La liberté c'est avoir le choix
— Stéphane Brosse

Nadie nos dijo que fueramos, nadie nos dijo que lo intentaramos,
nadia nos dijo que seria facil, alguien dijo, que somos nuestro sueño,
que si no soñamos, estamos muertos.
— Kilian Jornet

En Novembre, au salon d'l'auto, Ils vont admirer par milliers
L'dernier modèle de chez Peugeot, Qu'ils pourront jamais se payer
— Renaud

Pour un phare un peu amoché Ou pour un doigt tendu bien haut
Y'en a qui vont jusqu'à flinguer Pour sauver leur autoradio
— Renaud

La charpente a l'air solide mais le bois est sec
Un incendie n'en ferait qu'une bouchée de pain sec
— Médine

Remerciements

Je tiens à profiter de ces quelques lignes pour remercier toutes les personnes ayant permis le déroulement des quatre années de travail de thèse dans les meilleures conditions.

Tout d'abord, je remercie tout particulièrement Yves qui m'a permis de travailler durant ces quatre années sur mon sujet de prédilection, et, sans qui ce travail n'aurait pas été possible. Je remercie aussi mes parents et ma famille pour m'avoir constamment soutenu durant toutes ces longues années d'études. Sans tout ce soutien, cet aboutissement aurait été totalement impossible.

Je tiens également à remercier Dimitrios, Yann et David de Schneider-electric. Ces 2 ans de collaborations, ont largement enrichi ce travail. Tout d'abord, partager avec eux deux jours de travail au sein de leur entreprise m'a permis de m'inspirer de leur goût pour le travail avec une rigueur exemplaire. Par ailleurs, les multiples discussions techniques, dont certaines animées, m'ont permis d'aiguiser mon sens critique.

Je tiens aussi à remercier tous les collègues du laboratoire, ayant permis le déroulement de ce travail dans une ambiance très agréable. En commençant par Paolo, qui a supporté de superviser mon travail, en étant contraint de "se taper" des pages d'équations, de survivre en cotoyant mon bureau et ma table d'expérimentation d'entropie maximale. Merci également à Yoan, qui a relu avec le plus grand soin les différents documents rédigés. Son efficacité et son sens critique aiguisé sont toujours très impresionant. Merci aussi à Christian, toujours plein d'idées géniales de prototypage.

Je remercie également tous les doctorants que j'ai eu la chance de croiser durant ces quatre années : Christophe, pour son aide et ses idées précieuses; Daniel, qui n'a pas hésité à mettre à disposition son imprimante 3D personnelle pour réaliser certains prototypes; Shi Dan, Florian, Johnatan, RBesuche pour avoir partagé le bureau; Pascal pour les parties de fléchettes; Cécile, toujours présente pour donner un précieux coup de main; Xichang, incollable sur le langage java; Jasha, pour un apprentissage accéléré des insultes italiennes; et enfin les nouveaux collègues, Taira et Jiantao.

Merci également à toute les personnes externes ayant relu et apporter leur compétance sur ce manuscrit : Xavier, Martin et Christian.

Enfin, je tiens tout particulièrement à remercier Lisa, qui, grâce à son sens logique et critique très développé, m'a permis d'ouvrir un horizon plus large sur ce travail.

Neuchatel, 12 janvier 2015   C. A.

Abstract (English/Français)

Nowadays, there is a very high number of electronic devices with different ranges of power. Desktop peripherals and cellphones are an example of widely used low power devices. Contactless power transfer is useful to supply or recharge these devices without any physical link. Their lifetime can be increased because wires are a source of dysfunction. Contactless power transfer is also very useful in supplying rotating parts. Indeed, the brushes typically used for this purpose are impractical for high speed applications and are also a source of dysfunction. In recent years, the development of electric vehicles became a great opportunity for contactless power transfer applications. The batteries of these vehicles have a limited autonomy which makes the charging process very important. Contactless power transfer has two main advantages compared to wired charging. First, security is increased for the user because he does not need to handle any cable transporting high voltage. Also, the reliability of the system is increased due to the absence of these cables. The second advantage is the possibility for dynamic contactless charging. For example, a vehicle being recharged while moving along a designated stretch of road.

By taking as a starting point, the contactless battery charging for an electric vehicle, this work addresses contactless power transfer using inductive couplers. The modelling proposed in the scope of this work is available for different ranges of power. However, special attention is given to crucial points for high power applications, which are the efficiency of the system and the radiated magnetic field. Indeed, the efficiency in high power transfer is a crucial point for ecological and thermal dissipation reasons. The radiated field must be limited to meet magnetic radiation guidelines and to ensure the safety of users.

The inductive coupled power transfer (ICPT), similar to a conventional transformer, is made of two magnetically coupled coils. The first one, called the primary coil, is supplied with an alternating current, which induces a voltage in the secondary coil. The amplitude of the induced voltage in the secondary coil is a function of the magnetic coupling factor and the operating frequency. The main difference between conventional transformers and inductive couplers is the value of the magnetic coupling. Indeed, the distance between the coils is larger for inductive couplers, and the magnetic field lines are not guided by a ferromagnetic material as in the case in conventional transformers. As a result, such a system is also called an "air-transformer".

To obtain high performance in spite of a very low coupling factor (typically 0.1 compared to 0.9), compensation capacitances are inserted into the system. They compensate the very low power factor due to the magnetisation of the inductances. The different compensation topologies

Abstract

are studied and compared in detail in this work. They determine the load characteristic, the frequency response and the values of the voltages and currents in the coils. A novel compensation methodology is proposed and compared to the existing one. It aims to simplify the transformer's control instead of maximizing the efficiency.

When a conductive plate is close to the transformer, Eddy currents are induced leading to the generation of Joule losses. The system efficiency is thus decreased and thermal dissipation becomes an issue. In this case, adding magnetic shielding to the structure is very efficient. A modelling of these effects is performed and several shielding topologies are proposed. An optimisation of the shielding geometry, based on genetic algorithms, is also undertaken.

In addition, it is assumed for the transformer model, built upon an equivalent electric circuit (EEC), that the electrical load is a resistance. However, the response of the system is modified when a battery is directly connected to the secondary part of the transformer. Modelling of this phenomenon using a non-linear resistance is performed and this non-linear behaviour is then used to simplify the generation of the battery load profile.

As a result, the functional demonstrators realised in the scope of this work are presented. The theoretical aspects developed during the modelling portion are compared to practical measurements. The differences are analysed and the domain of validity of the mathematical models are discussed.

Keywords : *Bifurcation phenomenon, Capacitive compensation, Contactless battery charger, Contactless power transfer, Finite element modelling, Inductive coupler, Optimisation, Resonant transformer, Shielding*

Résumé

De nos jours, le nombre d'appareils électroniques et électriques de diverses puissances ne cesse de s'accroître. Dans le domaine des basses puissances, nous pouvons citer notamment les périphériques d'ordinateurs ainsi que les téléphones portables. La transmission d'énergie sans contact permet d'alimenter ou de recharger ces périphériques en se passant des innombrables câbles d'alimentation. Ceci permet d'augmenter la durée de vie des appareils d'une part car les câbles sont sources d'usures prématurées, et de permettre une utilisation plus agréable d'autre part. Le transfert d'énergie sans contact trouve aussi sa place pour l'alimentation de parties tournantes. En effet, l'utilisation de balais est aussi sujette à une usure prématurée et peu pratique dans le cas de rotation à haute vitesse. L'apparition des véhicules électriques au cours de ces dernières années motive d'autant plus la recherche dans le transfert d'énergie sans contact, pour de plus hautes puissances. En effet, l'autonomie des batteries des voitures électriques étant limitée, la recharge de ces dernières est un point important. L'utilisation de la transmission d'énergie sans contact possède deux avantages. Le premier consiste à se passer de câbles de recharge, augmentant d'une part la sécurité de l'utilisateur n'ayant plus besoin de manipuler un câble sous haute tension et d'autre part la robustesse du système en évitant l'usure de ces mêmes câbles. Le second avantage est que la recharge sans contact permet une recharge dynamique de véhicules. Dans le même concept que les caténaires sur les transports en communs urbains, le véhicule peut être rechargé sans contact sur certains tronçons de routes prévus à cet effet.

En prenant comme point de départ la recharge sans contact d'un véhicule électrique, ce travail porte sur l'étude du transfert d'énergie sans contact par couplage inductif. Bien que proposant une modélisation générale pouvant s'appliquer à différentes gammes de puissance, une attention particulière est portée sur le rendement du système ainsi que sur le champ magnétique rayonné. Le rendement est primordial pour des raisons écologiques et de problèmes de dissipations thermiques tandis que le champ magnétique rayonné est un point important pour assurer la sécurité de l'utilisateur.

Comme les transformateurs dits "conventionnels", le transfert d'énergie sans contact par couplage inductif est composé de deux bobines magnétiquement couplées entre elles. La première, communément appelée bobine primaire, est alimentée par un courant alternatif. Selon la loi de Lenz, une tension est induite dans la seconde bobine. Une grande différence entre un transformateur conventionnel et de la transmission d'énergie sans contact est la valeur du couplage magnétique. En effet, la distance entre les deux bobines est nettement plus élevée dans le second cas, et les lignes de champ ne sont pas guidées par un matériau

ferromagnétique contrairement au transformateur "conventionnel". Pour cette raison, un tel dispositif est aussi communément appelé "transformateur à air".

Afin d'obtenir de bonnes performances malgré un facteur de couplage très bas (typiquement 0.1 contre 0.9 pour les transformateurs conventionnels), des condensateurs dits de compensation sont ajoutés au système afin d'augmenter un facteur de puissance très bas dû aux champs de fuites. Les différentes topologies de compensations sont étudiées et comparées en détail dans le cadre de ce travail. Le gain du transformateur, la caractéristique en charge, la réponse en fréquence ainsi que les valeurs de tensions et courant dans les bobines sont des paramètres dépendants de la topologie de compensation. Une nouvelle méthodologie de compensation visant à simplifier le contrôle du transformateur est aussi proposée dans le cadre de ce travail. Cette dernière est comparée à la méthodologie existante visant à maximiser le rendement.

Par ailleurs, lorsqu'un matériau conducteur est présent à proximité du transformateur, des courants de Foucault sont induits dans ce dernier. En plus de générer des pertes dans la pièce (principe de chauffage par induction) et donc de baisser le rendement du transformateur, les caractéristiques de ce dernier sont totalement modifiées. Dans ce cas, l'ajout d'un blindage correctement dimensionné dans le système se révèle particulièrement efficace. Une modélisation de ces effets est effectuée et plusieurs topologies de blindages sont proposées. Une optimisation de la géométrie du blindage basée sur les algorithmes génétiques est également réalisée.

De plus, la modélisation des transformateurs par circuit électrique équivalent suppose que la charge électrique se comporte comme une résistance. Cependant, la réponse du système est complètement différente lorsqu'une batterie est directement connectée au transformateur. Une modélisation de ce phénomène par une résistance non-linéaire est entreprise. Cet effet non-linéaire est ensuite utilisé afin de simplifier le contrôle du cycle de charge de la batterie. Enfin, les réalisations dans le cadre de ce travail sont présentées. Les aspects théoriques développés au cours de la modélisation sont comparés aux mesures pratiques. Les différences obtenues sont analysées et les limites des différents modèles mathématiques développés sont présentées.

Mots clés : *Accordage, Blindages magnétiques, Chargeur de batterie sans fil, Compensation capacitive, Couplage inductif, Modélisation par éléments finis, Optimisation, Phenomène de bifurcation, Transfert d'énergie sans contact, Transformateur à double résonance*

Contents

Contents

List of Figures

List of Tables

1 Introduction

Contents

1.1 Introduction on contactless power transfer

Contactless power transfer consists in transferring electrical energy from a power supply to a load without any physical link. Such a system is basically made of two parts. The first one is generally called the transmitter or the primary part, and transmits the energy from the power supply to the second part, called the receiver. Since the medium between these two parts is generally insulated, the electrical energy must be converted for the transfer. The first experiment realised on contactless power transfer capability was done by the scientist Nicola Tesla in the 1900's using electromagnetic waves [40]. The emitter was the well-knwon Wardenclyffe tower, illustrated in Fig. 1.1, the transferred power was 300 kW and the exciting frequency was 150 kHz.
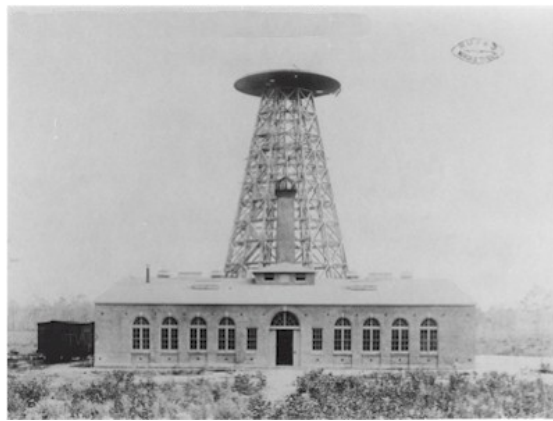
Figure 1.1: Picture of the Tesla Wardenclyffe tower used for the first contactless power transfer experiment [40]

The first photovoltaic cell was built around 1950 and the first solar power satellite was proposed a few years after, in 1958. It has demonstrated the possibility to convert light into electric energy. The microwave power transmission started with W.C Brown's experiments in 1963 [7]. For this demonstration, several hundred watts were transferred over eight meters with an operating frequency of 2.45 GHz. One year after this experiment, the now celebrated microwave-powered small helicopter was built [6]. The emitted power was 5 kW while the received power was only 280 W. The main historical experiments of contactless power transfer are summarized in Fig. 1.2.

Independently of the technology used, contactless power transfer has many advantages because it allows to transmit electrical power without any physical link. First of all, the absence of any wire between the power supply and the load increases the security of the user for high voltage operation, because there is no cable between these two parts. The lifetime is also enhanced because power wires are very often subject to dysfunction due to the mechanical stress imposed on them. Electronic devices such as peripherals for desktop computers and cellphones are always subject to be recharged. Using contactless power transfer, the charging procedure is easier as the user does not need to plug any wire. Moreover,
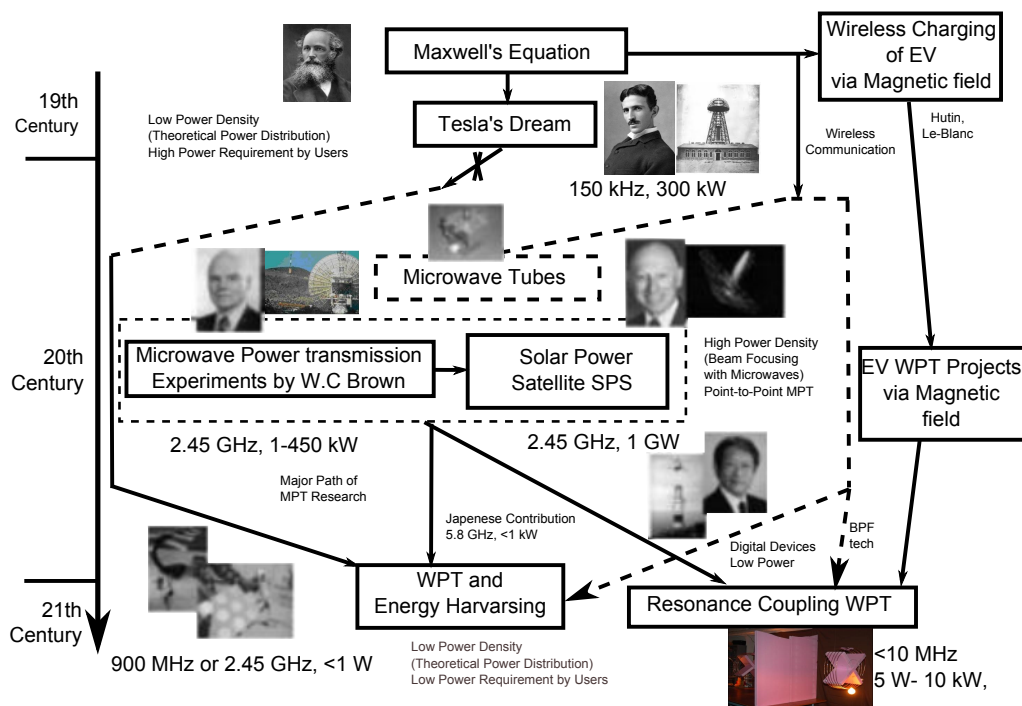
Figure 1.2: Summary of the wireless power transfer history [58]

it is also a suitable solution to power rotating parts since the use of brushes are subject to dysfunction. Moreover, using brushes is subject to the generation of particles. This causes trouble for special environments, such as flammable environments and clean rooms. In the field of electric transportations, contactless power transfer has also a great potential for high power range. Indeed, the safety of the user is increased because he does not need to plug any cable transporting high voltage. Moreover, dynamic contactless charging allows the vehicle to be recharged while moving on adapted parts. The different aspects of the existing technologies for contactless power transfer purpose are presented below.

Photonic power transfer allows transferring of electrical power from a light source (e.g a laser) to a photovoltaic receiver. High power over very large distance can be achieved (up to 34 kW over a distance of 1.5 km). However, the required installations are very complex and expensive [16]. For these reasons, applications of this technology are mainly dedicated to spacecraft platforms [53, 55].

Acoustic power transfer is another way to transfer power. The principle is illustrated in Fig. 1.3a. An acoustic transducer creates a pressure wave from the electrical power supply. It is propagated through a medium (such as air) to a receiver which converts the wave into electrical power. Unlike the inductive couplers developed below, this technology is not affected by external magnetic fields. However, the efficiency of the power transferred is lower than inductive coupler, except for long distances between the emitter and the receiver [33]. This technique is mostly used for biomedical purpose (low power transmission < 1 W). It is also used for

mid-range power ($1\,\mathrm{kW}$) in presence of metal parts where inductive coupler performances are limited [25, 39].

Capacitive coupler is also a way to transfer power using electric field. Two sets of parallel plates form two capacitances which are used to transfer power. Such a system is described in Fig. 1.3b. This is widely used for low power range ($1-50\,\mathrm{W}$) [11] and relatively small distance (generally less than $1\,\mathrm{mm}$) between the electrodes. Indeed, the very small capacitance made by the electrodes leads to a very high voltage between the electrodes which is subject to air breakdown. Since the power transfer is achieved by the electrical field between the electrodes, an advantage of this technology is to be able to transfer power through a metal barrier [41]. Moreover, it is not affected by any external magnetic field. It is used in synchronous machines [42], low power contactless charging ($5\,\mathrm{W}$) [36], medical devices power supply ($30\,\mathrm{W}$) [78] ,...

Another well-known used technology, called magnetic resonance is very suitable for long distance transmission (up to $10\,\mathrm{m}$). A primary coil is supplied by a high frequency current (generally between $5\,\mathrm{MHz}$ and $15\,\mathrm{MHz}$). Unlike the inductive coupling principle, the coupling between the transmitter and the receiver is achieved by both the magnetic field and the electric displacement field. This is due to the operating frequency which is higher than the range used for inductive couplers (generally between $20\,\mathrm{kHz}$ and $200\,\mathrm{kHz}$) and lower than the one used for RF transmission (generally $2.4\,\mathrm{GHz}$). The transmission is thus possible even if the receiver is not aligned to the transmitter. The main drawback of this technology is that the maximum admissible field value is not yet known to ensure the safety of the users. This technology is used to supply the Radio Frequency IDentification (RFID) systems. For such an implementation, the distance is generally small (a few centimeters) but this standard also cover transmissions over 12 meters [30]. The probably most known company since 2007 that uses this technology is WiTricity [72].

Inductive coupler is a widely used technology to transmit power. The principle is the same as the conventional transformers. It consists in injecting an alternative current into an emitter coil (the primary coil) which creates a magnetic field. The magnetic flux through the secondary coil induces a voltage. The main difference between a classical transformer and an inductive coupler is the leakage flux. It can be very often neglected in a conventional transformer. Because of its relatively high airgap and the absence of magnetic core, the leakage is not negligible in most inductive couplers. In order to compensate the power transfer capability of the coupler, the frequency is generally increased from $50\,\mathrm{Hz}$ (frequency generally used for the conventional transformers) to $10\,\mathrm{kHz} - 10\,\mathrm{MHz}$. However, increasing the operating frequency decreases the power factor of the system since it increases the value of the reactances. Compensation capacitances are generally inserted in this purpose.

1.2   Structure of this work

This work focuses on contactless power transfer using the inductive couplers technology. It is structured into seven chapters which are presented below.

(a) Accoustic contactless power transfer principle   (b) Capacitive contactless power transfer principle

(c) Inductive contactless power transfer principle
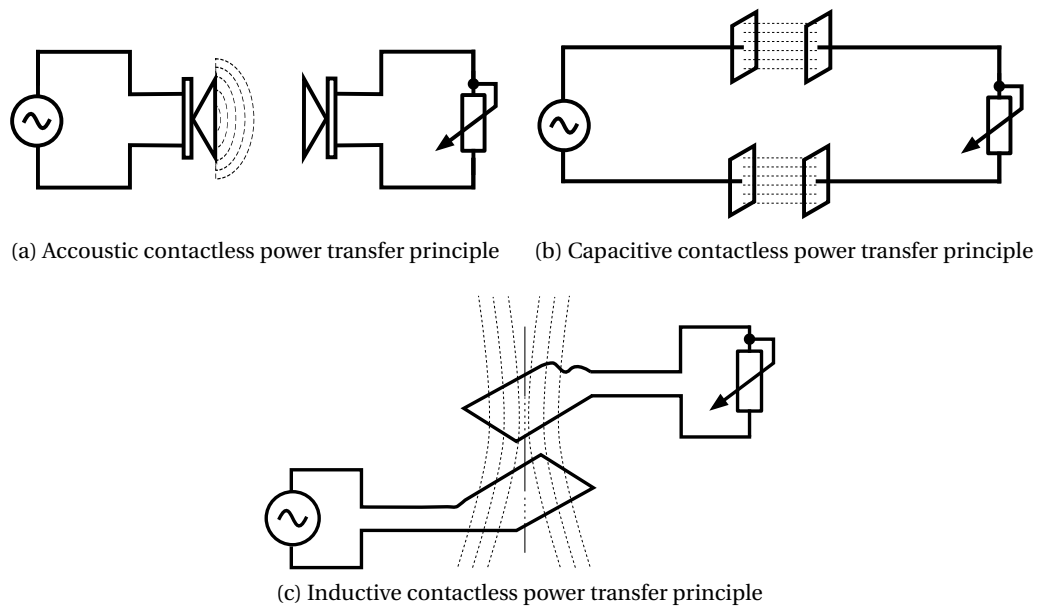
Figure 1.3: Different techniques available for contactless power transfer

- Chapter 2 presents a state of the art of inductive coupled power transfer systems. Different applications, depending on the required power and the topology of the system are detailed and compared.

- Chapter 3 presents a modelling of all the parts which constitute an inductive coupled power transfer. As a first part, the power electronics is presented and modelled. A first-harmonic approximation, very useful for the modelling in this work, is made. The second part of this chapter is dedicated to air-transformers (no conductive or ferromagnetic parts are present near the coupler). The elements of such a coupler are studied and modelled. The third part integrates conductive and/or ferromagnetic parts. New effects appear which can widely change the behaviour of the coupler. In both cases, the different electric equivalent circuit of the transformers are presented. The modelling investigated in this chapter is a very important point of this work because it allows the magnetic and the electrical parts to separate for the future design.

- Chapter 4 introduces the capacitive compensation of the transformer. This is a very critical part of this work since a non-compensated system can lead to very low performances. A proper compensation is essential to increase the transferred power at a maximal efficiency. The different topologies of compensation are introduced, studied in detail and compared. Two methodologies of compensation are proposed. The first one, used in literature, consists in maximizing the efficiency of the transformer. A novel methodology introduced in this work targets to simplify the control of the transformer. Finally, the frequency response of the transformer for the different compensation topologies investigated is computed. General criteria for bifurcation operation are developed.

- Chapter 5 addresses the shielding of the transformer. A preliminary study motivates the need of a proper shielding design combining conductive and ferromagnetic parts. This allows achieving of a good efficiency when one or more conductive plates are close to the transformer. As a second step, a design methodology is proposed. The electric and magnetic parts are design independently, according to given specifications. Several shielding topologies are then studied and compared. As a third step, an optimisation on different shielding geometries based on genetic algorithms is performed. The transformer efficiency is to be maximized while the radiated magnetic field is to be minimized to ensure the safety of the user. The results of this optimisation are presented and discussed.

- Chapter 6 is dedicated to the practical implementations realised in the scope of this work. The first section presents the prototyped resonant inverter. The different aspects, such as the power stage, the power driver, the logic interface and the hardware protections are detailed. After that, a prototype built to validate and evaluate the performances of the novel compensation methodology presented in Chapter 4 is introduced. The measurements are discussed and compared to the theory. Two implementations for contactless battery chargers are also presented in this chapter.

- As a result, chapter 7 draws the conclusions and the perspectives of this work.

2 State of the art

Contents

2.1 Introduction

This chapter presents a large scope of applications for inductive coupled power transfer systems. It is divided into two main parts. The first one is related to lower power transmission (less than 100 watt). In this case, the efficiency is not the most important criterion. However, since theses applications are very often embedded, the specifications require a small geometry, a high misalignment tolerance, a very cheap and basic electronics. The second part addresses "high power" transfer (more than one kW). The coils are generally larger but the efficiency is generally a challenge since the losses have to be dissipated and can be quite important. It can be divided into two main categories. The first one addresses static applications. It means that both primary and secondary parts are standstill. The second one addresses the dynamical applications. It means that the receiver is embedded into a moving parts. For each part, some existing applications are presented and compared.

In both cases, the magnetic field emission generated by the coils could be a problem. First of all, depending on the design, the presence of a conductive or ferromagnetic part close to the transformer may cause troubles. Indeed, it changes the parameters of the transformer and generates additional power losses. Moreover, the magnetic field emission should be limited for safety reasons. The impact of the magnetic field on the human body is beyond the scope of this document. However, additional information can be found in [15, 59].

In order to ensure the functionality between different kinds of consumer peripheral, several standards exist [67]. Since the manufacturer who provides the peripheral is not necessary the same as the one who provides the charge platform, the interoperability between these two elements is an essential point. The different standards normalize the geometry of the coils, provide a range of operating frequency, and a range of the transferred power.

A basic contactless power transfer system is made of two coils (single coil configuration). The first one is the emitter coil in which an alternative current is injected by the power supply. The second one is the receiver coil. In order to increase the misalignment tolerance, to increase the airgap, or to decrease the radiated magnetic field, additional emitters and/or coils can be used. This is called multi-coils configuration. For instance, to increase the distance between the emitter and the receiver, several solutions such as relay resonators and domino loops are studied in [26, 17].

These different concepts introduced in this state of the art are summarized in Fig. 2.1.
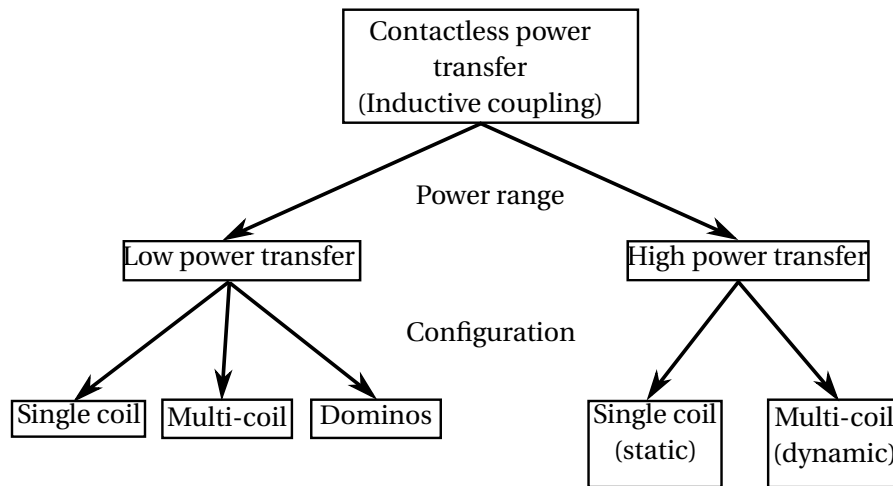
Figure 2.1: Overview of the different introduced concepts

2.2 Low power transmission

The main applications of low power contactless power transfer are desktop peripherals power supply, mobile phones charger platforms and transcutaneous power transfer. This section introduces some of these applications and their associated concepts.

2.2.1 Desktop peripherals supply and mobile phones charger

Contactless supply of desktop peripherals and mobile phones is an application widely investigated. The required transferred power is generally comprised between 1 and 20 W and the distance between the coils is generally small (generally less than a cm).

A contactless mobile phone charger is proposed in [12]. The transmitted power is up to 4 watt and the operating frequency is about 500 kilohertz. The coils are circular with a radius of 35 mm and the distance between each other is about 2 mm. A battery manager is connected to the battery in order to provide a controlled load battery cycle. The peripherals are placed on a "charging zone". The system detects the presence of one or more objects and starts the energy transfer. Since the power is low, the efficiency is not so important. However, the working surface is quite large (for mice and loud-speakers, the table is about 300x300 mm^2 [49]). In order to ensure a good reliability over such a working zone, an array of small primary coils is generally used instead of a large single one (Fig. 2.2). Only the coils under the peripheral are supplied by acting on switches to increase the efficiency and minimize the magnetic field emission. The same implementation is used in [27]. To reduce the radiated magnetic field, another solution consisting in supplying three coils with a phase of 120° is proposed in [62, 63]. Basically, the idea is to create destructive interferences above the secondary part. For this purpose, the primary is made of an array of hexagonal coils, as shown in Fig. 2.3. Although the leakage magnetic flux is smaller using this configuration, the need of a three-phases magnetic

supply turns this system into a complex one. Moreover, the efficiency is decreased due to the need of the additional electronics and the high number of coils to supply.
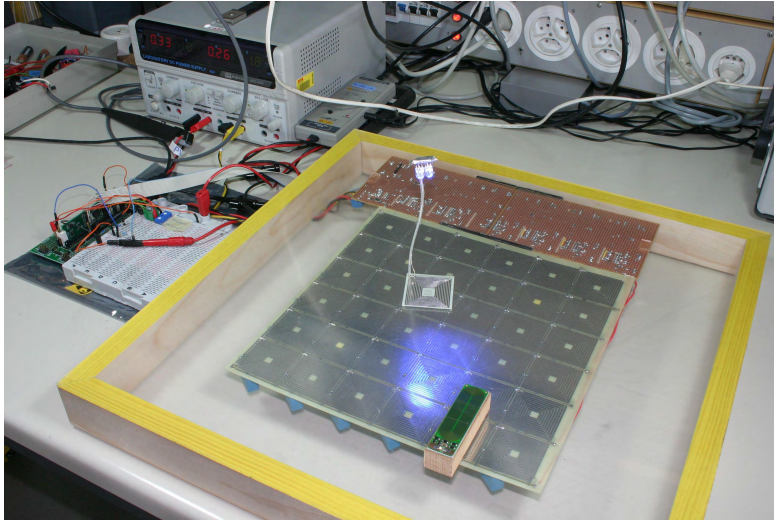
Figure 2.2: Desktop peripherals charger realised in [49]

Several layers of coil arrays can be stacked to obtain a constant magnetic field independently of the position of the secondary part. This is done in [27] for a contactless mobile phone charger. Since the position dependency of the magnetic coupling is smaller, the control of this system is simplified. Firstly, the efficiency is increased due to this effect. Secondly, it is decreased due to the high number coils to supply. The main drawback of this system is its complexity because it requires additional electronics and coils.

2.2.2 Medical applications

Contactless power transfer is widely used for transcutaneous energy transfer (TET) because it allows the physical link to remove between the power supply and the load placed inside the body of the patient. As the displacement of the secondary part is smaller than for desktop

(a) Arrangement of the coils   (b) Prototype realised in [64]
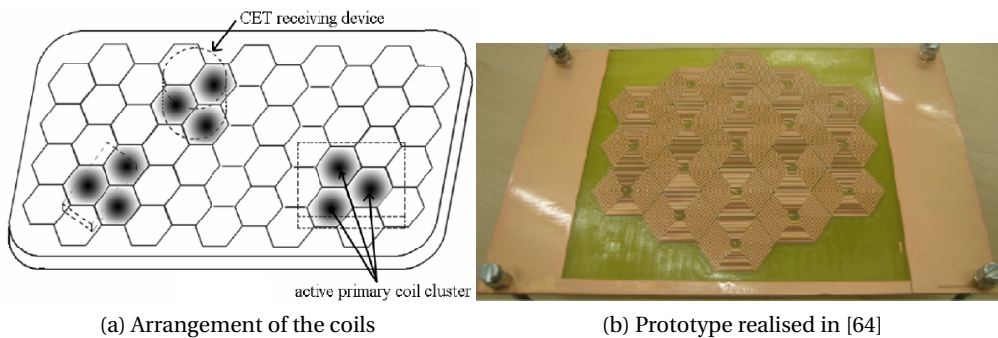
Figure 2.3: Description of the multiphase coil array used in [64]

peripherals, the primary part is generally composed of only one coil. One crucial point is the temperature of the secondary part since it is inside the body of the patient. This is why the acceptable current density in the secondary coil is lower than for other applications.

Contactless power transfer is applied for colic stimulation in [24]. The secondary coil is directly placed inside the body of the patient. The transmitted power is about 0.1 watt and the operating frequency is 600 kilohertz. A particularity of this design is the use of the intrinsic secondary coil capacitance to create the resonance at the operating frequency. This means that no additional capacitance is needed at the receiver side. It leads to two main advantages. Firstly, the embedded electronics is smaller. This is a good advantage because this part is in the body of the patient, so the acceptable volume of the system is limited. Secondly, the losses in the secondary part are reduced because this capacitance is removed. However, the operating frequency is imposed by the intrinsic resonance of the secondary coil. It is higher than the one used for similar applications. The losses in the primary electronics are thus higher, due to this high frequency. Since the transmitted power is low, this is not necessarily a problem.

A contactless power transfer system is proposed in [74] to supply a heart device assistance. The transferred power is 10 watt at 205 kilohertz. In [45, 44], an inductive coupler is designed for artificial heart power supply. Compared to the other applications listed above, the coupling factor is very high ($k \approx 0.7$). The required power is 20 watt for a distance of 5 mm between the coils and the operating frequency is set to 50 kilohertz. The critical point for this implementation is the temperature surge of the coils, which have not to excess 3°C. Moreover, the secondary coil is made of amorphous fibres in order to be flexible.

2.2.3 Drill machine

Another application of contactless power transfer systems is a contactless battery charger for drill machines. In collaboration with the Hilti company, the LAI has developed such a system, which is illustrated in Fig. 2.4. The primary coil is placed in the emitter system. The second one is inserted in the drill machine. A bidirectional communication based on magnetic coupling is ensured between the primary part and the machine to regulate the transmitted power. For this purpose, the magnetic coupling between the power coils and the communication ones is to be minimized. If it is too high, the data transmission can be corrupted. The transferred power is 25 watt and the working frequency is around 100 kilohertz [4].
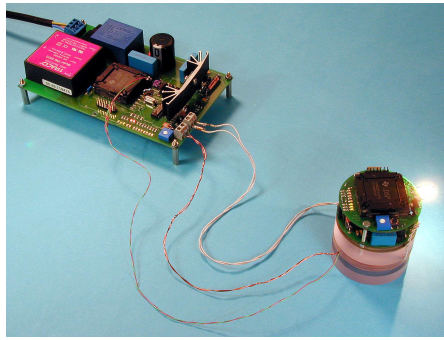
Figure 2.4: Transformer used for a drill machine charger [4]

2.2.4 Existing standards

More and more manufacturers use contactless power transfer to recharge their devices. Standardizations become mandatory in order to have compatible charging devices, as illustrated in Fig. 2.5.

Wireless Charger X   Wireless Charger Y
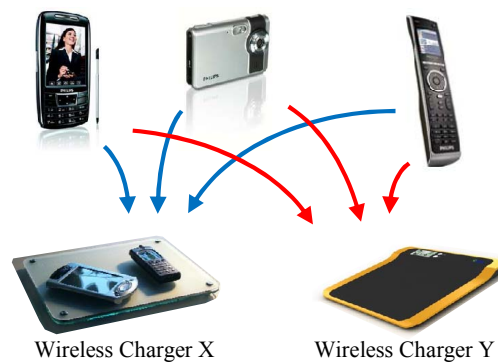
Figure 2.5: Interoperability concept [67]

Since 2008, the probably most known standard for inductive power transfer has been set up by the Wireless Power Consortium company and is called QI [13]. It addresses low power applications (between 0 and 5 watt) for a small distance between the transmitter and the devices (less than 40 mm). This standard is available for three types of transmitter to achieve a good enough coupling factor. The first one is called "guided positioning". The peripheral is aligned to the primary coil. The second one is called "free positioning" with moving coil. The primary coil moves below the receiver in order to ensure a coupling factor in each allowable position of the receiver. The third one is called "free positioning with coil matrix". The transmitter is composed of an array of coils. These three configurations are illustrated in Fig. 2.6.

In the multi-coils configuration, a load detection is performed in order to supply only the coils below the receiver. In order to control the transferred power, an information canal based on

(a) Guided-positioning (b) Free-positioning (multi-coils) (c) Free-positioning
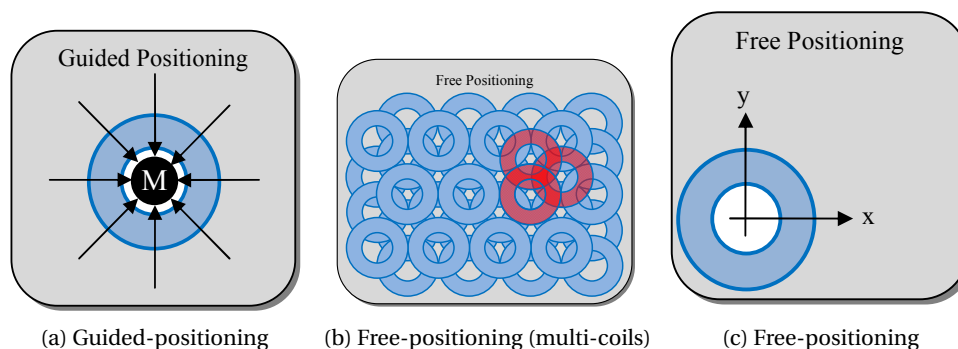
Figure 2.6: Configurations for QI standard [67]

the measurement of the reflected impedance is superimposed to the power transfer canal. The standard also defines the communication protocol between the transmitter and the devices [67]. Nowadays, several smart-phone manufacturers implement this standard, as illustrated in Fig. 2.7.

Another standard called Rezence has been established by the company Alliance for Wireless Power (A4WP) in 2012. Unlike the Qi standard, Rezence supports power transfer up to 50 watt over a distance up to 5 cm [22]. The working frequency is imposed at 6.78 megahertz. This standard uses a smart bluetooth (BLE) for the communication between the transmitter and its device.

The Power Matters Alliance (PMA) is trying to standardize the different standards presented above in order to provide contactless charger in public places.

Figure 2.7: Contactless charger implementing QI standard [51]

2.2.5 Resonant loops

In order to increase the distance between the primary and the secondary coil, resonant loops can be inserted. The principle consists in inserting one or more additional coils between the transmitter and the receiver. These coils are tuned with capacitances in order to maximize the current. In [79], the transferred power is 15 watt and the operating frequency is around

(a) Different configurations   (b) Photo of the practical implementation
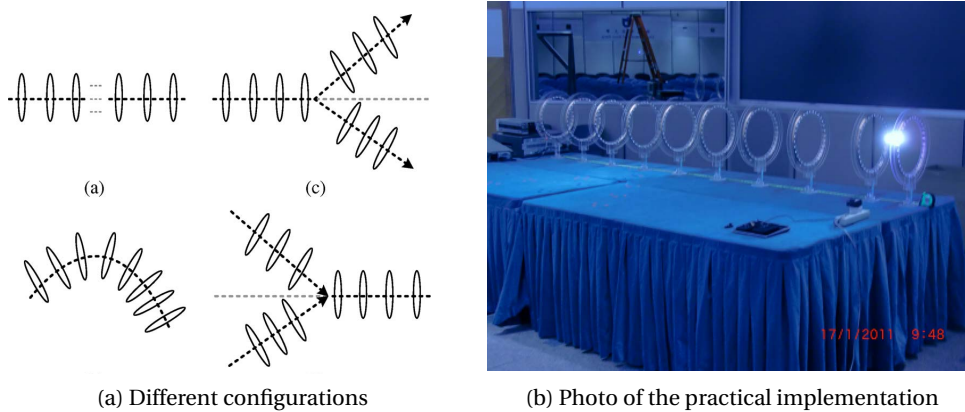
Figure 2.8: Resonant coils [79]

500 kHz. An implementation is illustrated in Fig. 2.8. Although this very elegant solution increases the distance between the primary and the secondary coils, no real application uses this concept in literature.

2.3   High power transmission

Applications using "high power" transmission (larger than one kW) are mainly electric vehicle power supplies, battery chargers and induction cookers. As the transmitted power is important, a high efficiency is required. Indeed, important losses cause problems to dissipate the thermal energy, and are not admissible for ecological reasons. For safety reasons, the magnetic field emission is often limited. The maximal admissible value depends on both the operating frequency and the application. The ICNIRP commission provides more information [29].

The contactless chargers or supplies for the electric vehicle can be divided into two parts. The first one is about static applications. The vehicle is placed in front of the emitter before the charging sequence begins. The second one is about dynamic charging. The vehicle is moving when it is supplied or recharged.

2.3.1   Static Electric vehicle power supply and battery charger

Many researches focus on contactless power supply or battery charger for electric vehicles. The transmitted power is generally comprised between 1 kW and 200 kW and the operating frequency between 20 kHz and 50 kHz. As the electronics is more complex than for low power applications, coil arrays are generally avoided.

For these applications, massive iron parts are very often present close to the transformer (the car itself for example). The efficiency of the power transfer is very low if no shielding is designed because a lot of power is dissipated in these parts. In [56], a shielding composed of

(a) Transformer realised in the university of Saragosse [68]
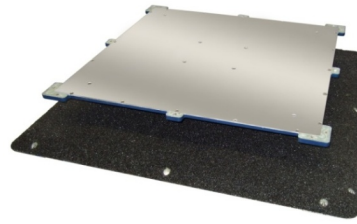
(b) Transformer with shielding realised in [56]

Figure 2.9: Transformers for high power applications

a ferrite plate and an aluminium plate at both primary and secondary side is introduced to reduce these losses. The primary part is larger than the secondary one (the exact dimensions are not given) to increase the misalignment tolerance. In this implementation, the operating frequency is higher than the common one (140 kHz). The system is illustrated in Fig. 2.9b.

In [38], a 3 kW contactless battery charger for electric cars has been realised. Compared to the previous implementations, the distance between the two coils is very low (5 mm). The magnetic coupling factor of the transformer ($k > 0.8$) is very high due to its small airgap and the presence of ferrite pieces. The operating frequency is less than 100 kHz.

In [68], a laboratory of the Saragosse University has realised a 5 kW contactless battery charger. The operating frequency is around 15 kHz. This transformer is realised in the air (no shielding and no solid magnetic circuit). The efficiency obtained is up to 94%. All the losses are contained into the coils since no iron parts are close to the transformer. Its implementation is illustrated in Fig. 2.9a.

In [8], the university of Auckland has proposed a particular coil geometry to increase the misalignment tolerance between the primary and secondary part. It consists in placing the coils around ferrite bars. The receiver is then sensitive to the tangential component of the magnetic field, as shown in Fig. 2.10. This topology is then applied to a 2 kW power supply for electric vehicle. The main drawback of this configuration is that the secondary coil is only sensitive to the tangential component of the magnetic field. Its interoperability is very low because most transmitters use the vertical component. In this way, a generic secondary pad using several coils called "Quadrature Double D with quadrature coil" has been developed by the university of Auckland in [14, 10]. This topology is illustrated in Fig. 2.11.

2.3.2 Dynamic Electric vehicle power supply and battery charger

A widely investigated field of research is the contactless power supply for moving secondary parts (also called "pick-up"). It is also called Roadway Powered Electric Vehicles (RPEVs). In this purpose, many solutions exist in literature.
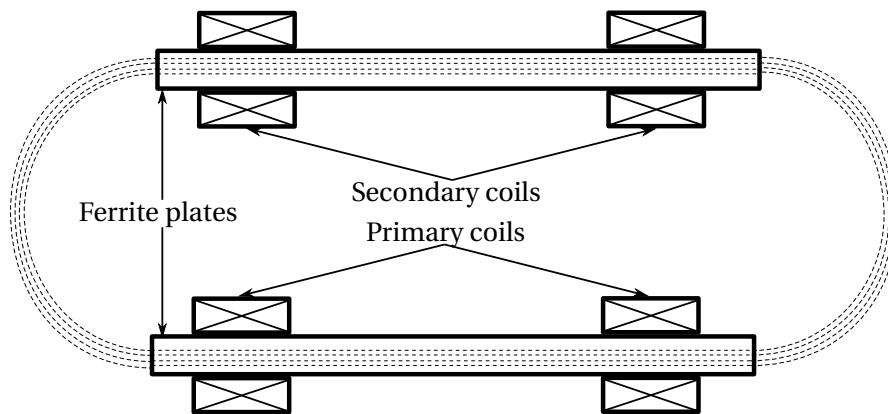
Figure 2.10: Geometry proposed to increase the misalignement tolerance [8]
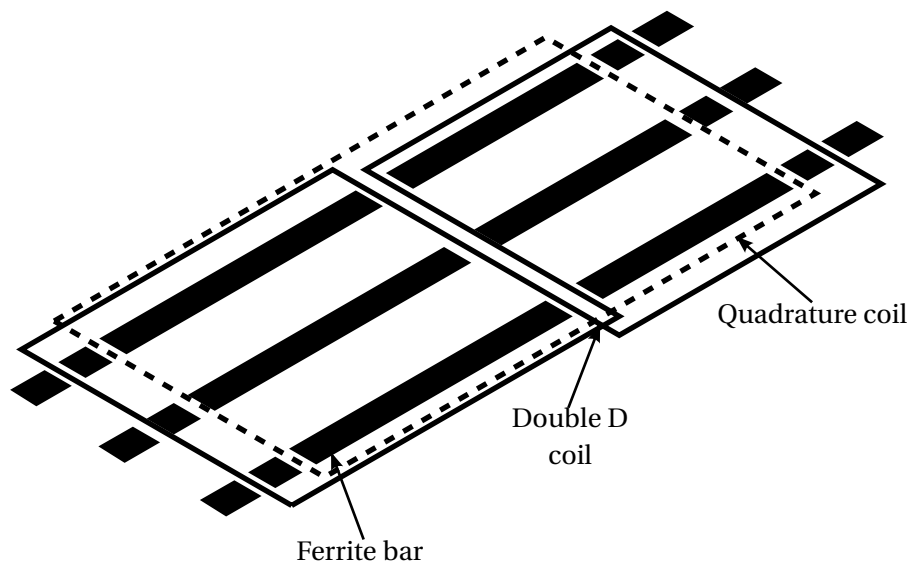
Figure 2.11: Double D with Quadrature coil [10]

A simple solution is to design a very long single coil so that the moving part is always above the primary coil. It is implemented in [52]. In order to increase the power transfer capabilities, the secondary part is made of two coils : one sensitive to the tangential component of the magnetic field and the other one to the normal component. This is illustrated in Fig. 2.12. More primary tracks can be used in order to increase the misalignment tolerance, as done in [35]. This is illustrated in Fig. 2.13. The main problem of this configuration is the interaction between the primary coils. Some special geometries can be adopted to reduce this effect, as investigated in [34]. Fig. 2.14 shows two primary tracks without interaction cancellation (Fig. 2.14a) and with interaction cancellation (Fig. 2.14b).

The main drawback of these solutions is that all the tracks are supplied. Due to the (very)
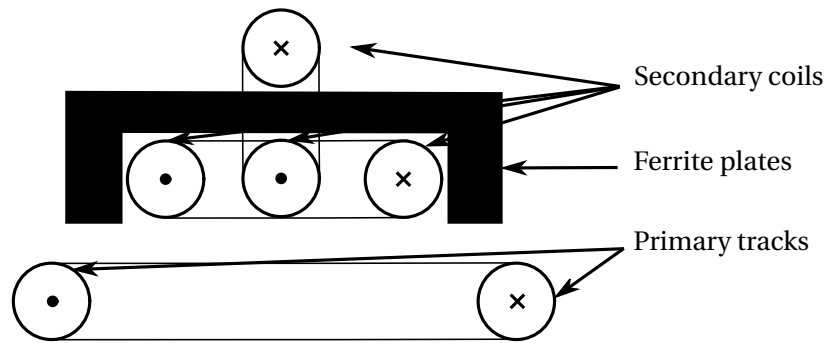
Figure 2.12: A solution proposed for a moving secondary part [35]

Figure 2.13: Prototype realised at the university of Auckland [35]

(a) Non-overlaped primary tracks　　　　(b) Overlaped primary tracks
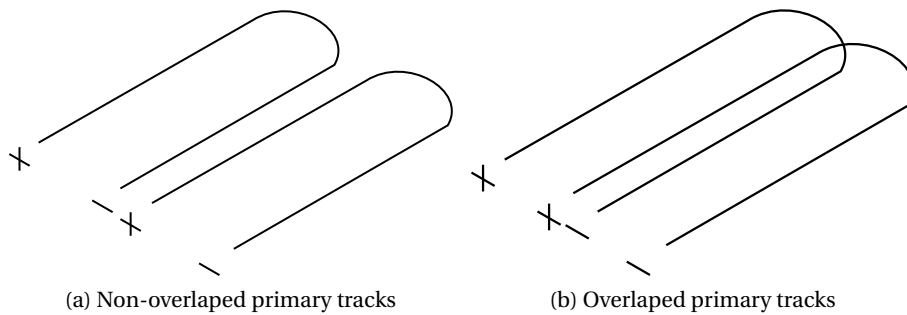
Figure 2.14: Description of the multitracks for pickup applications [34]

large size of the tracks, the efficiency is reduced. Moreover, the magnetic field emission is high where the pickup is not present. The roadway can be subdivided into smaller coils to solve this problem. Only the one where the vehicle is present is supplied. This has been realised in the "Laboratoire d'electromecanique et de machines electriques" at "Ecole Polytechnique Fédérale de Lausanne" to supply an electric transportation vehicle called "Serpentine". This implementation is illustrated in Fig. 2.15 and Fig. 2.16. Only the hashed coils are supplied,

reducing the power losses due to the length of the wires and the magnetic field emission. However, no shielding is present in the vehicle. It means that the magnetic field is quite important there. Moreover, this system does not work if conductive parts are present in the vehicle.
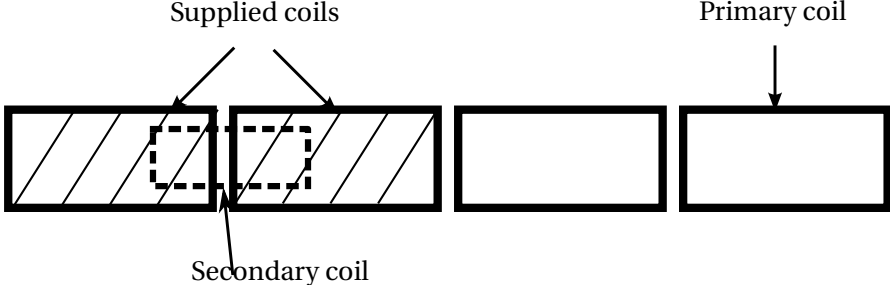
Figure 2.15: The solution implemented for the "Serpentine" project

In last years, the Korean Advances Institude of Science and Technology (KAIST), based in Korea, has been working on a contactless power supply for an electric bus [50, 57, 60, 61]. This system is called OLEV (On-Line Electric Vehicle). The distance between the primary and the secondary parts is 25 cm. Due to the high power transmitted (100 kW), the operating frequency is low (20 kHz). This system is illustrated in Fig. 2.17. It is now working for the transportation in the campus of KAIST.

(a) Photo of the Serpentine installation   (b) Zoom on the vehicle
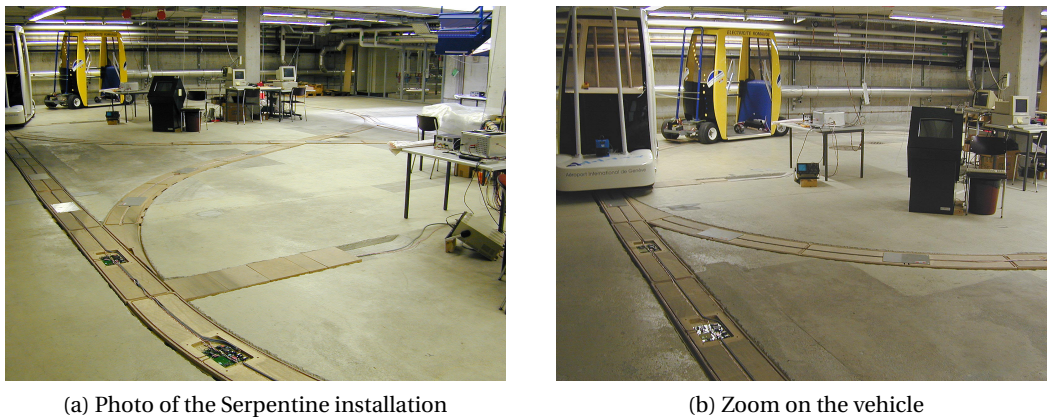
Figure 2.16: Serpentine system
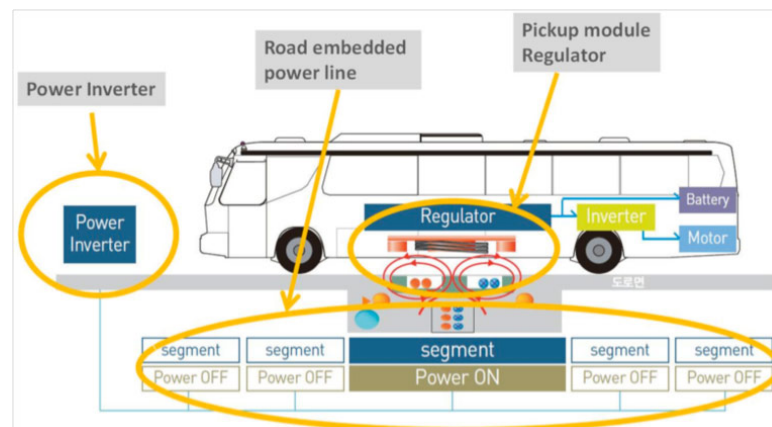
Figure 2.17: Overview of the KAIST OLEV system [48]

2.3.3 Bidirectional power transfer

In most applications, the power transfer is unidirectional. The primary part of the system is energized by the power supply, and the load is located at the secondary part. For contactless electric vehicles charging purpose, it means that the power is transferred from the grid to the vehicle. However, the transfer from the vehicle to the grid using the energy of the battery is more and more interesting. For instance, the energy stored in the battery can be useful for a portable electrical supply.

To ensure the possibility of proper bidirectional power transfer, the configuration of the transformer is very important [73]. If the behaviour of the system is not symmetric, additional power electronics must be inserted to overcome to this asymmetry. A solution is proposed in [46].

2.4 Conclusion

Contactless power transfer using inductive coupler is widely used for many kinds of applications. It can be split into two main categories : low-power applications and high power applications. The challenges are different depending on the power range. A standardization has been established in order to ensure interoperability between the transmitter and the receiver from different companies.

Contactless transfer for electric vehicle supply is a more and more investigated field. Two main types of transmission exist. The first one addresses static power transfer. The car is recharged when it is placed in a charging station. The second one is called dynamic charging. The power is transmitted when the vehicle is moving. The efficiency of the conversion chain is very important since the power in presence is high and the losses have to be dissipated. Emissions of the magnetic field is another important point for such applications to ensure the safety of the user. These challenges will be studied in details in this work.

3 Modelling of the transformer

Contents

3.1 Introduction

The aim of this chapter is to introduce and model the different components of the transformer and its associated electronics. First of all, the whole conversion chain is introduced as well as the main topologies of each element. A first-harmonic approximation is used to model the non-linear elements . The second part of this chapter is dedicated to the study of the magnetic properties of the transformer.

As a first step, the transformer is modelled assuming that it is placed in an air-environment. The different elements of the transformer are modelled and different electric equivalent models are presented and compared. A proper modelling of the transformer is mandatory to determine the behaviour of the system and to be able to design such a system.

In practice, the transformer itself and/or its environment contains conductive and magnetic parts. In this way, the aim of the third section is to adapt the models developed in the first one in order to keep them available in presence of these materials. In all these sections, only the linear effects are taken into account. For instance, the saturation phenomena, which turns the system into a non-linear one is not studied.

3.2 Modelling of the conversion chain

This section addresses the power electronics used to drive the transformer. The conversion process can be split into several parts. First of all, the power supply is assumed to be a continuous voltage. Otherwise, a power rectifier transforms it into a DC one. A power inverter is then used to drive the primary part of the transformer. It injects an alternative current at the desired operating frequency. For low-coupled transformer, a resonant tank is generally inserted to increase the performances of the system. This is studied in details in Chapter 4. A power rectifier is used at the secondary side to get a DC output voltage from the induced voltage into the secondary coil. The load is then connected at the output of the rectifier. An additional power converter is sometimes used if the load voltage must be changed. An overview of the conversion chain is presented in Fig. 3.1.

In this chapter, the currents and voltages of these different elements are computed. However, the modelling of the parasitic effects regarding the practical implementation of the electronics is beyond the scope of this study.

3.2.1 Power inverter

A lot of topologies of inverter exists. The more suitable one depends on the nature of the load, the application and the power range. Since this study is restricted to the drive of the coil for contactless power transfer, the load is assumed to be a resonant RLC tank. Only the resonant inverters are studied for this reason. The inverters can be divided into two main categories. The first one is the so called linear amplifier. The efficiency is very limited so this topology
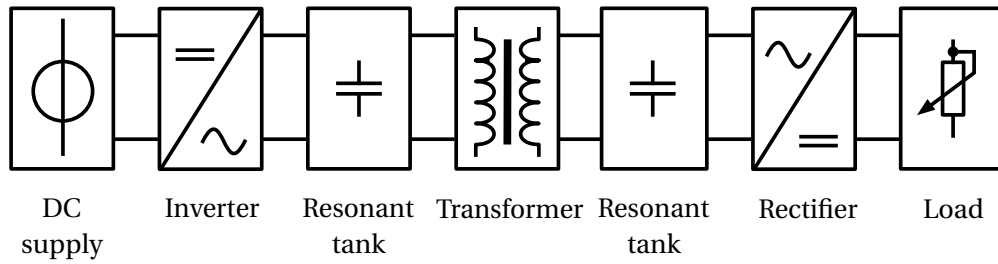
Figure 3.1: Overview of the overall conversion chain

is not often used for contactless power transfer purpose. The second one is the switching amplifier which is widely used for these applications due to its high efficiency and simplicity. Therefore, only this category is studied in this work.

The resonant tank can be a serial RLC or a parallel one. Since a current discontinuity in an inductor leads to an infinite voltage, a serial RLC tank is necessarily driven by a voltage inverter. A parallel RLC tank is necessarily driven by a current inverter since a voltage discontinuity is not allowed across a capacitor.

3.2.2 Overview of the main inverter topologies

The well known half bridge topology, composed of two switches is illustrated in Fig. 3.2. The voltage across the RLC load equals U_{DC} when the switch T_1 is ON and equals 0 when the switch T_2 is ON. One can see that this topology can only drive serial tanks. The capacitor C_1 represents the primary compensation capacitance of the transformer. The capacitance C_f ensures a DC voltage across the bridge while the inductance L_f ensures a DC current in the power supply.
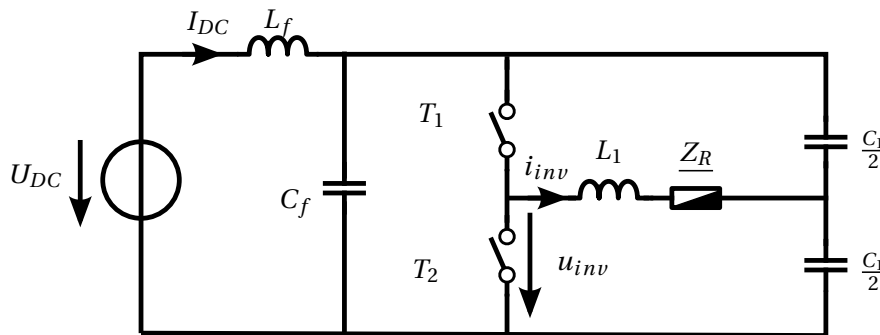
Figure 3.2: Simplified schematic of the half bridge resonant inverter

The command of the half bridge inverter can be decomposed into two phases :

1. During the first phase ($0 < t < \frac{T}{2}$), the switch T_1 is open (conduction mode) while T_2 is closed (blocking mode). During this phase, $u_{inv} \approx U_{DC}$.

2. During the second phase ($\frac{T}{2} < t < T$), the switch T_1 is closed while T_2 is open. During
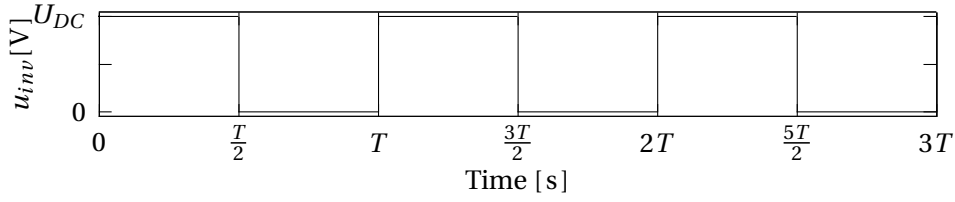
(a) Inverter voltage
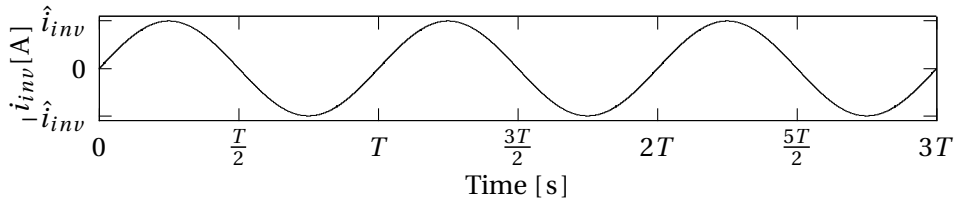
(b) Inverter current

Figure 3.3: Outputs of the half-bridge inverter

this phase, $u_{inv} \approx 0$).

The advantage of this topology is its simplicity because it requires only two switches and thus, two drives. However, the amplitude voltage is limited. For these reasons, it is widely used for induction heating systems [65] .

The most used inverter topology has four switches and is called full bridge. This topology is slightly different depending on the nature of the resonant load. It is presented in the next section.

3.2.3 Study of the full bridge resonant voltage inverter

A simplified schematic of the voltage inverter is presented in Fig. 3.4. The control of the four switches T_1 to T_4 generates a square-wave voltage u_{inv} from the DC voltage U_{DC}. The transformer is shown under its simplified form (this model is detailed in 3.4). The capacitance C_f ensures a DC voltage across the bridge while the inductance L_f ensures a DC current in the power supply.

Full-wave command

This command can be decomposed into two different phases :
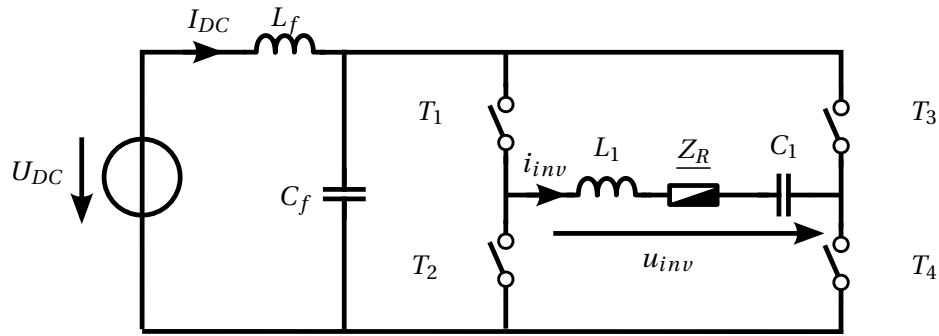
Figure 3.4: Simplified schematic of the voltage resonant inverter

1. During the first phase ($0 < t < \frac{T}{2}$), the transistors T_1 and T_4 are open while T_2 and T_3 are closed ($u_{inv} \approx U_{DC}$).

2. During the second phase ($\frac{T}{2} < t < T$), the transistors T_1 and T_4 are closed while T_2 and T_3 are open ($u_{inv} \approx -U_{DC}$).

The voltage u_{inv} is shown in Fig. 3.5a. Since the current is filtered due to the resonance phenomena (this is computed afterwards), it can be considered to be a sinewave. The current i_{inv}, assuming that the inverter operates at the resonant frequency of the load, is shown in Fig. 3.5b.
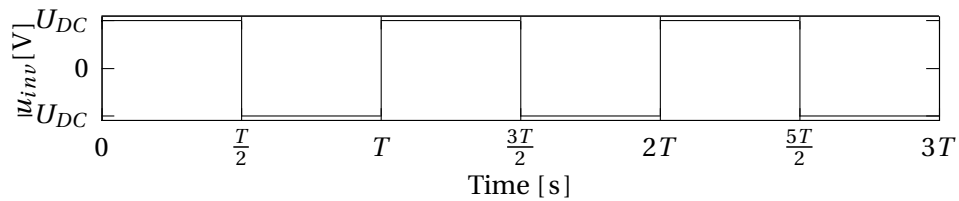
(a) Inverter output voltage
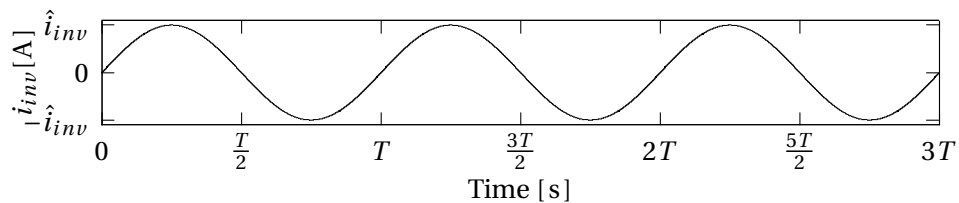
(b) Inverter output current

Figure 3.5: Outputs of the full-bridge inverter

In order to compute the different output parameters of the inverter, the Fourier's decomposition of the ideal inverter voltage outputs is computed in (3.1) and (3.2). The voltage u_{inv} represents the voltage across the resonant tank and the current i_{inv} its associated current.

$$u_{inv}(t) = \sum_{n=0}^{\infty} \frac{4U_{DC}}{(2n+1)\pi} \sin((2n+1)\omega t) \tag{3.1}$$

$$i_{inv}(t) = \sum_{n=0}^{\infty} \frac{4U_{DC}}{(2n+1)\pi || \underline{Z_R}((2n+1)\omega) + j((2n+1)\omega L_1 - \frac{1}{(2n+1)\omega C_1})||} \sin((2n+1)\omega t) \tag{3.2}$$

When the system operates at the resonant frequency (the nominal operating point), (3.2) can be simplified, as suggested in (3.3). This simplification is detailed in the next chapter.

$$i_{inv}(t) = \frac{4U_{DC}\underline{Z_2}}{\pi\omega^2 \underline{M^2}} \sin(\omega t) + \sum_{n=1}^{\infty} \frac{4U_{DC}}{(2n+1)\pi || \underline{Z_R}((2n+1)\omega) + j((2n+1)\omega L_1 - \frac{1}{(2n+1)\omega C_1})||} \sin((2n+1)\omega t)$$
$$\tag{3.3}$$

As suggested in (3.3), a first-harmonic approximation is suitable due to the frequency dependency of the current i_{inv}. The input voltage U_{in} can be deduced from (3.1) as suggested in (3.4). The voltage U_{in} represents the RMS value of first harmonic of the voltage across the tank.

$$U_{in} = \frac{2\sqrt{2}}{\pi} U_{DC} \tag{3.4}$$

The voltage across the resonant tank is proportional to the DC input voltage but can not be modified by this command. Another command called "phase shift modulation" (PSM) consists in introducing a variable phase shift between the two legs. It is the object of the next section.

Phase shift modulation command

The phase shift modulation command can be decomposed into four different steps :

1. During the first phase ($0 < t < T_{shift}$), the transistors T_1 and T_3 are opened while T_2 and T_4 are closed ($u_{inv} \approx 0$).

2. During the second phase ($T_{shift} < t < \frac{T}{2}$), the transistors T_1 and T_4 are opened while T_2 and T_3 are closed ($u_{inv} \approx U_{DC}$).

3. During the third phase ($\frac{T}{2} < t < \frac{T}{2} + T_{shift}$), the transistors T_1 and T_3 are opened while T_2 and T_4 are closed ($u_{inv} \approx 0$).

4. During the fourth phase ($\frac{T}{2} + T_{shift} < t < T$), the transistors T_1 and T_4 are opened while T_2 and T_3 are closed ($u_{inv} \approx -U_{DC}$).
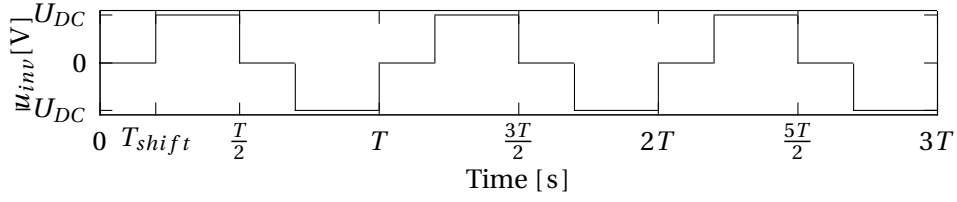
(a) Inverter voltage
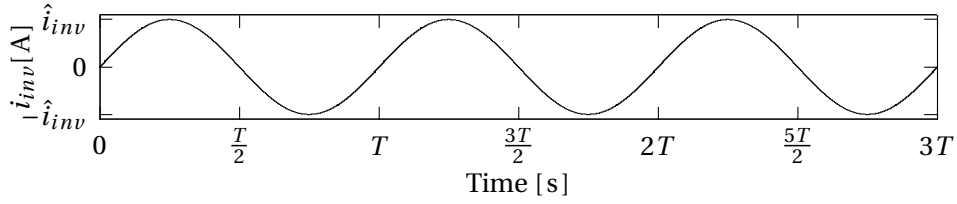
(b) Inverter current

Figure 3.6: Outputs of the inverter using Phase shift modulation

The power injected in the inverter load depends on the delay time T_{shift}. When $T_{shift} = 0$, the maximum power is injected in the transformer. When $T_{shift} = \frac{T}{2}$, no power is injected.

According to [76], the voltage across the inverter load, function of the DC input voltage and the shift angle α is expressed in (3.5).

$$U_{in} = \frac{2\sqrt{2}}{\pi} U_{DC} \sin(\frac{\alpha}{2}) \tag{3.5}$$

The relationship between the shift angle α and the shift time T_{shift} is given in (3.6).

$$\alpha = \frac{T - 2T_{shift}}{T} \cdot \pi \tag{3.6}$$

27

One can see that the case of $\alpha = \pi$ corresponds to a full-wave command, and thus, (3.5) leads to (3.4).

3.2.4   Study of the resonant current inverter

A simplified schematic of the current inverter is presented in Fig. 3.7. The four transistors T_1 to T_4 generate a square-wave current i_{inv} from the DC voltage U_{DC}. The choke inductance L_C ensures a DC current at the input of the bridge.
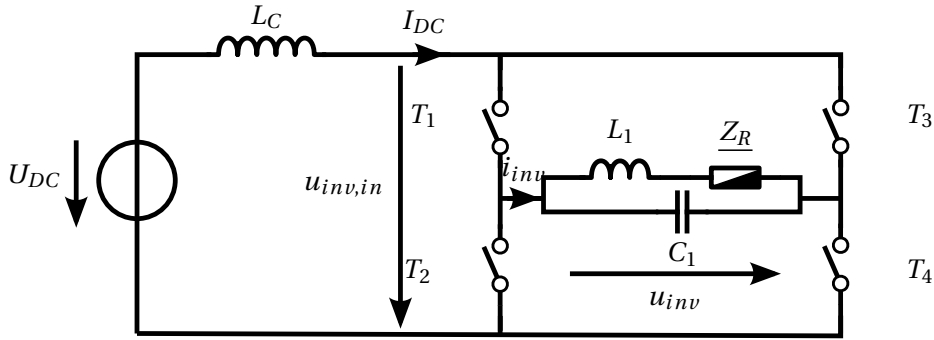
Figure 3.7: Simplified schematic of the current resonant inverter

This command is similar to the voltage inverter using a full-wave command, and can be decomposed into two phases :

1. During the first phase ($0 < t < \frac{T}{2}$), the transistors T_1 and T_4 are opened while T_2 and T_3 are closed ($i_{inv} \approx I_{DC}$).

2. During the second phase ($\frac{T}{2} < t < T$), the transistors T_1 and T_4 are closed while T_2 and T_3 are opened ($i_{inv} \approx -I_{DC}$).

According to [71], the voltage across the inverter load is proportional to the DC input voltage, as shown in (3.7).

$$U_{in} = \frac{\pi}{2\sqrt{2}} U_{DC} \tag{3.7}$$

Unlike the voltage inverter, the phase shift command is not applicable for this topology. An additional power converter is often used to obtain the desired input voltage U_{in}.

3.2.5   Rectifier

The rectifier is used to transform the AC voltage or current from the secondary coil to a DC one to drive the load. Two main categories exist : the active rectifier and the passive one. An
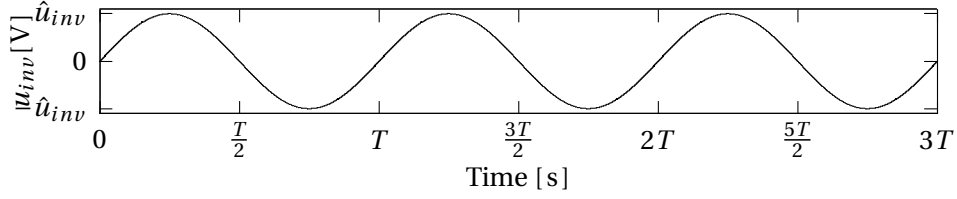
(a) Inverter voltage
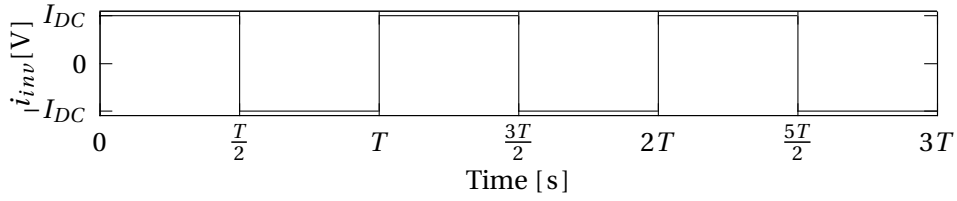
(b) Inverter current

Figure 3.8: Outputs of the inverter

active rectifier is made of switches like the inverter and enables the possibility to control the output voltage or current into the load. A passive rectifier is made of diodes and the output voltage or current depends on the input one and can not be controlled.

Due to the presence of non-linear elements (the diodes), the rectifier acts as a non-linear system. The effective resistance R_{DC} and the rectifier can be modelled into a single resistance Rl using a first-harmonic analysis. This expression of this equivalent resistance is very useful for the modelling of the transformer. A simplified schematic of the passive rectifier used is presented in Fig. 3.9. If the rectifier is driven by a voltage source, an inductance L_f is added.

The expression of the load voltage U_L, current I_L and the equivalent load R_L using the first harmonic analysis can easily be deduced from (3.1) and (3.2).

For a voltage drive :

$$U_L = \frac{\pi}{2\sqrt{2}} U_{DC} \quad (3.8) \qquad I_L = \frac{2\sqrt{2}}{\pi} U_{DC} \quad (3.9) \qquad R_L = \frac{U_L}{\underline{I_L}} = \frac{\pi^2}{8} R_{DC} \quad (3.10)$$

For a current drive :

$$U_L = \frac{2\sqrt{2}}{\pi} U_{DC} \quad (3.11) \qquad I_L = \frac{\pi}{2\sqrt{2}} U_{DC} \quad (3.12) \qquad R_L = \frac{U_L}{\underline{I_L}} = \frac{8}{\pi^2} R_{DC} \quad (3.13)$$

29

(a) Rectifier driven by a voltage source

(b) Rectifier driven by a current source
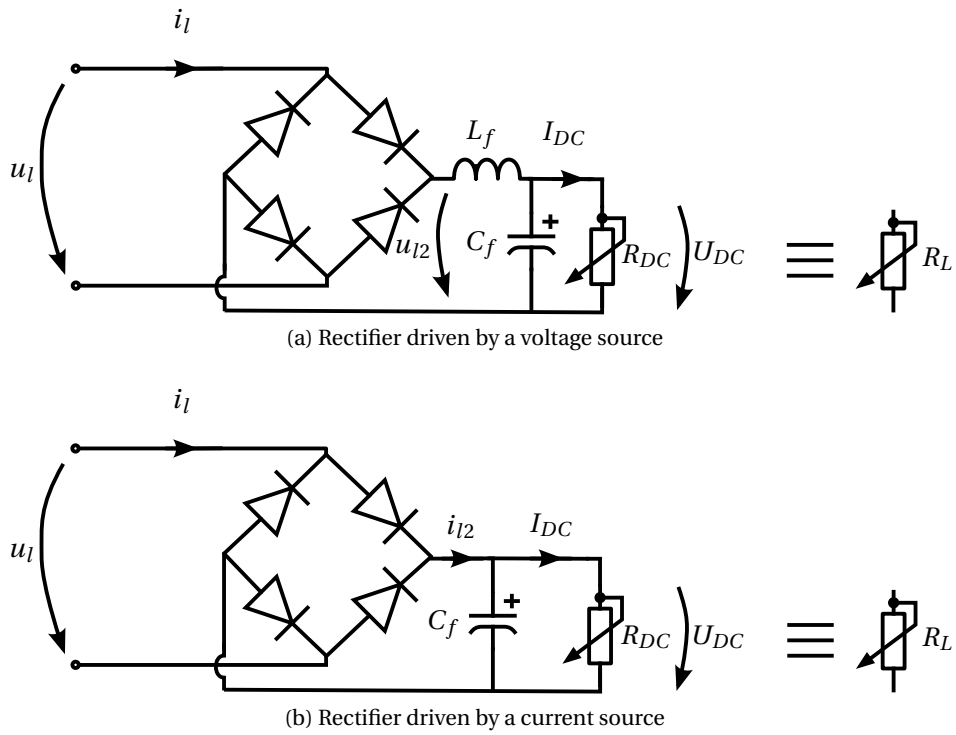
Figure 3.9: Simplified schematic of the rectifier
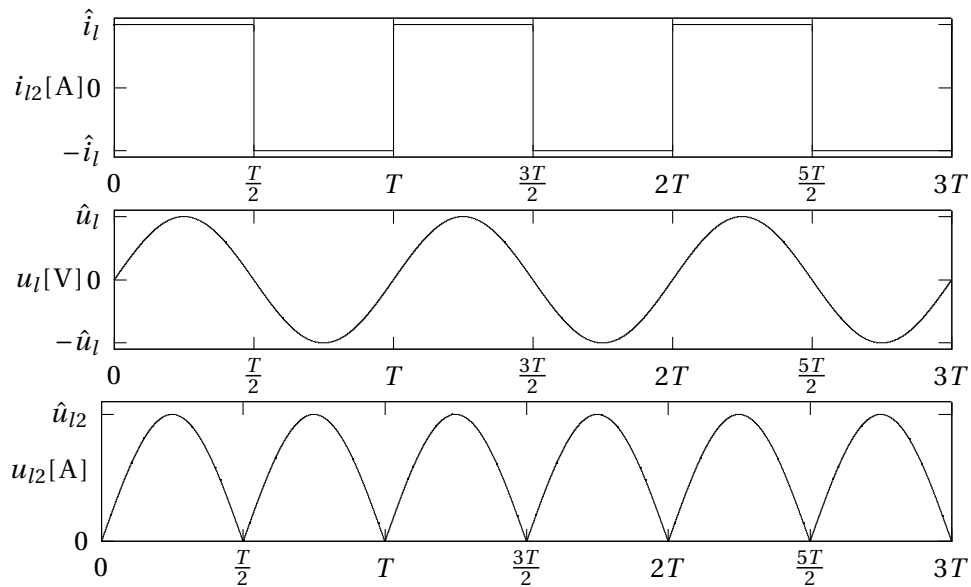
Figure 3.10: Temporal signals for the voltage driven rectifier
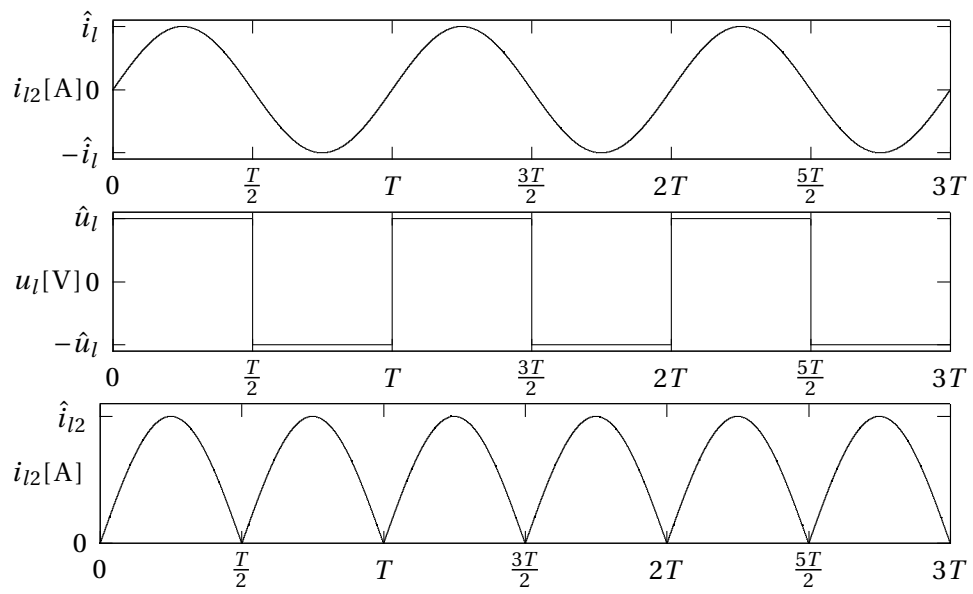
Figure 3.11: Temporal signals for the current driven rectifier

3.2.6 Conclusion

The associated power electronics of the transformer has been introduced and modelled. For all the upcoming developments, the transformer is assumed to be driven by a sine-wave current or voltage. The rectifier is also replaced by its equivalent resistance.

The main inverter topologies introduced in this chapter are compared in Table 3.1.

Topology	Pro	Cons
Linear amp		Efficiency
Half bridge	Number of switches	Serial tank only Power not adjustable
Full bridge, serial tank	Power adjustable Voltage across the switches	Command more complex Current in the switches
Full bridge, parallel tank	Current in the switches	Power not adjustable Voltage across the switches

Table 3.1: Comparison of the main inverter topologies

3.3 Definition of the main magnetic quantities

The fundamental equations of the magnetic properties are defined in this section. It is then used as a starting point for all the following developments.

3.3.1 Maxwell equations

The well-known Maxwell equations define the relationships between the electromagnetic quantities. In this study, the operating frequency is supposed to be small enough to be in quasi-static mode. This means that $\frac{\partial \vec{D}}{\partial t} \ll \vec{J}$. Eq. (3.14) is rewritten in (3.15) under this hypothesis.

$$
\begin{cases}
\vec{\nabla} \times \vec{H} = \vec{J} + \dfrac{\partial \vec{D}}{\partial t} \\[2mm]
\vec{\nabla} \times \vec{E} = -\dfrac{\partial \vec{B}}{\partial t} \\[2mm]
\vec{\triangle} \cdot \vec{B} = 0 \\[2mm]
\vec{\triangle} \cdot D = \rho_q
\end{cases}
\tag{3.14}
\qquad
\begin{cases}
\vec{\nabla} \times \vec{H} = \vec{J} \\[2mm]
\vec{\nabla} \times \vec{E} = -\dfrac{\partial \vec{B}}{\partial t} \\[2mm]
\vec{\triangle} \cdot \vec{B} = 0
\end{cases}
\tag{3.15}
$$

3.3.2 Material properties

The equations describing the material properties are generally combined with the Maxwell equations defined in (3.14). Assuming that the materials properties are isotropic, the relation between the electric field $\vec{E}$, the current density $\vec{J}$ and the resistivity of the material ρ is given in (3.16).

$$
\vec{E} = \rho \vec{J}
\tag{3.16}
$$

The relationship between the magnetic flux density $\vec{B}$ and the magnetic field $\vec{H}$ for an amagnetic material is given in (3.17).

$$
\vec{B} = \mu_0 \vec{H} \ \text{ with } \ \mu_0 = 4 \cdot \pi \cdot 10^{-7} \ \text{T} \cdot \text{m} \cdot \text{A}^{-1}
\tag{3.17}
$$

The relationship between the magnetic flux density and the magnetic field for a ferromagnetic material is shown in Fig. 3.12. This characteristic presents an hysteresis behaviour, source

of hysteresis losses, studied in Section 3.5.2. Except this effect, the B-H characteristics of a ferromagnetic is modelled without its hysteresis effect and restricted to $B > 0$ and $H > 0$, as illustrated in Fig. 3.13.
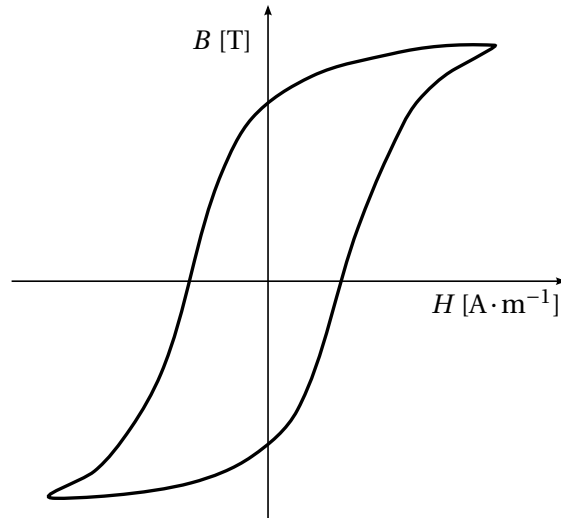
Figure 3.12: Typical B-H characteristics of ferromagnetic materials
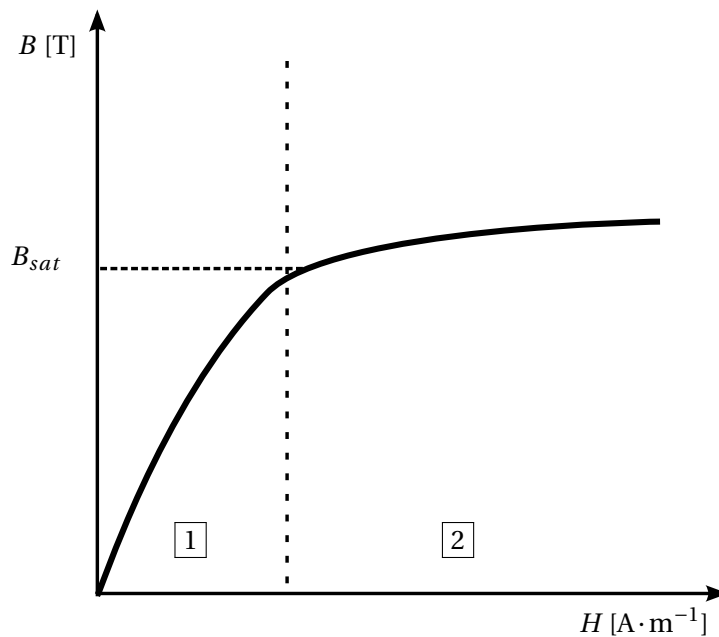
Figure 3.13: Simplified B-H curve generally used

The B-H characteristics presented in Fig. 3.13 can be decomposed into two linear modes :

- The mode $\boxed{1}$ corresponds to the linear mode of the material.

- The mode $\boxed{2}$ corresponds to the saturated mode of the material.

$$B = \begin{cases} \mu_r \mu_0 H & \text{if } B < B_{sat} \\ B_{sat} + \mu_0 H & \text{otherwise} \end{cases} \tag{3.18}$$

3.3.3 Definition of the magnetic flux

The magnetic flux Φ through a surface is defined as the integral over a surface $\mathscr{S}$ of the normal component of the flux density B relative to the surface $\mathscr{S}$, as defined in (3.19). The normalized vector $\vec{n}$ is normal to the surface $\mathscr{S}$. When the conductor is composed of N identical turns, the total flux Ψ is defined as the flux of one turn multiplied by the number of turns, as suggested in (3.20). This is only true if the flux Φ is the same in all turns. Otherwise, the flux seen by each turn must be computed separately.

$$\Phi = \oiint_{\mathscr{S}} \vec{B} \cdot \vec{n} \tag{3.19}$$

$$\Psi = N\Phi \tag{3.20}$$

The magnetic flux is a very important quantity to determine the properties of the coils since the values of the inductances depend on it. This is detailed in the modelling of the inductances.

3.3.4 Solving by using the finite elements methodology

The finite element methodology is a numerical way to solve a physical problem when no analytical approach is suitable or possible. Except for simple particular cases, the differential equations (3.15) can not be solved using an analytical way. It consists in separating the domain into small ones in order to solve the system into each one. The mathematical formalism of this methodology are beyond the scope of this work. However, a lot of relevant references are available, such as [18, 31]. A lot of ready to use software package exist for this purpose. As an example, the simulation of a transformer composed of two coils, two ferrite disks and a conductive plate is detailed. It can be decomposed into several steps.

- The first step consists in describing the geometry of the problem to solve. A proper attention should be paid to the symmetry of the geometry since it allows to reduce the size of the domain. For this example, the geometry is axis-symmetric as suggested in Fig. 3.14. Thus, only a half cross-section is described. The boundary conditions are then described. An infinite box is created and a zero magnetic field is imposed along it.

- The aim of the second step is to define the used materials in presence, model them and assign them to the different regions of the geometry.

- The third step consists in meshing the domain. The mesh elements are generally small triangles for the two dimension simulations and small tetrahedron for three dimensional

simulations, but it can also be rectangle pieces in some particular cases. Each physical quantity in a mesh element is interpolated by a shape function. This latter is generally a second order polynomial shape function for 2D element and a linear interpolation for 3D ones. Therefore, the smaller these elements are, the more precise is the simulation, but longer is the required computation time. Therefore, the choice of the size of these elements is function of the physical effects in presence.

- The fourth step is the solving of the problem. Different numerical solvers are available to this purpose.

- The last step is the post-processing. It consists in analysing the results and compute the desired values.

(a) Geometry   (b) Zoom of the geometry
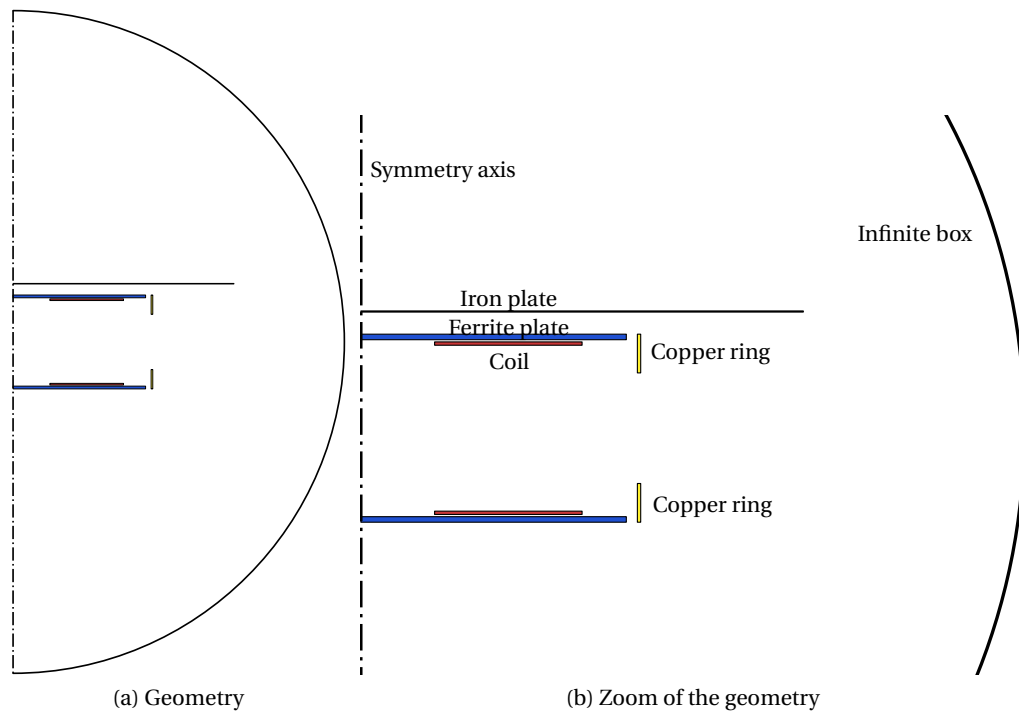
Figure 3.14: Description of geometry to be solved using the finite element method

3.4 Modelling of the air-transformer

In this section, the transformer is modelled, assuming that no conductive or ferromagnetic parts are present. The different elements of the transformer are first introduced. Then, several equivalent models of the transformer found in literature are presented and compared.

3.4.1 Modelling of the coils

Basically, a coil consists in wrapping a wire into one or more turn(s). Its macroscopic electrical equivalent circuit can be modelled as illsutrated in Fig. 3.15. Basically, it can be modelled as an inductance L_s, a serial resistance R_s and a parallel capacitance C_p.
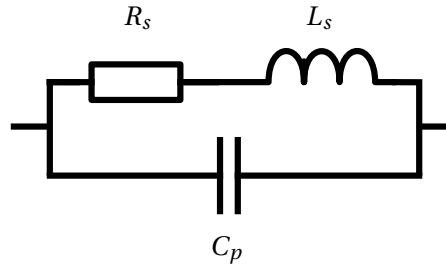
Figure 3.15: Electric equivalent circuit of a coil

When the working frequency is far under the intrinsic resonant frequency , the parallel capacitance C_p can be neglected. This hypothesis can be made for most contactless transfer designs. Thus, this hypothesis ($C_p \to 0$) is assumed in all developments made in this document.

3.4.2 Modelling of the resistances

The serial resistances of the coils are the source of losses in the transformer. When a conductor is supplied with an alternative current, depending on the frequency, the current density is not uniform in the conductor; this is the so-called Eddy current effect. A complete study of this phenomenon is beyond the scope of the document. However, additional information is available in [66]. An approximation of the effective resistance is expressed in (3.22). When many conductors are supplied by an AC current, a proximity effect appears which modifies the distribution of the current density. This effect is beyond the scope of this document since Litz wires are very often used for high power transfer. However, additional information is available in [28].

When a conductor is traversed by an alternative current, an alternative magnetic field which induces an opposite current is generated in the conductor. As a result, the current density is concentrated in the external part of the conductor. This is the well-known skin effect.

The repartition of the current density for a circular conductor of radius R at the position r r is shown in (3.21).

$$J(r) = J_S \, e^{-\frac{R-r}{\delta}} \tag{3.21}$$

The parameter δ is the so-called skin depth. It depends on the electrical resistivity of the conductor material ρ, the operating electrical pulsation ω and the relative permeability of the

material μ.

An approximative formula for the resistance of the coils is proposed in (3.22).

$$R = \begin{cases} \rho \dfrac{l}{\pi r^2} & \text{if } r < \delta \\[2ex] \rho \dfrac{l}{\pi \delta (2r - \delta)} & \text{if } r > \delta \end{cases} \qquad (3.22) \qquad\qquad \delta = \sqrt{\dfrac{2\rho}{\omega \mu}} \qquad (3.23)$$

When the current through the conductor requires a size larger than the parameter δ ($r>\delta$), the resistance increases. In order to avoid this undesirable effect, Litz wires which consists in using several thin insulated wires in parallel are generally used.

3.4.3   Modelling of the inductances

Basically, the self inductance of a coil is the ratio of its magnetic flux over its current, as defined in (3.24). The mutual inductance between two coils is the ratio of the magnetic flux seen by the first coil divided by the current of the second one, as defined in (3.25). For the computation of the inductances, only one coil must be supplied.

$$L_i = \frac{\Psi_i}{I_i} \Big|_{I_j = 0 \, \forall j \in [0,k], j \neq i} \tag{3.24}$$

$$M_{ij} = \frac{\Psi_i}{I_j} \Big|_{I_j = 0 \, \forall j \in [0,k], j \neq i} \tag{3.25}$$

When the environment is only made of air, Neumann formulas, derived from the well-known Biot-Savart's law can be used to compute self and mutual inductances. Only the main results of the application of these formulas are presented. More details can be found in [49, 5].

Considering two coils shape $\mathscr{C}_i$ and $\mathscr{C}_j$ as illustrated in Fig. 3.16, the mutual inductance is defined in (3.27).

In practice, the evaluation of the self inductance can be made using the same formula as the ones for the mutual inductance, but a singularity appears when $|\vec{d}_{ij}| = 0$. In order to avoid this problem, the self inductance is generally split into two parts : the external self inductance and the internal one. As a result, the self inductance is expressed as the sum of these two contributions, as shown in (3.26). The internal self inductance decreases with the frequency and its value is negligible compared to the external inductance [49]. As a result, only the
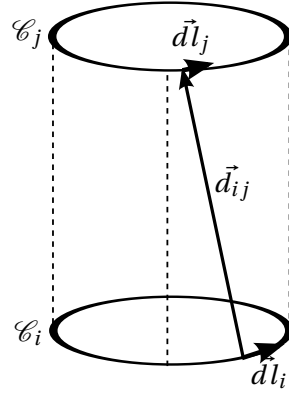
Figure 3.16: Geometric situation for the computation of the mutual inductance of two turns

external contribution is taken into account in this study.

$$L = L_e + L_i \tag{3.26}$$

$$
\begin{cases}
L_e = \dfrac{\mu_0}{4\pi} \oint_{C_i} \oint_{C_j} \dfrac{\vec{dl_i} \cdot \vec{dl_j}}{|\vec{d_{ij}}|} \\[3mm]
M_e = \dfrac{\mu_0}{4\pi} \oint_{C_i} \oint_{C_j} \dfrac{\vec{dl_i} \cdot \vec{dl_j}}{|\vec{d_{ij}}|}
\end{cases}
\tag{3.27}
$$

Applying (3.27) to circular coils leads to (3.28).

$$
\begin{cases}
L_e = \mu_0 \mu_{air} \sqrt{r \cdot r_i} \cdot a \cdot \displaystyle\int_0^{\frac{\pi}{2}} \dfrac{2\sin^2\vartheta - 1}{\sqrt{1 - a^2 \cdot \sin^2\vartheta}} \, \mathrm{d}\vartheta \text{ with } a^2 = \dfrac{4 \cdot r \cdot r_i}{(r + r_i)^2} \\[4mm]
M_e = \mu_0 \mu_{air} \sqrt{r_1 \cdot r_2} \cdot b \cdot \displaystyle\int_0^{\frac{\pi}{2}} \dfrac{2\sin^2\vartheta - 1}{\sqrt{1 - b^2 \cdot \sin^2\vartheta}} \, \mathrm{d}\vartheta \text{ with } b^2 = \dfrac{4 \cdot r_1 \cdot r_2}{(r_1 + r_2)^2 + h^2}
\end{cases}
\tag{3.28}
$$

where L_e represents the inductance of one turn, M_e the mutual inductance between two turns of radius r_1 and r_2, and r and r_i the geometrical parameters of the coil.

For N turns, the inductances are defined in (3.29) ($M_{1i,2j}$ is the mutual inductance between

the i-th turn of the primary coil and the j-th turn of the secondary coil).

$$
\begin{cases}
L = \sum_{i=1}^{N} \sum_{j=1}^{N} M_{Ti,Tj} \\[2ex]
M = \sum_{i=1}^{N_1} \sum_{j=1}^{N_2} M_{1i,2j}
\end{cases}
\tag{3.29}
$$

One can see that if the coupling between the turns equals 1 (all the magnetic flux created by one turn is caught by the others), $L = N^2 L_e$. Under this hypothesis about the mutual inductance, $M = N_1 N_2 M_e$. This approximation is very useful in practice to have an approximation of the number of turns needed to realise a design.

3.4.4 Electric equivalent circuit

In this section, several electric equivalent circuit of the transformer are presented, and then compared.

The first one is the representation the most used in this work and is presented in Fig. 3.17. The resistances R_1 and R_2 are the serial resistances of the coils, L_1 and L_2 the self inductances of the coils and M the mutual inductances between the primary and secondary coils.
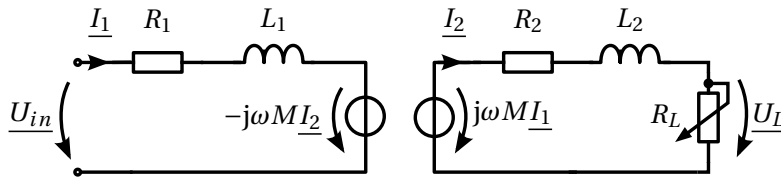
Figure 3.17: Electric equivalent circuit of an uncompensated transformer

The currents $\underline{I_1}$, $\underline{I_2}$ and the load voltage $\underline{U_L}$ can be determined solving (3.30).

$$
\begin{cases}
\underline{U_{in}} = (R_1 + j\omega L_1)\underline{I_1} - j\omega M \underline{I_2} \\[1.5ex]
j\omega M \underline{I_1} = (R_2 + R_L + j\omega L_2)\underline{I_2} \\[1.5ex]
\underline{U_L} = R_L \underline{I_2}
\end{cases}
\tag{3.30}
$$

The second representation is detailed and extracted from [47]. It is detailed in (3.31), (3.32) and Fig. 3.18. Unlike the previous representation, this one is made of an ideal transformer and a leakage inductance, function of both the self and mutual inductances. The leakage

inductance can be expressed at both primary side L_{fp} (Fig. 3.18a) and secondary side L_{fs} (Fig. 3.18b).

(a) Primary reported

(b) Secondary reported
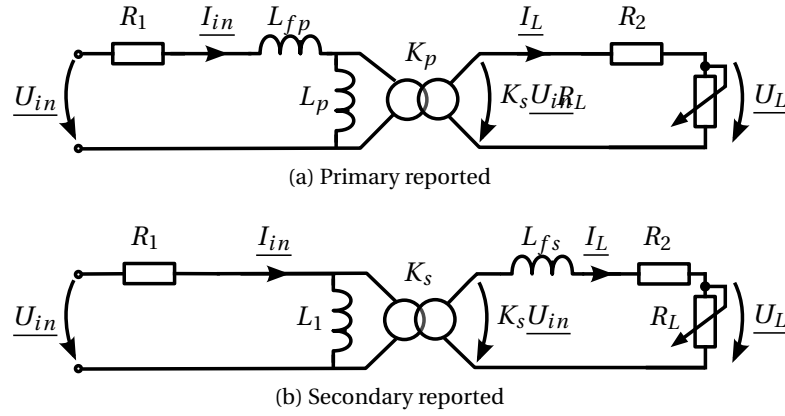
Figure 3.18: Electric equivalent circuit of an uncompensated transformer [47]

$$\begin{cases} K_p & = \dfrac{L_2}{M} \\ L_p & = \dfrac{M^2}{L_2} \\ L_{fp} & = \dfrac{L_1 L_2 - M^2}{L_2} \end{cases} \qquad (3.31) \qquad \begin{cases} K_s & = \dfrac{M}{L_1} \\ L_{fs} & = \dfrac{L_1 L_2 - M^2}{L_1} \end{cases} \qquad (3.32)$$

The third representation is presented in [32]. It is widely used for conventional transformers. In this model, K is the gain of an ideal transformer, R_1 and R_2 the resistances of the coils, $X_{\sigma 1}$ and $X_{\sigma 2}$ the leakage impedances and X_h the mutual reactance.

The main restriction of this modelling is the hypothesis defined in (3.34). The primary and secondary self inductances L_1 and L_2 are squared functions of the number of turns.
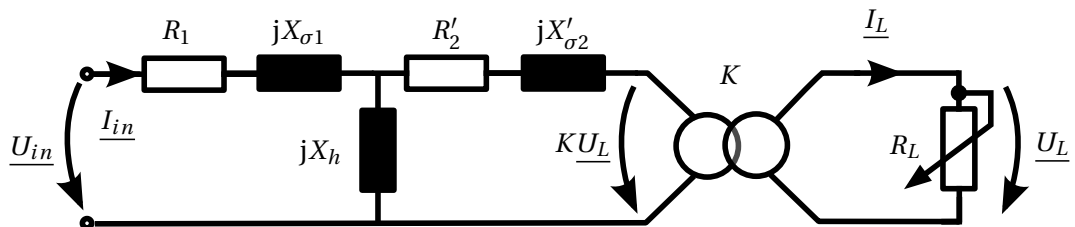
Figure 3.19: Electric equivalent circuit of an uncompensated transformer

$$\begin{cases} K = \dfrac{N_1}{N_2} \\ X'_{\sigma2} = K^2 X_{\sigma2} \\ R'_2 = K^2 R_2 \end{cases} \quad (3.33) \qquad \begin{cases} L_1 = N_1^2 \Lambda_1 \\ L_2 = N_2^2 \Lambda_2 \end{cases} \quad (3.34)$$

This third representation Fig. 3.19 is probably the most used in literature for the study of core-transformers. However, using the parameters identification proposed in [32], its restrictive hypothesis defined in (3.34) is not very convenient for contactless power transfer. Indeed, although it is useful to have an approximation of the required number of turns for a transformer, it is not very practical for the modelling because of the nature of the coreless coils. In conclusion, the first representation Fig. 3.17 is generally used for this study and is equivalent to the second one (Fig. 3.18).

3.5 Modelling of the transformer in presence of conductive and/or ferromagnetic parts

The electric equivalent circuit introduced in the previous section is very useful for the design and the analysis of a transformer. However, in practice, the environment of the transformer often contains conductive or ferromagnetic parts. Moreover, such parts are sometimes added to the transformer itself in order to increase its performances. As a result, the behaviour of the system is generally strongly modified. Eddy currents and a linear approximation of hysteresis losses are studied in order to adapt the electrical equivalent circuit of the transformer presented in Section 3.4.4, taking into account these effects.

3.5.1 Modelling of Eddy currents

An alternative magnetic field induces a current in a conductive part. This is the so-called Eddy current effect, illustrated in Fig. 3.20. The relation between the magnetic flux density in the material and its induced current density is shown in (3.35).

$$\vec{\nabla} \times \vec{J} = \frac{-1}{\rho} \frac{\partial \vec{B}}{\partial t} \tag{3.35}$$

The resulting induced power losses is expressed in (3.36).

$$P_{loss,eddy} = \iiint_V \rho J^2 \mathrm{d}V \tag{3.36}$$
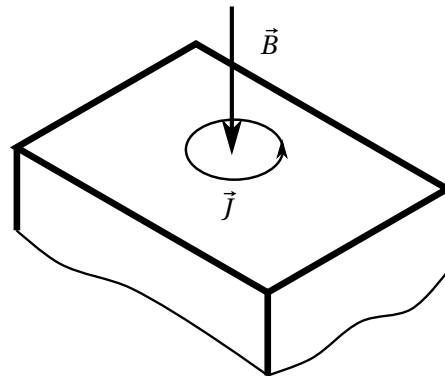
Figure 3.20: Description of Eddy current effect

In practice, it is often very difficult to determine an analytical modelling of the repartition of the current density J in the conductive part. Thus, the finite element method is widely used to determine J. This value is then numerically integrated as suggested in (3.36).

In order to study this phenomenon, the situation shown in Fig. 3.21 is investigated. An alternative current is imposed in the coil. Eddy currents are induced into the iron plate. The electric equivalent circuit of such a system is presented in Fig. 3.22. One can see that this example is solved using the 2D finite element methodology since this configuration is axis-symmetric.
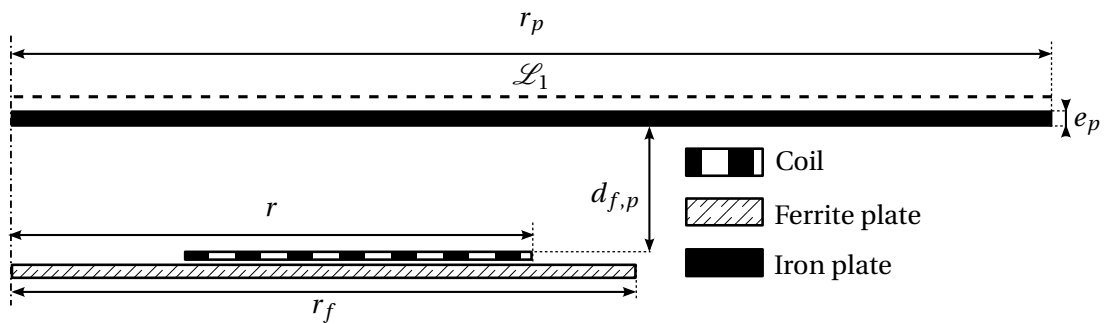
Figure 3.21: cross-section of the scenario studied
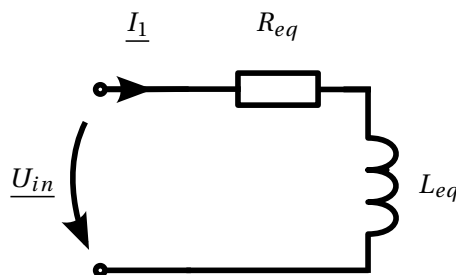
Figure 3.22: Electric equivalent circuit of the scenario studied

The equivalent resistance R_{eq} is composed of two terms : a static resistance of the coil due to the resistance of the wire and a resistance due to the dissipation in the plate induced by the Eddy currents.

The inductance L_{eq} represents the equivalent inductance of the coil in presence of the plate. Due to the phase of the current induced in the latter, the equivalent inductance is smaller than the self-one.

These equivalent parameters can be obtained during the post-processing step using (3.37) and (3.38).

$$R_{eq} = \text{Re}(\frac{\underline{U_{eq}}}{\underline{I_{eq}}}) \qquad (3.37) \qquad\qquad L_{eq} = \text{Im}(\frac{\underline{U_{eq}}}{\omega\underline{I_{eq}}}) \qquad (3.38)$$

In order to highlight the Eddy currents effect, the two following scenarios are investigated :

- Scenario sc_1 : Only the coil and the ferrite are studied (Fig. 3.23a).

- Scenario sc_2 : The iron plate is added to the previous scenario (Fig. 3.23b).

(a) Scenario sc_1
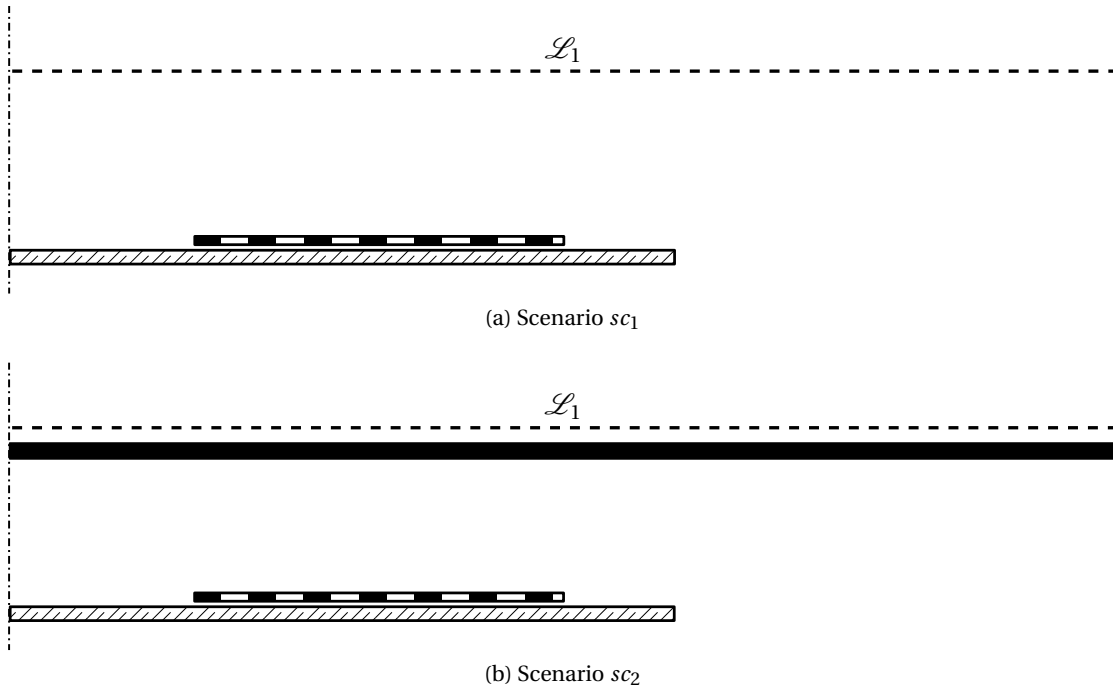
(b) Scenario sc_2

Figure 3.23: The different scenarios studied

The arbitrary electrical parameters used for this study are listed in Table 3.2, the geometrical ones in Table 3.3 and the physical ones in Table 3.4. The repartition of the current density in the coil is supposed to be uniform (Litz wires are used). The equivalent resistance and inductance, function of the working frequency are plotted in Fig. 3.24.

Table 3.2: Electrical parameters

Parameter	Value
Current in the coil	$I_1 = 20\,\text{A}$
Operating frequency	$f = 50\,\text{kHz}$

Table 3.3: Geometrical parameters

Parameter	Value
Radius of the coil	$r = 250\,\text{mm}$
Number of turns	$N = 15$
Radius of the ferrite	$r_f = 350\,\text{mm}$
Distance coil-plate	$d_{f,p} = 30\,\text{mm}$
Radius of the plate	$r_p = 600\,\text{mm}$
Thickness of the plate	$e_p = 0.5\,\text{mm}$

Table 3.4: Material properties

Part	Material	Properties
Coil	Copper	$\rho = 17 \cdot 10^{-9}\,\Omega\text{m}$, $\mu_r = 1$
Ferrite	N7 [†]	$\rho = 3\,\Omega\text{m}$, $\mu_r = 2000$, $B_{sat} = 0.5\,\text{T}$
Plate	Iron	$\rho = 85 \cdot 10^{-8}\,\Omega\text{m}$, $\mu_r = 1000$

[†] see EPCOS website [1]

Based on this study, one can see that the equivalent inductance L_{eq} decreases when the frequency increases. Since the magnetic field induced by the Eddy currents is opposed to the magnetic field generated by the coil (according to Lenz law), the flux of the coil decreases. The equivalent resistance R_{eq} increases when the frequency increases. As shown in Fig. 3.24a, the behaviour of this resistance regarding the frequency can be split into two parts :

- When the skin depth of the material is greater than the thickness of the plate ($\delta > e_p$), the equivalent resistance value is a quadratic function of the frequency. This result is coherent with the conclusions made in [43].

- When the skin depth of the plate is smaller than the thickness of the material ($\delta < e_p$), the equivalent resistance value is a root function of the frequency. This result is coherent with the conclusions made in [43].
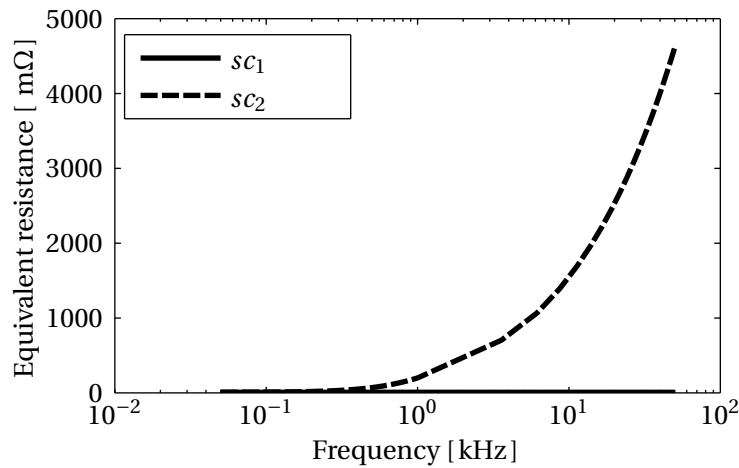
(a) Equivalent resistance function of the operating frequency
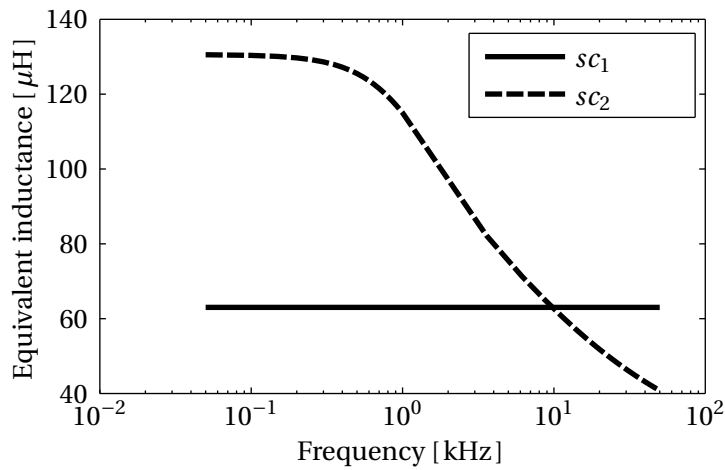
(b) Equivalent inductance function of the operating frequency

Figure 3.24: Resistance and inductance function of the operating frequency
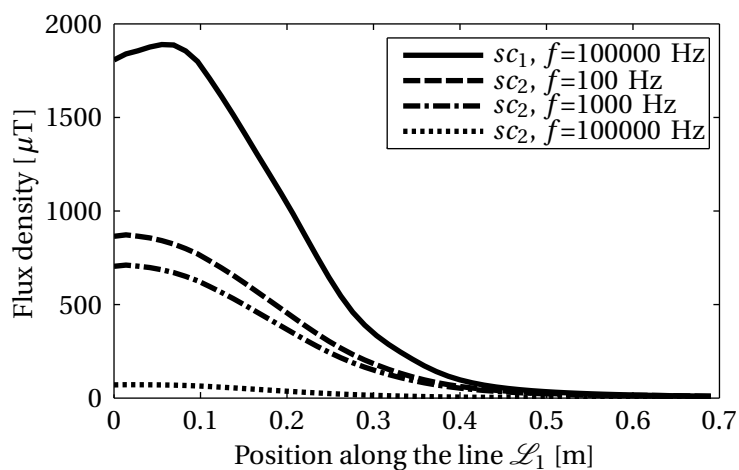
Figure 3.25: Magnetic emission for different frequencies

3.5.2 Modelling of Hysteresis losses

In all the previous sections, the system is assumed to be linear. Although the hysteresis losses is a phenomenon due to the non-linear characteristic of the magnetic field in a ferromagnetic material, the losses induced by this latter can be approximated as an additional resistance in the electrical domain. Several modelling of hysteresis effect are available in [54]. In order to model the hysteresis losses in an environment containing ferromagnetic parts, one suitable methodology is studied.

An empirical model of hysteresis losses, taken from [32] is given in (3.39). In this formula, $\mathrm{d}m$ is a mass element, C_h a coefficient depending on the material specifications, $\hat{B}$ the maximum amplitude of the flux density .

$$P_{loss,hyst} = \int_m C_h f \hat{B} \mathrm{d}m = \int_V C_{h,eq} \mathrm{d}V \tag{3.39}$$

In practice, the coefficient $C_{h,eq}$ is given in the specifications of the material. An example of the description of this coefficient is given in Fig. 3.26 for the ferrite N27, assuming that the temperature of the material is 20 degrees. Using the finite element method, the flux density is integrated as suggested in (3.39) in order to get the losses due to this effect.
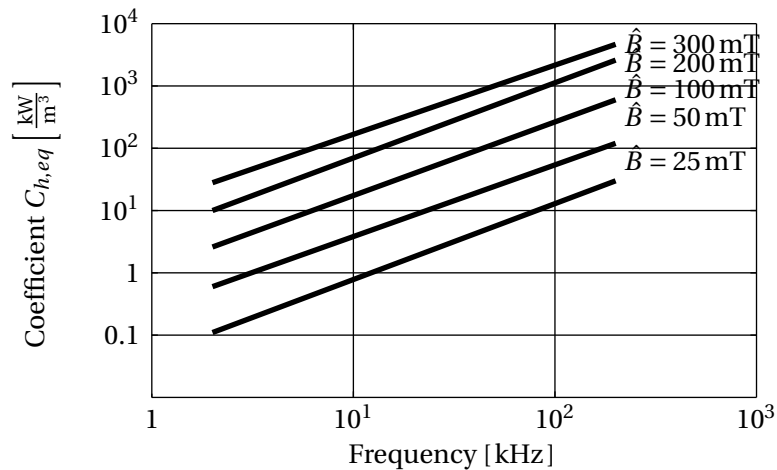
Figure 3.26: Coefficient $C_{h,eq}$ for N7 material [19]

3.5.3 Electric equivalent circuit

The electric equivalent circuits of the transformer introduced in Section 3.4.4 are still valid for a transformer which contains conductive and ferromagnetic parts if the elements of the

circuit are adapted as suggested in (3.40). This adaptation integrates the skin and hysteresis effects. These equations are generally solved using the finite element methodology.

$$
\begin{cases}
R_{i,tot} = R_i + R_{eddy,i} + R_{hyst,i} \, , \, i = 1, 2 \\
L_i \quad = |\dfrac{\Psi_i}{I_i}| \, , \, i = 1, 2 \\
M \quad = |\dfrac{\underline{\Psi}_1}{\underline{I}_2}| = |\dfrac{\Psi_2}{\underline{I}_1}|
\end{cases}
\tag{3.40}
$$

The equivalent resistance of the coils can be split into three parts. The first one is the intrinsic resistance of the wire R_i. It is constant if the skin effect is neglected. Otherwise, it increases when the operating frequency increases. The second one $R_{eddy,i}$ models the power losses induced by the Eddy current effect on the conductive parts present in the environment. The third one $R_{hyst,i}$ is a representation of the power losses in the magnetic components of the environment due to the hysteresis effect. Since a linear representation of these effects is used, the superposition principle can be used and the total equivalent resistance $R_{i,tot}$ is the sum of these three contributions.

The determination of the equivalent self inductance L_i is the total flux Ψ_i divided by the current flowing in the coil I_i. However, unlike in an air environment, the magnetic flux is also dependant on the flux induced by the Eddy currents in the conductive parts of the environment. The reasoning is the same for the mutual inductance.

3.6   Conclusion

This chapter presents a modelling of the different elements of the conversion chain, which can be divided into two main parts. The first one is the power electronics needed to drive the coils of the transformer. Several topologies of the inverter which drives the primary coil and its associated commands have been introduced. The choice of the inverter topology depends on several parameters such as the transformer topology and the desired input voltage. The phase shift modulation command, which allows to control the power injected in the transformer has been presented and modelled. Due to the presence of the switches and the diodes, the inverter and the rectifier are non-linear systems. A first-harmonic approximation has been proposed, which will be used for the next chapters.

The second part of this chapter is dedicated to the modelling of the transformer's magnetic properties. The different constituting elements of the coils have been studied. As a first part, the serial resistance, self and mutual inductances have been computed in an air environment. The skin effect is introduced in the computation of the resistances. The Neumann formulas, derived from the well-known Biot-Savart law are used and solved using a numerical methodology in order to compute the inductance values.

Moreover, the different electric equivalent circuits of the transformer found in literature have been presented and compared. The fourth part of this chapter addresses the modelling of the resistances and inductances of the coil in presence of conductive and/or ferromagnetic parts. The equivalent circuit developed for an air environment are still available if the resistances and inductances are redefined.

Innovative contribution to the chapter

The different parts of the transformer and its associated electronics are studied in this chapter.Two different inverter topologies and the rectifier are modelled. Different electric equivalent circuit of the transformer in an air environment are presented and compared. A modelling of the losses induced by the Eddy currents and hysteresis effect has been developed in order to keep the previous modelling available.

4 Capacitive compensation of the transformer

Contents

4.1 Introduction and motivations

In most contactless power transfer applications, the transformer described in Fig. 3.17 is not used in this form because of its natural poor magnetic coupling between the primary and the secondary coil. In fact, the leakage flux of such a transformer leads to a low power factor (typically between 0.1 and 0.3). Therefore, one or more capacitances are usually combined with the transformer in order to compensate the leakage energy stored in the coils. This chapter highlights the motivations to use these capacitances. The main compensation topologies are then introduced and studied. Two methodologies to determine the capacitance values are presented. The first one, which aims to maximize the transformer efficiency is very known in literature. The second one, which aims to simplify the control of the transformer, is a novel one proposed in this work. The main characteristics of the transformer working at its resonant frequency, such as the power transfer capability, the efficiency and the load characteristics are investigated and compared. Finally, the frequency response of the transformer is addressed. It is very useful to determine the behaviour of the transformer when the operating frequency changes or when the transformer is detuned.

First of all, a proper compensation of the transformer increases its performances. The main motivation is to decrease the current flowing through the coils for a given transferred power. Thus, the aim is to decrease the Joule losses in the coils in order to increase its efficiency. Let us introduce this compensation with a simple example. The numerical application of this latter comes from one of the prototype detailed in Chapter 6.

Two scenarios are investigated and their respective associated equivalent electric circuit (EEC) are illustrated in Fig. 4.1. The electrical circuit of the compensated transformer Fig. 4.1b is solved without lack of generality. In fact, the uncompensated transformer presented in Fig. 4.1a is a particular case of the compensated transformer when $C_1 \rightarrow \infty$ and $C_2 \rightarrow \infty$. The corresponding equation system, which is obtained applying Kirchoff's law at both primary and secondary sides from the equivalent electric circuit (EEC) are computed in (4.1).

In all the development undertaken in this chapter, the ESR (Equivalent Serial Resistance) of the capacitances are neglected. The characteristics of the compensated transformer does not depend on these resistances for low dissipation factor, such as the MKP technology. However, the thermal dissipation of the capacitance losses may become an issue for high power applications.

- Inductances of the transformer : $L_1 = 1.2\,\text{mH}$, $L_2 = 1.1\,\text{mH}$, $M = 115\,\mu\text{H}$

- Load characteristics: $P_L = 300\,\text{W}$, $R_L = 30\,\Omega$

- Operating frequency : $f_0 = 50\,\text{kHz}$

$$
\begin{cases}
j\omega M \underline{I_1} = (R_2 + j\omega L_2 + R_L)\underline{I_2} \\[2em]
\underline{U_{in}} = (R_1 + j\omega L_1)\underline{I_1} - j\omega M \underline{I_2}
\end{cases}
\tag{4.1}
$$

(a) Uncompensated transformer

(b) Compensated transformer using capacitances

(c) EEC of uncompensated transformer

(d) EEC of Compensated transformer
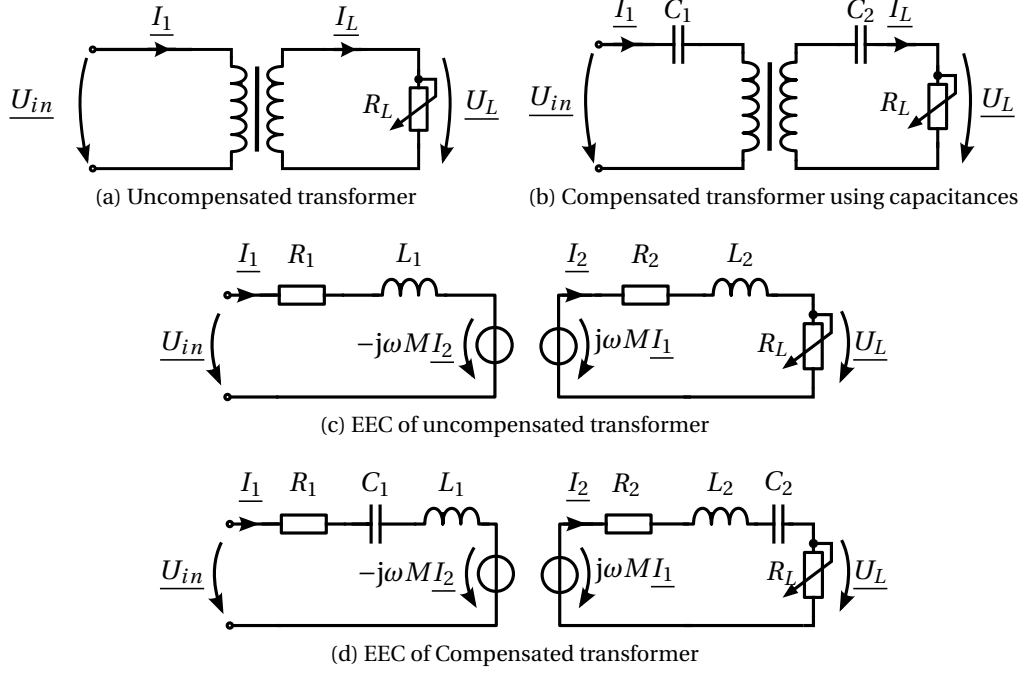
Figure 4.1: Description of the two scenarios studied

$$
\begin{cases}
P_L = R_L I_1^2 \\[2mm]
\cos(\phi) = \arg(\underline{I_{in}}) - \arg(\underline{U_{in}}) \\[2mm]
\eta = \dfrac{P_L}{U_{in} I_{in} \cos(\phi)}
\end{cases}
\tag{4.2}
$$

The transmitted power to the load P_L is obtained solving the three equations described in (4.1) and applying (4.2). The solution is given in (4.3).

$$
P_L =
\begin{cases}
\dfrac{R_L \omega^2 M^2 I_1^2}{(R_L + R_2)^2 + (\omega L_2)^2} & \text{for the uncompensated scenario (Fig. 4.1c)} \\[4mm]
\dfrac{R_L \omega^2 M^2 I_1^2}{(R_L + R_2)^2 + (\omega L_2 - (\omega C_2)^{-1})^2} & \text{for the compensated scenario (Fig. 4.1d)}
\end{cases}
\tag{4.3}
$$

Applying (4.3) leads to the results given in (4.4) for the uncompensated transformer and (4.5) for the compensated one.

$$\begin{cases} U_{in} \approx 10,7\,\text{kV} \\ I_1 \approx 30\,\text{A} \\ \cos(\phi) \approx 0.006 \\ \eta \approx 0.1 \end{cases} \qquad (4.4)$$

$$\begin{cases} U_{in} \approx 120\,\text{V} \\ I_1 \approx 2.7\,\text{A} \\ \cos(\phi) \approx 1 \\ \eta \approx 0.9 \end{cases} \qquad (4.5)$$

One can see in (4.3) that the current I_1 flowing in the primary coil is very large to be able to transfer the required power. This is due to the very low power factor of the uncompensated transformer. As a result, the efficiency is very low and the primary voltage U_{in} very high. Adding compensation capacitances to cancel the reactive power stored in the coils multiplies the efficiency by a factor 9 and divides the required input voltage by 100.

The resonant response of the compensated transformer is also an advantage for the power electronics. Firstly, the harmonics generated by the switching inverter are rejected. Secondly, a sine-wave current in injected in the primary coil from a square-wave voltage thanks to the resonance phenomenon.

4.2   Compensation methodologies

The two compensation capacitances C_1 and C_2 for the main topologies give two degrees of freedom in the system. Two independent conditions can be thus imposed. In literature, the transformer is tuned to maximize the power factor of the transformer and its efficiency. As developed in the next section, the main drawback of this methodology is that, depending on the compensation topology, the capacitance values are function of the parameters of the transformer, such as the load resistance and the mutual inductance. In this way, a novel compensation methodology, called "control-oriented compensation" is proposed. It aims to simplify the control of the transformer by choosing if possible the value of the capacitances independently of these parameters.

For both compensation methodologies, the secondary compensation capacitance is first computed. The primary one is computed as a second step. The order of these steps is not mandatory but is very practical since the value of the secondary compensation capacitance is independent of the primary one. However, the primary compensation capacitance depends on the secondary one. This result is demonstrated case by case for the four compensation topologies in this chapter.

4.2.1   Methodology for the efficiency-oriented compensation

The efficiency of the transformer is defined in (4.6). According to the development made in Chapter 3, all losses are generated in the two equivalent resistances of the coils R_1 and R_2. Thus, (4.6) can be rewritten as shown in (4.7).

$$\eta = \frac{P_L}{P_{in}} \qquad (4.6) \qquad\qquad \eta = \frac{P_L}{P_L + P_{loss}} \text{ with } P_{loss} = R_1 I_1^2 + R_2 I_2^2 \qquad (4.7)$$

The goal of this compensation is to maximize the transformer efficiency for a given load power P_L, which consists in minimizing P_{loss}. For this purpose, the currents I_1 and I_2 are to be minimized for a

given transmitted power, as suggested in (4.8).

$$\begin{cases} \left.\dfrac{\partial I_1}{\partial C_2}\right|_{P_L = Cte} = 0 \\[2ex] \left.\dfrac{\partial I_1}{\partial C_2}\right|_{C_2 = C_{2,opt}} < 0 \end{cases} \tag{4.8}$$

Determination of the secondary compensation capacitance using a serial secondary compensation

The secondary compensation capacitance for a serial secondary compensation calculation is presented in this section. The equivalent electric circuit for the secondary part of the transformer is shown in Fig. 4.2. The load power and the primary current are deduced from the equivalent circuit in (4.9) and (4.10).
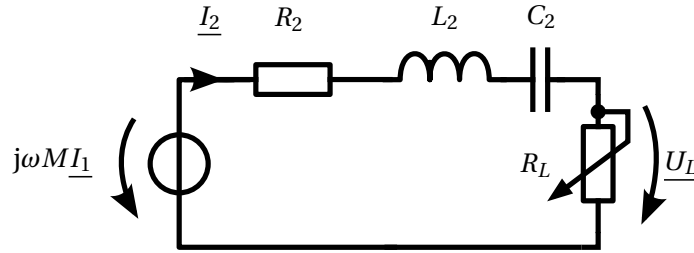
Figure 4.2: Electric equivalent circuit of the secondary part of the transformer

$$P_L = \frac{R_L \omega^2 M^2 I_1^2}{(R_L + R_2)^2 + (\omega L_2 - (\omega C_2)^{-1})^2} \tag{4.9}$$

$$I_1 = \sqrt{P_L \frac{(R_L + R_2)^2 + (\omega L_2 - (\omega C_2)^{-1})^2}{R_L \omega^2 M^2}} \tag{4.10}$$

The optimal secondary compensation capacitance C_2 (also denoted $C_{2,opt}$) for efficiency-oriented operation is obtained by solving (4.8) with (4.10). The result is given in (4.11).

$$C_2 = \frac{1}{\omega^2 L_2} \tag{4.11}$$

$$\left.\frac{\partial^2 I_1}{\partial^2 C_2}\right|_{C_2 = C_{2,opt}} = \frac{L_2^4 \omega_0^6 \sqrt{\dots}}{(\dots)^2} \tag{4.12}$$

The second differentiation of the primary current I_1 regarding the secondary capacitance C_2 evaluated using (4.11) is given in (4.12). A simple sign analysis reveals that this function is positive. As a result, this analysis confirms that the extremum of the current is a minimum.

55

Determination of the secondary compensation capacitance using a parallel secondary compensation

This section computes the secondary compensation capacitance for a parallel secondary compensation. The equivalent electric circuit for the secondary part of the transformer is shown in Fig. 4.3. The load power and the primary current are deduced from the equivalent circuit in (4.13) and (4.14).
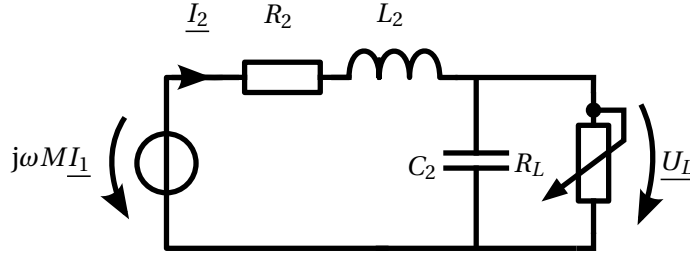
Figure 4.3: Electric equivalent circuit of the secondary part of the transformer

$$P_L = \frac{R_L I_1^2 M^2 \omega^2}{(L_2 + C_2 R_L R_2)^2 \omega^2 + (R_L + R_2 - C_2 L_2 R_L \omega^2)^2} \tag{4.13}$$

$$I_1 = \sqrt{P_L \frac{(L_2 + C_2 R_L R_2)^2 \omega^2 + (R_L + R_2 - C_2 L_2 R_L \omega^2)^2}{R_L \omega^2 M^2}} \tag{4.14}$$

The optimal secondary compensation capacitance C_2 for efficiency-oriented operation is obtained by solving (4.8) with (4.14). The result is given in (4.15). If $R_2 \ll L_2 \omega$, which is the case for almost all contactless systems, the result is the same than for a serial secondary compensation, defined in (4.11).

$$C_2 = \frac{L_2}{R_2^2 + L_2^2 \omega^2} \tag{4.15}$$

$$\frac{\partial^2 I_1}{\partial^2 C_2}\Big|_{C_2 = C_{2,opt}} = \frac{P_L^2 (\dots)^2}{(\dots)^4 (\dots)^{1.5}} \tag{4.16}$$

The second differentiation of the primary current I_1 regarding the secondary capacitance C_2 evaluated using (4.15) is given in (4.16). A simple sign analysis reveals that this function is positive. As a result, this analysis confirms that the extremum of the current is a minimum.

Determination of the primary compensation capacitance

For both serial and parallel secondary compensations, the primary capacitance does not change the efficiency of the transformer but its power factor. In order to cancel all the reactive power, this

capacitance can be computed solving (4.17).

$$\text{Im}(\underline{Z_t}(C_1)) = 0 \tag{4.17}$$

In some very special designs, in particular when the secondary part is uncompensated or detuned, the value of C_1 may be negative. In this case, a compensation inductance should be placed instead of a capacitance.

4.2.2 Methodology for control-oriented compensation

Unlike the efficiency-oriented compensation, the aim of the control-oriented one is not to maximize the efficiency of the transformer, but to simplify its control. Indeed, as developed in Section 4.4, the value of the primary compensation capacitance can be function of the load resistance R_L and/or the mutual inductance M, depending on the topologies. Moreover, the maximum reachable efficiency under these conditions is desired. These three criteria are listed in (4.18). However, this system leads to a number of constraints higher than its two degrees of freedom (C_1 and C_2). There is no solution, except if the equations of the system are linear dependant. Unfortunately, no analytical approach have been found to determine the value of these capacitances. As a result, a graphical approach, depending of the compensation topology is proposed in Section 4.4.

$$
\begin{cases}
\dfrac{\partial C_i}{\partial R_L} = 0 \, \forall R_L \in \mathbb{R}^+, i = 1, 2 \\[2ex]
\dfrac{\partial C_i}{\partial M} = 0 \, \forall M, i = 1, 2 \\[2ex]
\text{Im}(\underline{Z_t}) = 0
\end{cases}
\tag{4.18}
$$

4.3 Compensation topologies

This section presents the main capacitive compensation topologies. Fig. 4.4 introduces the compensated transformer structure. The equivalent secondary impedance, which contains the secondary self inductance L_2, the secondary capacitance C_2 and the load R_L is denoted $\underline{Z_2}$. The equivalent impedance of the whole transformer, which includes the reflected secondary part is denoted $\underline{Z_t}$.

On each side of the transformer, the capacitance can be placed in series or in parallel with the corresponding coils. It gives the four main compensation topologies, presented in Fig. 4.5 (S refers to a serial compensation while P refers to a parallel compensation).

Alternatively, the secondary inductance can also remain uncompensated, as proposed in [20]. Such a system is simplified because the compensation at the secondary side is removed. However, its performances are decreased compared to a fully compensated one. This is due to the reactive power flowing in the transformer. Only the topologies compensated at both primary and secondary sides are studied without lack of generality. Indeed, the special case of the uncompensated transformer at the
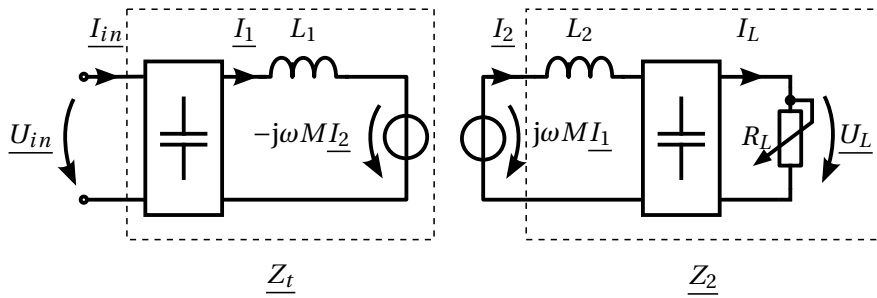
Figure 4.4: Overview of a capacitive compensated transformer
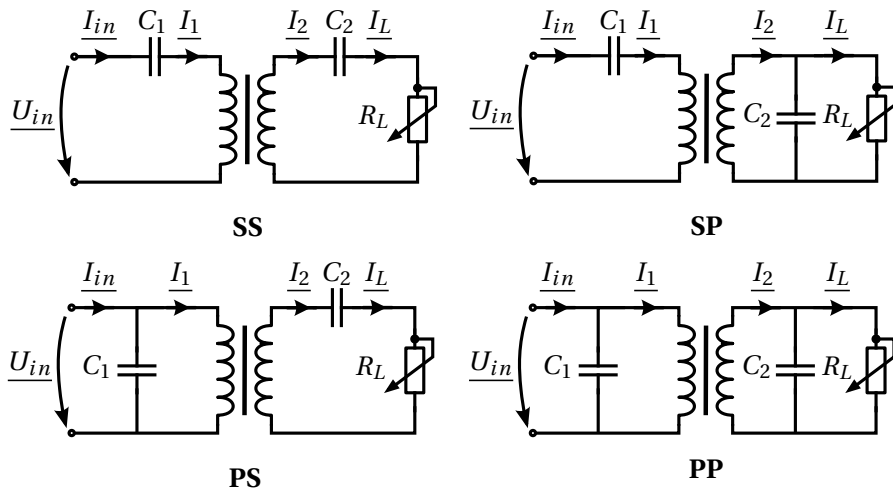
Figure 4.5: The four main compensation topologies

secondary side can be obtain when $C_2 \to \infty$ for a serial compensation and $C_2 \to 0$ for a parallel one.

4.4 Modelling of the main compensation topologies

In this section, the main parameters of the transformer are studied for the four main compensation topologies described in Fig. 4.5. For each topology, the following parameters are investigated :

- The compensation capacitances for the efficiency-oriented and control-oriented operations described in Section 4.2 are computed.

- The impedances of the transformer, which can be deduced solving the electric equivalent circuit of the compensated transformer.

- The efficiency of the transformer, computed using (4.7). This development is detailed for the SS topology. For the other topologies, the methodology is the same but numerical methods should be used because its resolution leads to very complex and unworkable expressions.

- The load characteristics are determined solving the electric equivalent circuit of the compensated transformer. It is made for the following control strategies :

    1. The supply voltage U_{in} is imposed,

    2. The supply current I_{in} is imposed,

    3. The current in the primary coil I_1 is imposed.

- Some stability considerations can be made out from the impedance formulas (behaviour when the load is disconnected, short-circuited or when the secondary part is removed).

For all the topologies studied, the compensation capacitances C_1 and C_2 are computed taking into account the serial resistances of the coils R_1 and R_2. The impedances, the supply current I_{in} and the currents flowing in the coils (I_1 and I_2) are computed. The resistances of the coils are supposed to be negligible regarding their respective reactances. This hypothesis is satisfied for a high efficiency transformer. If not, a numerical approach should be used. This analysis taking into account these resistances is made for SS topology as an example because the analytical solution is simpler than for the other topologies.

In practice, the resistances R_1 and R_2 can be very often neglected for relative high power transmission ($> 100\,\mathrm{W}$). For low power transmission or low efficiency systems, these resistances should be taken into account to obtain more accurate results.

4.4.1   Study of SS topology

The equivalent electric circuit of a SS topology compensated transformer is shown in Fig. 4.6.
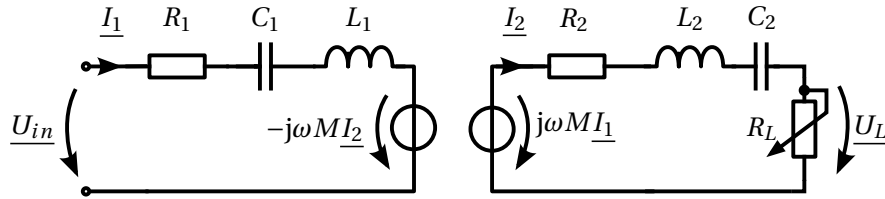
Figure 4.6: Electric equivalent circuit of a SS compensated transformer

The equivalent impedances of the transformer can be deduced by solving the circuit given in Fig. 4.6.

$$
\begin{cases}
\underline{Z_2} = R_2 + \mathrm{j}(\omega L_2 - \dfrac{1}{\omega C_2}) + R_L \\[2ex]
\underline{Z_R} = \dfrac{\omega^2 M^2}{\underline{Z_2}} \\[2ex]
\underline{Z_t} = R_1 + \mathrm{j}(\omega L_1 - \dfrac{1}{\omega C_1}) + \underline{Z_R}
\end{cases}
\tag{4.19}
$$

The optimal primary compensation capacitance C_1 for efficiency-oriented operation is obtained by solving (4.17) with (4.19). The result is given in (4.21).

$$C_2 = \frac{1}{\omega_0^2 L_2} \qquad (4.20) \qquad\qquad C_1 = \frac{1}{\omega_0^2 L_1} \qquad (4.21)$$

The impedances presented in (4.19) are simplified in (4.22) and (4.23) using optimal compensation capacitances defined in (4.11) and (4.21). The corresponding primary and secondary currents are shown in (4.24), and in (4.25) neglecting the resistances R_1 and R_2.

$$\begin{cases} \underline{Z_2} = R_2 + R_L \\[2ex] \underline{Z_R} = \dfrac{\omega_0^2 M^2}{R_2 + R_L} \\[2ex] \underline{Z_t} = R_1 + \dfrac{\omega_0^2 M^2}{R_2 + R_L} \end{cases} \qquad (4.22) \qquad\qquad \begin{cases} \lim\limits_{\substack{R_1 \to 0 \\ R_2 \to 0}} \underline{Z_2} = R_L \\[2ex] \lim\limits_{\substack{R_1 \to 0 \\ R_2 \to 0}} \underline{Z_R} = \dfrac{\omega_0^2 M^2}{R_L} \\[2ex] \lim\limits_{\substack{R_1 \to 0 \\ R_2 \to 0}} \underline{Z_t} = \dfrac{\omega_0^2 M^2}{R_L} \end{cases} \qquad (4.23)$$

$$\begin{cases} \underline{I_1} = \dfrac{\underline{U_{in}}(R_2 + R_L)}{\omega_0^2 M^2 + R_1(R_2 + R_L)} \\[3ex] \underline{I_2} = \dfrac{j\omega_0 M \underline{U_{in}}(R_2 + R_L)}{R_L \omega_0^2 M^2 + R_1 R_L (R_2 + R_L)} \end{cases} \qquad (4.24) \qquad \begin{cases} \lim\limits_{\substack{R_1 \to 0 \\ R_2 \to 0}} \underline{I_1} = \dfrac{\underline{U_{in}} R_L}{\omega_0^2 M^2} \\[3ex] \lim\limits_{\substack{R_1 \to 0 \\ R_2 \to 0}} \underline{I_2} = \dfrac{j\underline{U_{in}}}{\omega_0 M} \end{cases} \qquad (4.25)$$

Some relevant remarks can be made analysing the simplified form of the equivalent impedances. First of all, the equivalent impedance of the whole transformer $\underline{Z_t}$ is inversely proportional to the load resistance R_L. Thus, the transformer can be short-circuited if it is driven by a constant voltage because the current $\underline{I_1}$ becomes zero. Removing the load or the secondary part of the transformer leads to a huge primary current (theoretically infinity) if the voltage U_{in} is imposed. In practice, a proper protection should be placed in order to limit the primary current I_1.

Determination of the efficiency

The efficiency of the transformer can immediately be computed applying (4.7) and (4.25). It leads to (4.26).

$$\eta = \frac{\omega_0^2 M^2 R_L}{R_1 R_L^2 + \omega_0^2 M^2 (R_2 + R_L)} \qquad (4.26)$$

One can see that the transformer efficiency is function of the load R_L. Moreover, it increases up to $\eta = \frac{R_L}{R_2 + R_L}$ when the frequency increases. The compensation capacitances are only function of the operating pulsation ω and the self inductances L_1 and L_2. As a result, this compensation satisfies all the constraints presented in (4.18). For this reason, this is both an efficiency and control-oriented compensation.

Determination of the load characteristics

The load characteristics are determined solving the electric equivalent circuit presented in Fig. 4.6. This is done using the compensation capacitances determined in (4.11) and (4.21). The results are given in (4.27) (U_{in} imposed) and (4.30) (I_1 imposed).

When $R_1 \to 0$, $R_2 \to 0$ and U_{in} is imposed, the transformer acts as an ideal current source, as suggested in (4.28).

$$U_L(I_L) = \frac{MU_{in}\omega_0}{R_1} - \frac{M^2\omega_0^2 + R_1R_2}{R_1}I_L \quad (4.27) \qquad \lim_{\substack{R_1 \to 0 \\ R_2 \to 0}} I_L = \frac{U_{in}}{M\omega_0} \qquad (4.28)$$

In most ICPT designs, the resistance of the coils is very low compared to the mutual impedance ($M^2\omega_0^2 \gg R_1R_2$). Therefore, the output of the transformer acts as a quasi-ideal current source, as shown in (4.29).

$$I_L(U_L) = \frac{U_{in}}{M\omega_0} - \frac{R_1}{M^2\omega_0^2}U_L \qquad (4.29)$$

When the transformer is driven by a current source (I_1 imposed), it acts as a voltage source. If the voltage across the resistance R_2 is negligible regarding to the induced voltage of the secondary coil ($R_2I_L \ll \omega M I_1$), it acts as an ideal voltage source, as suggested in (4.31).

$$U_L = \omega_0 M I_1 - R_2 I_L \qquad (4.30) \qquad \lim_{R_2 \to 0} U_L = \omega_0 M I_1 \qquad (4.31)$$

4.4.2 Study of PS topology

The equivalent electric circuit of a PS topology compensated transformer is shown in Fig. 4.7.
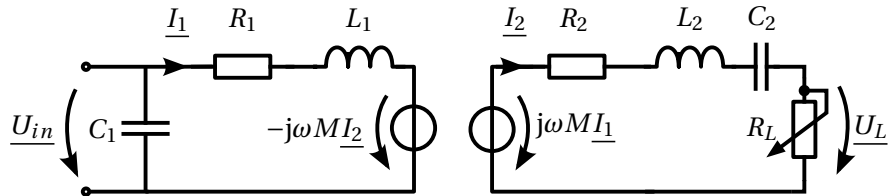
Figure 4.7: Electric equivalent circuit of a PS compensated transformer

The impedances can be deduced solving the circuit given in Fig. 4.7.

$$\begin{cases} \underline{Z_2} = R_2 + j(\omega L_2 - \dfrac{1}{\omega C_2}) + R_L \\[3mm] \underline{Z_R} = \dfrac{\omega^2 M^2}{\underline{Z_2}} \\[3mm] \underline{Z_t} = \dfrac{(\omega C_1)^{-1}(R_1 + j\omega L_1 + \underline{Z_R})}{R_1 + j\omega L_1 + (\omega C_1)^{-1} + \underline{Z_R}} \end{cases} \tag{4.32}$$

Efficiency-oriented compensation

The optimal primary compensation capacitance C_1 for efficiency-oriented operation is obtained solving (4.17) applied with (4.32). The result is given in (4.34). If the resistances R_1 and R_2 are negligible, (4.34) can be simplified as shown in (4.35).

$$C_2 = \frac{1}{\omega_0^2 L_2} \quad \text{(4.33)} \qquad C_1 = \frac{L_1(R_2 + R_L)^2}{R_1^2(R_2 + R_L)^2 + 2M^2 R_1(R_2 + R_L)\omega_0^2 + L_1^2(R_2 + R_L)^2\omega_0^2 + M^4\omega_0^4} \tag{4.34}$$

$$\lim_{\substack{R_1 \to 0 \\ R_2 \to 0}} C_1 = \frac{L_1 R_L^2}{L_1^2 R_L^2 \omega_0^2 + M^4 \omega_0^4} \quad \text{(4.35)}$$

The impedances presented in (4.32) are simplified in (4.36) using optimal compensation capacitances defined in (4.33) and (4.34). The serial resistances of the coils R_1 and R_2 are supposed to be negligible. The corresponding primary and secondary currents under this hypothesis are shown in (4.37).

$$\begin{cases} \lim_{\substack{R_1 \to 0 \\ R_2 \to 0}} \underline{Z_2} = R_L \\[3mm] \lim_{\substack{R_1 \to 0 \\ R_2 \to 0}} \underline{Z_R} = \dfrac{\omega_0^2 M^2}{R_L} \\[3mm] \lim_{\substack{R_1 \to 0 \\ R_2 \to 0}} \underline{Z_t} = \dfrac{R_L^2 L_1^2 + M^4 \omega_0^2}{R_L M^2} \end{cases} \tag{4.36} \qquad \begin{cases} \lim_{\substack{R_1 \to 0 \\ R_2 \to 0}} \underline{I_{in}} = \dfrac{\underline{U_{in}} R_L M^2}{R_L^2 L_1^2 + M^4 \omega_0^2} \\[3mm] \lim_{\substack{R_1 \to 0 \\ R_2 \to 0}} \underline{I_1} = \dfrac{j R_L \underline{U_{in}}}{j \omega_0^2 M^2 - L_1 R_L \omega_0} \\[3mm] \lim_{\substack{R_1 \to 0 \\ R_2 \to 0}} \underline{I_2} = \dfrac{M \underline{U_{in}}}{L_1 R_L - j \omega_0 M^2} \end{cases} \tag{4.37}$$

Unlike the SS topology, the equivalent impedance $\underline{Z_t}$ is very large if the load resistance R_L becomes infinite and/or the mutual inductance M becomes zero. The supply current I_{in} is very small (zero in theory) in these cases. However, the expression of the current $\underline{I_1}$ flowing in the primary coil reveals that a large value of R_L or a small value of the mutual inductance M leads to a very large current in the coil (infinite in theory). In practice, only the resistance R_1 of the coil limits this current. As a result, the primary coil should be oversized if this scenario can occur. When the transformer is short-circuited, the supply current I_{in} becomes very small (zero in theory).

Control-oriented compensation

Unlike for the SS topology, the efficiency-oriented compensation does not satisfy the criteria of control-oriented compensation. An intuitive control-oriented compensation can be made solving the electric equivalent circuit shown in Fig. 4.8. The parameters of this model are defined in Section 3.4.4. Intuitively, C_2 should compensates L_f and C_1 should compensate L_1. Applying this methodology leads to (4.38) and (4.39).
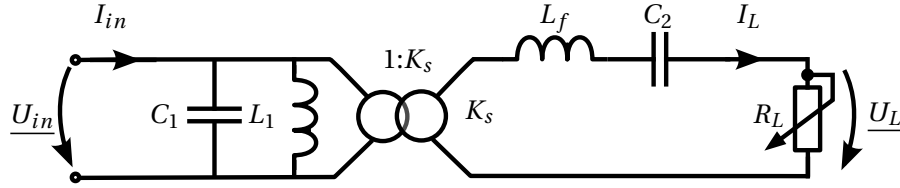
Figure 4.8: The equivalent circuit used to determine the control-oriented compensation

$$\lim_{\substack{R_1 \to 0 \\ R_2 \to 0}} C_2 = \frac{L_1}{(L_1 L_2 - M^2)\omega_0^2} \quad (4.38) \qquad \lim_{\substack{R_1 \to 0 \\ R_2 \to 0}} C_1 = \frac{1}{\omega_0^2 L_1} \quad (4.39)$$

The impedances of the transformer using compensation capacitances defined in (4.38) and (4.39) are presented in (4.40). The serial resistances of the coils R_1 and R_2 are supposed to be negligible. The corresponding currents in these conditions are shown in (4.41). As expected, the value of the capacitances C_1 and C_2 are not function of the load value R_L.

$$\begin{cases} \lim_{\substack{R_1 \to 0 \\ R_2 \to 0}} \underline{Z_2} = R_L + j\omega_0 \frac{M^2}{L_1} \\[2ex] \lim_{\substack{R_1 \to 0 \\ R_2 \to 0}} \underline{Z_R} = \frac{\omega_0^2 M^2 L_1}{R_L L_1 + j\omega_0 M^2} \\[2ex] \lim_{\substack{R_1 \to 0 \\ R_2 \to 0}} \underline{Z_t} = \frac{L_1^2 R_L}{M^2} \end{cases} \quad (4.40) \qquad \begin{cases} \lim_{\substack{R_1 \to 0 \\ R_2 \to 0}} \underline{I_{in}} = \frac{U_{in} M^2}{L_1^2 R_L} \\[2ex] \lim_{\substack{R_1 \to 0 \\ R_2 \to 0}} \underline{I_1} = \frac{(M^2 \omega_0 - jL_1 R_L)U_{in}}{L_1^2 R_L \omega_0} \\[2ex] \lim_{\substack{R_1 \to 0 \\ R_2 \to 0}} \underline{I_2} = \frac{M U_{in}}{L_1 R_L} \end{cases} \quad (4.41)$$

Determination of the load characteristics

The load characteristics are determined solving the electric equivalent circuit presented in Fig. 4.7. This is done using the compensation capacitances determined for both efficiency-oriented compensation (4.33) and (4.35) and control-oriented compensation (4.38) and (4.39). The results are given in (4.42) (U_{in} imposed) and (4.43) (I_{in} imposed).

For a fixed supply voltage U_{in} :

$$\lim_{\substack{R_1 \to 0 \\ R_2 \to 0}} U_L = \frac{M}{L_1}\sqrt{U_{in}^2 - M^2\omega_0^2 I_L^2} \quad \text{for efficiency-oriented compensation } (U_{in}\text{fixed})$$

$$\lim_{\substack{R_1 \to 0 \\ R_2 \to 0}} U_L = \frac{M}{L_1} U_{in} \qquad\qquad \text{for control-oriented compensation } (U_{in}\text{fixed}) \qquad (4.42)$$

For a fixed supply current I_{in} :

$$\lim_{\substack{R_1 \to 0 \\ R_2 \to 0}} U_L = \frac{M}{L_1}\sqrt{U_{in}^2 - M^2\omega_0^2 I_L^2} \quad \text{for efficiency-oriented compensation } (I_{in}\text{fixed})$$

$$\lim_{\substack{R_1 \to 0 \\ R_2 \to 0}} I_L = \frac{L_1}{M} I_{in} \qquad\qquad \text{for control-oriented compensation } (I_{in}\text{fixed}) \qquad (4.43)$$

4.4.3 Study of SP topology

The equivalent electric circuit of a SP topology compensated transformer is shown in Fig. 4.9.
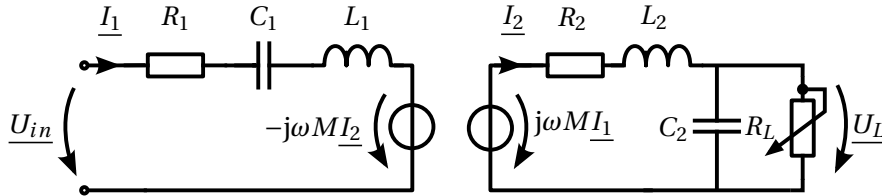
Figure 4.9: Electric equivalent circuit of a SP compensated transformer

The impedances can be deduced solving the circuit given in Fig. 4.9.

$$
\begin{cases}
\underline{Z_2} = R_2 + j\omega L_2 + \dfrac{R_L}{1 + j\omega_0 R_L C_2} \\[3mm]
\underline{Z_R} = \dfrac{\omega^2 M^2}{\underline{Z_2}} \\[3mm]
\underline{Z_t} = R_1 + j(\omega L_1 - \dfrac{1}{\omega C_1}) + \underline{Z_R}
\end{cases}
\qquad (4.44)
$$

The optimal primary compensation capacitance C_1 for efficiency-oriented operation is obtained solving (4.17) applied with (4.44). The result is given in (4.46).

$$C_2 = \frac{L_2}{R_2^2 + L_2^2 \omega^2} \tag{4.45}$$

$$C_1 = ((R_2^2 + L_2^2 \omega^2)(R_2(R_L + R_2) + L_2^2 \omega^2))(L_1 R_2^3 (R_L + R_2)\omega^2$$
$$+ L_2 R_2 (M^2(R_L - R_2) + L_1 L_2(R_L + 2R_2))\omega^4 + L_2^3(L_1 L_2 - M^2)\omega^6)^{-1} \tag{4.46}$$

$$\lim_{\substack{R_1 \to 0 \\ R_2 \to 0}} C_1 = \frac{L_2}{(L_1 L_2 - M^2)\omega_0^2} \tag{4.47}$$

The impedances presented in (4.44) are simplified in (4.48) using optimal compensation capacitances defined in (4.45) and (4.47), and assuming that the serial resistances of the coils R_1 and R_2 are negligible. The corresponding primary and secondary currents in these conditions are shown in (4.49).

$$\begin{cases} \lim_{\substack{R_1 \to 0 \\ R_2 \to 0}} \underline{Z_2} = \frac{\omega_0^2 L_2^2}{R_L - j\omega_0 L_2} \\[2ex] \lim_{\substack{R_1 \to 0 \\ R_2 \to 0}} \underline{Z_R} = \frac{M^2(R_L - j\omega_0 L_2)}{L_2^2} \\[2ex] \lim_{\substack{R_1 \to 0 \\ R_2 \to 0}} \underline{Z_t} = \frac{M^2 R_L}{L_2^2} \end{cases} \tag{4.48}$$
$$\begin{cases} \lim_{\substack{R_1 \to 0 \\ R_2 \to 0}} \underline{I_{in}} = \frac{U_{in} L_2^2}{M^2 R_L} \\[2ex] \lim_{\substack{R_1 \to 0 \\ R_2 \to 0}} \underline{I_2} = \frac{\omega_0 L_2^2 \underline{U_{in}}}{M R_L (\omega_0 L_2 - jR_L)} \\[2ex] \lim_{\substack{R_1 \to 0 \\ R_2 \to 0}} \underline{I_L} = \frac{L_2 \underline{U_{in}}(\omega_0 L_2 + jR_L)}{M R_L (\omega_0 L_2 - jR_L)} \end{cases} \tag{4.49}$$

As the PS topology, the equivalent impedance of the whole transformer $\underline{Z_t}$ decreases to zero when the load resistance decreases to zero. If the transformer is short-circuited, the supply current should be limited. As for the SS topology, the impedance $\underline{Z_t}$ becomes zero when the secondary part is removed ($M = 0$). Finally, when no load is connected to the secondary coil $R_L \to \infty$ the supply current decreases to zero.

One can see that the compensation capacitance C_2 depends only on the self inductances L_2 and the resistance R_2. If the resistances R_1 and R_2 are neglected, the primary capacitance C_1 is function of the mutual inductance M but not of the load resistance R_L. Indeed, it satisfies the criteria given in (4.18), except the mutual inductance dependency.

Load characteristics

The load characteristics are determined solving the electric equivalent circuit presented in Fig. 4.6. This is done using the compensation capacitances determined in (4.15) and in (4.46). The result is given in (4.50) if the transformer is driven by an imposed voltage (U_{in} fixed) and in (4.52) if the transformer is

driven by an imposed supply current (I_{in} fixed).

$$U_L(I_L) = \frac{(R_2^2 + L_2^2\omega_0^2)(MR_2^2 U_{in} - L_2^2 MU_{in}\omega_0^2)}{L_2 R_1 R_2^3 + L_2^3(R_1 R_2\omega_0^2 + M^2\omega_0^4)} - \frac{(R_2^2 + L_2^2\omega_0^2)(L_2 R_1 R_2^2 + L_2^3 R_1\omega_0^2 + L_2 M^2 R_2\omega_0^2)}{L_2 R_1 R_2^3 + L_2^3(R_1 R_2\omega_0^2 + M^2\omega_0^4)} I_L \tag{4.50}$$

When $R_1 \to 0$ and $R_2 \to 0$, the transformer acts as an ideal voltage source, as suggested in (4.51).

$$\lim_{\substack{R_1 \to 0 \\ R_2 \to 0}} U_L = \frac{L_2 U_{in}}{M} \qquad \text{for a fixed voltage supply} \tag{4.51}$$

$$\lim_{\substack{R_1 \to 0 \\ R_2 \to 0}} I_L = \frac{M}{L_2} I_{in} \qquad \text{for a fixed current supply} \tag{4.52}$$

4.4.4 Study of PP topology

The equivalent electric circuit of a PP topology compensated transformer is shown in Fig. 4.10.
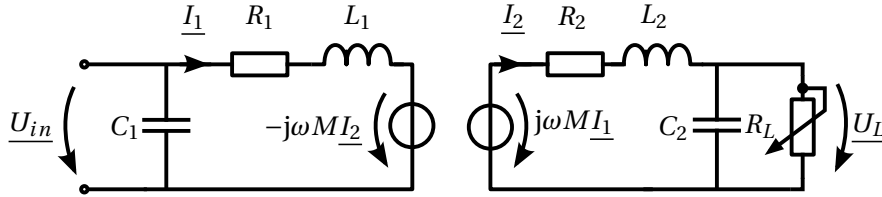
Figure 4.10: Electric equivalent circuit of a PP compensated transformer

The impedances can be deduced solving the circuit given in Fig. 4.10.

$$\begin{cases} \underline{Z_2} = R_2 + j\omega L_2 + \dfrac{R_L}{1 + j\omega_0 R_L C_2} \\[3mm] \underline{Z_R} = \dfrac{\omega^2 M^2}{\underline{Z_2}} \\[3mm] \underline{Z_t} = \dfrac{(\omega C_1)^{-1}(R_1 + j\omega L_1 + \underline{Z_R})}{R_1 + j\omega L_1 + (\omega C_1)^{-1} + \underline{Z_R}} \end{cases} \tag{4.53}$$

The optimal primary compensation capacitance C_1 for efficiency-oriented operation is obtained solving (4.17) applied with (4.53). The result is given in (4.55), assuming that the resistances R_1 and R_2 are negligible (the computation taking these resistances into account should be made using numeric

methods due to the complexity of its determination).

$$C_2 = \frac{L_2}{R_2^2 + L_2^2 \omega^2} \tag{4.54}$$

$$\lim_{\substack{R_1 \to 0 \\ R_2 \to 0}} C_1 = \frac{L_2^3 (L_1 L_2 - M^2)}{M^4 R_L^2 + L_2^2 (M^2 - L_1 L_2)^2 \omega^2} \tag{4.55}$$

The impedances presented in (4.53) are simplified in (4.56) using optimal compensation capacitances defined in (4.54) and (4.55). The corresponding currents in these conditions are shown in (4.57).

$$\begin{cases} \lim_{\substack{R_1 \to 0 \\ R_2 \to 0}} \underline{Z_2} = \dfrac{\omega_0^2 L_2^2}{R_L - j\omega_0 L_2} \\[3ex] \lim_{\substack{R_1 \to 0 \\ R_2 \to 0}} \underline{Z_R} = \dfrac{M^2 (R_L - j\omega_0 L_2)}{L_2^2} \\[3ex] \lim_{\substack{R_1 \to 0 \\ R_2 \to 0}} \underline{Z_t} = \dfrac{M^2 R_L}{L_2^2} + \dfrac{(M^2 - L_1 L_2)^2 \omega^2}{M^2 R_L} \end{cases} \tag{4.56}$$

$$\begin{cases} \lim_{\substack{R_1 \to 0 \\ R_2 \to 0}} \underline{I_{in}} = \dfrac{\underline{U_{in}} L_2^2 M^2 R_L}{M^4 R_L^2 + \omega_0^2 L_2^2 (M^2 - L_1 L_2)^2} \\[3ex] \lim_{\substack{R_1 \to 0 \\ R_2 \to 0}} \underline{I_1} = \dfrac{L_2^2 \underline{U_{in}}}{M^2 R_L + j\omega_0 L_2 (L_1 L_2 - M^2)} \\[3ex] \lim_{\substack{R_1 \to 0 \\ R_2 \to 0}} \underline{I_2} = \dfrac{j\omega_0 M L_2^2 \underline{U_{in}}}{(R_L + j\omega_0 L_2)(M^2 R_L + j\omega_0 L_2 (L_1 L_2 - M^2))} \\[3ex] \lim_{\substack{R_1 \to 0 \\ R_2 \to 0}} \underline{I_L} = -\dfrac{L_2 M \underline{U_{in}} (R_L - j\omega_0 L_2)}{(R_L + j\omega_0 L_2)(M^2 R_L + j\omega_0 L_2 (L_1 L_2 - M^2))} \end{cases} \tag{4.57}$$

If the secondary part of the transformer is removed ($M \to 0$), the equivalent impedance of the whole transformer decreases to zero and the supply current should be limited. The same behaviour occurs if the load is removed ($R_L \to \infty$).

Control-oriented compensation

The primary compensation capacitance determined for efficiency-oriented operation is function of both the mutual inductance M and the load resistance R_L.

The control-oriented compensation proposed is to use the same secondary compensation capacitances as for SP topology. The primary capacitance C_1 is independent of the load resistance R_L, but the imaginary part is only partially cancelled.

$$\lim_{\substack{R_1 \to 0 \\ R_2 \to 0}} C_2 = \frac{1}{\omega_0^2 L_2} \qquad (4.58) \qquad \lim_{\substack{R_1 \to 0 \\ R_2 \to 0}} C_1 = \frac{L_2}{(L_1 L_2 - M^2)\omega_0^2} \qquad (4.59)$$

The impedances of the transformer using compensation capacitances defined in (4.58) and (4.59) are presented in (4.60). The corresponding currents in these conditions are shown in (4.61).

$$\begin{cases} \lim_{\substack{R_1 \to 0 \\ R_2 \to 0}} \underline{Z_2} = \frac{(\omega_0 L_2)^2}{R_L - j\omega_0 L_2} \\[2ex] \lim_{\substack{R_1 \to 0 \\ R_2 \to 0}} \underline{Z_R} = \frac{\omega_0^2 M^2}{\underline{Z_2}} \\[2ex] \lim_{\substack{R_1 \to 0 \\ R_2 \to 0}} \underline{Z_t} = \frac{(-L_1 L_2 + M^2)^2 \omega_0^2}{M^2 R_L} + j\omega_0 \frac{L_1 M^2 - L_1 L_2}{L_1 L_2} \end{cases} \qquad (4.60)$$

$$\begin{cases} \lim_{\substack{R_1 \to 0 \\ R_2 \to 0}} \underline{I_{in}} = \frac{L_2 M^2 R_L \underline{U_{in}}}{\omega_0 (M^2 - L_1 L_2)(\omega_0 L_2 (M^2 - L_1 L_2) + j M^2 R_L)} \\[2ex] \lim_{\substack{R_1 \to 0 \\ R_2 \to 0}} \underline{I_1} = \frac{L_2^2 \underline{U_{in}}}{M^2 R_L + j\omega_0 (L_1 L_2 - M^2)} \\[2ex] \lim_{\substack{R_1 \to 0 \\ R_2 \to 0}} \underline{I_2} = \frac{j\omega_0 M L_2^2 \underline{U_{in}}}{(R_L + j\omega_0 L_2)(M^2 R_L + j L_2 (L_1 L_2 - M^2)\omega_0)} \\[2ex] \lim_{\substack{R_1 \to 0 \\ R_2 \to 0}} \underline{I_L} = -\frac{L_2 M R_L \underline{U_{in}}}{(R_L + j\omega_0 L_2)(M^2 R_L + j\omega_0 L_2 (L_1 L_2 - M^2))} \end{cases} \qquad (4.61)$$

Load characteristics

The load characteristics are determined solving the electric equivalent circuit presented in Fig. 4.10. This is done using the compensation capacitances determined for both efficiency-oriented compensation (4.54) and (4.55) and control-oriented compensation (4.58) and (4.59). The result is given in (4.62) (U_{in} imposed) and (4.63) (I_1 imposed).

For a fixed voltage supply U_{in} :

$$\lim_{\substack{R_1 \to 0 \\ R_2 \to 0}} U_L = \frac{L_2}{M^2} \sqrt{M^2 U_{in}^2 - (M^2 - L_1 L_2)^2 \omega_0^2 I_L^2} \quad \text{for efficiency-oriented compensation}$$

$$\lim_{\substack{R_1 \to 0 \\ R_2 \to 0}} I_L = \frac{M}{(L_1 L_2 - M^2)\omega_0} U_{in} \qquad \qquad \text{for control-oriented compensation} \qquad (4.62)$$

For a fixed current supply I_{in} :

$$\lim_{\substack{R_1 \to 0 \\ R_2 \to 0}} U_L = \frac{L_2(L_1 L_2 - M^2)\omega_0 I_{in} I_L}{\sqrt{(L_2 M)^2 I_L^2 - I_{in}^2 M^4}} \text{ for efficiency-oriented compensation}$$

$$\lim_{\substack{R_1 \to 0 \\ R_2 \to 0}} U_L = \frac{(L_1 L_2 - M^2)\omega_0}{M} I_{in} \qquad \text{for control-oriented compensation}$$

(4.63)

One can see that for both current controlled (I_{in} imposed) and voltage controlled (U_{in} imposed), the control-oriented compensation leads to a current source and voltage source respectively (if the resistances R_1 and R_2 are neglected). Nevertheless, the load voltage and current are function of the load for the efficiency-oriented compensation.

4.4.5   Comparison of the four main compensation topologies

The behaviour of the four compensation topologies studied in Section 4.4 are summarized in this section. In all the results, the serial resistances of the coils R_1 and R_2 are neglected. Table 4.1 presents the compensation capacitances for the four topologies and the two compensation methodologies studied.

Table 4.1: Determination of the compensation capacitances of the transformer

Topology	Efficiency-oriented		Control-oriented	
SS	$C_2 = \dfrac{1}{\omega_0^2 L_2}$	$C_1 = \dfrac{1}{\omega_0^2 L_1}$	$C_2 = \dfrac{1}{\omega_0^2 L_2}$	$C_1 = \dfrac{1}{\omega_0^2 L_1}$
SP	$C_2 = \dfrac{1}{\omega_0^2 L_2}$	$C_1 = \dfrac{L_2}{(L_1 L_2 - M^2)\omega_0^2}$	$C_2 = \dfrac{1}{\omega_0^2 L_2}$	$C_1 = \dfrac{L_2}{(L_1 L_2 - M^2)\omega_0^2}$
PS	$C_2 = \dfrac{1}{\omega_0^2 L_2}$	$C_1 = \dfrac{L_1 R_L^2}{L_1^2 R_L^2 \omega_0^2 + M^4 \omega_0^4}$	$C_2 = \dfrac{L_1}{(L_1 L_2 - M^2)\omega_0^2}$	$C_1 = \dfrac{1}{\omega_0^2 L_1}$
PP	$C_2 = \dfrac{1}{\omega_0^2 L_2^2}$	$C_1 = \dfrac{L_2^3(L_1 L_2 - M^2)}{M^4 R_L^2 + L_2^2(M^2 - L_1 L_2)^2 \omega_0^2}$	$C_2 = \dfrac{1}{\omega_0^2 L_2}$	$C_1 = \dfrac{L_2}{(L_1 L_2 - M^2)\omega_0^2}$

One can see that the capacitance values are the same for the two compensation methodologies for SS and SP topologies, while they are different for PS and PP topologies, especially for high-coupled transformer. The compensation of SS topology is the most robust and the simplest to implement since the values of the capacitances neither depend on the load resistance R_L nor the mutual inductance M. This result is still available if the resistances R_1 and R_2 are not neglected. For the other topologies, the primary capacitance C_1 is function of the mutual inductance M and the load resistance R_L for the efficiency-oriented compensation. Assuming that the resistances R_1 and R_2 are negligible, the capacitance C_1 is independent of the load resistance but depends on the mutual inductance M for the control-oriented one.

The equivalent impedances associated to the compensation topologies and methodologies are summarized in Table 4.2. As expected, the imaginary part of the equivalent impedance of the whole

transformer $\underline{Z_t}$ is zero in each case except for the PP topology using control-oriented compensation. This result was expected because all the reactive power is compensated by the capacitance C_1. The computation of these impedances is important to determine the response of the transformer when it is short-circuited, open-circuited and when the secondary coil is removed ($M \to 0$). This is detailed for each cases in Section 4.4.

The current flowing in the coils and the supply current are shown for each topologies and compensation methodologies in Table 4.3. The computation of the current flowing in the coils I_1 and I_2 is very important because it determines the minimal section of the conductors to get an acceptable current density. The supply current I_{in} is useful to design the power electronics (This is detailed in Chapter 3). One can see that for parallel compensation, the current flowing in the primary and secondary coil/capacitance respectively is higher than the supply and load current respectively. Using a serial compensation, the voltage across the primary and secondary coil/capacitance respectively is higher than the supply voltage for a serial compensation. The results of the load characteristics for each topologies and compensation methodologies and the different drives are summarized in Table 4.4.

Table 4.2: Determination of the equivalent impedances of the transformer

Topology	Efficiency-oriented	Control-oriented
SS	$\underline{Z_2} = R_L \quad \underline{Z_t} = \dfrac{\omega_0^2 M^2}{R_L}$	$\underline{Z_2} = R_L \quad \underline{Z_t} = \dfrac{\omega_0^2 M^2}{R_L}$
SP	$\underline{Z_2} = \dfrac{\omega_0^2 L_2^2}{R_L - j\omega_0 L_2} \quad \underline{Z_t} = \dfrac{M^2 R_L}{L_2^2}$	$\underline{Z_2} = \dfrac{\omega_0^2 L_2^2}{R_L - j\omega_0 L_2} \quad \underline{Z_t} = \dfrac{M^2 R_L}{L_2^2}$
PS	$\underline{Z_2} = R_L \quad \underline{Z_t} = \dfrac{R_L^2 L_1^2 + M^4 \omega_0^2}{R_L M^2}$	$\underline{Z_2} = R_L + j\omega_0 \dfrac{M^2}{L_1} \quad \underline{Z_t} = \dfrac{L_1^2 R_L}{M^2}$
PP	$\underline{Z_2} = \dfrac{\omega_0^2 L_2^2}{R_L - j\omega_0 L_2} \quad \underline{Z_t} = \dfrac{M^2 R_L}{L_2^2} + \dfrac{(M^2 - L_1 L_2)^2 \omega^2}{M^2 R_L}$	$\underline{Z_2} = \dfrac{\omega_0^2 L_2^2}{R_L - j\omega_0 L_2} \quad \underline{Z_t} = \dfrac{M^2 R_L}{L_2^2} + \dfrac{(M^2 - L_1 L_2)^2 \omega^2}{M^2 R_L}$

Table 4.3: Determination of the currents flowing in the transformer

Topology	Efficiency-oriented	Control-oriented
Transformer driven with a constant voltage U$_{in}$		
SS	$\underline{I_1} = \dfrac{U_{in} R_L}{\omega_0^2 M^2} \quad \underline{I_2} = j\dfrac{U_{in}}{\omega_0 M}$	$\underline{I_1} = \dfrac{U_{in} R_L}{\omega_0^2 M^2} \quad \underline{I_2} = j\dfrac{U_{in}}{\omega_0 M}$
SP	$\underline{I_1} = \dfrac{U_{in} L_2^2}{M^2 R_L} \quad \underline{I_2} = \dfrac{\omega_0 L_2^2 U_{in}}{MR_L(\omega_0 L_2 - jR_L)}$ $\underline{I_L} = \dfrac{L_2 U_{in}(\omega_0 L_2 + jR_L)}{MR_L(\omega_0 L_2 - jR_L)}$	$\underline{I_1} = \dfrac{U_{in} L_2^2}{M^2 R_L} \quad \underline{I_2} = \dfrac{\omega_0 L_2^2 U_{in}}{MR_L(\omega_0 L_2 - jR_L)}$ $\underline{I_L} = \dfrac{L_2 U_{in}(\omega_0 L_2 + jR_L)}{MR_L(\omega_0 L_2 - jR_L)}$
PS	$\underline{I_{in}} = \dfrac{U_{in} R_L M^2}{R_L^2 L_1^2 + M^4 \omega_0^2}$ $\underline{I_1} = \dfrac{jR_L U_{in}}{j\omega_0^2 M^2 - L_1 R_L \omega_0} \quad \underline{I_2} = \dfrac{M U_{in}}{L_1 R_L - j\omega_0 M^2}$	$\underline{I_{in}} = \dfrac{U_{in} M^2}{L_1^2 R_L}$ $\underline{I_1} = \dfrac{(M^2 \omega_0 - jL_1 R_L)U_{in}}{L_1^2 R_L \omega_0} \quad \underline{I_2} = \dfrac{M U_{in}}{L_1 R_L}$
PP	$\underline{I_{in}} = \dfrac{L_2 M^2 R_L U_{in}}{\omega_0(M^2 - L_1 L_2)(\omega_0 L_2(M^2 - L_1 L_2) + jM^2 R_L)}$ $\underline{I_1} = \dfrac{L_2^2 U_{in}}{M^2 R_L + j\omega_0 L_2(L_1 L_2 - M^2)}$ $\underline{I_2} = \dfrac{j\omega_0 M L_2^2 U_{in}}{(R_L + j\omega_0 L_2)(M^2 R_L + j\omega_0 L_2(L_1 L_2 - M^2))}$ $\underline{I_L} = -\dfrac{L_2 M U_{in}(R_L - j\omega_0 L_2)}{(R_L + j\omega_0 L_2)(M^2 R_L + j\omega_0 L_2(L_1 L_2 - M^2))}$	$\underline{I_{in}} = \dfrac{L_2 M^2 R_L U_{in}}{\omega_0(M^2 - L_1 L_2)(\omega_0 L_2(M^2 - L_1 L_2) + jM^2 R_L)}$ $\underline{I_1} = \dfrac{L_2^2 U_{in}}{M^2 R_L + j\omega_0 L_2(L_1 L_2 - M^2)}$ $\underline{I_2} = \dfrac{j\omega_0 M L_2^2 U_{in}}{(R_L + j\omega_0 L_2)(M^2 R_L + j\omega_0 L_2(L_1 L_2 - M^2))}$ $\underline{I_L} = -\dfrac{L_2 M U_{in}(R_L - j\omega_0 L_2)}{(R_L + j\omega_0 L_2)(M^2 R_L + j\omega_0 L_2(L_1 L_2 - M^2))}$

Table 4.4: Determination of the load characteristics of the transformer

Topology	Efficiency-oriented	Control-oriented
Transformer driven with a constant voltage U_{in}		
SS	$I_L = \dfrac{U_{in}}{M\omega_0}$	$I_L = \dfrac{U_{in}}{M\omega_0}$
PS	$U_L = \dfrac{M}{L_1}\sqrt{U_{in}^2 - M^2\omega_0^2 I_L^2}$	$U_L = \dfrac{M}{L_1}U_{in}$
SP	$U_L = \dfrac{L_2 U_{in}}{M}$	$U_L = \dfrac{L_2 U_{in}}{M}$
PP	$U_L = \dfrac{L_2}{M^2}\sqrt{M^2 U_{in}^2 - (M^2 - L_1 L_2)^2 \omega_0^2 I_L^2}$	$I_L = \dfrac{M}{(L_1 L_2 - M^2)\omega_0}U_{in}$
Transformer driven with a constant current I_{in}		
SS	$U_L = \omega_0 M I_1$	$U_L = \omega_0 M I_1$
PS	$I_L(U_L) = \dfrac{L_1}{M}I_{in}\dfrac{U_L}{\sqrt{U_L^2 - (M\omega_0 I_{in})^2}}$	$I_L = \dfrac{L_1}{M}I_{in}$
SP	$I_L = \dfrac{M}{L_2}I_{in}$	$I_L = \dfrac{M}{L_2}I_{in}$
PP	$U_L(I_L) = \dfrac{L_2(L_1 L_2 - M^2)\omega_0 I_{in} I_L}{\sqrt{(L_2 M)^2 I_L^2 - I_{in}^2 M^4}}$	$U_L = \dfrac{(L_1 L_2 - M^2)\omega_0}{M}I_{in}$
Transformer driven with a constant primary coil current I_1		
SS	$U_L = \omega_0 M I_1$	$U_L = \omega_0 M I_1$
PS	$U_L = \omega_0 M I_1$	$U_L = \omega_0 M I_1 - \dfrac{\omega_0 M^2}{L_1}I_L$
SP	$I_L = \dfrac{M}{L_2}I_1$	$I_L = \dfrac{M}{L_2}I_1$
PP	$I_L = \dfrac{M}{L_2}I_1$	$I_L = \dfrac{M}{L_2}I_1$

The load characteristics of the transformer are very important to model the transformer when the load resistance R_L is variable. The behaviour of the transformer can be either a voltage or current source for all topologies using the control-oriented compensation. Using the efficiency-oriented compensation leads to a current source for SS topology and a voltage source for PS topology. However, the load voltage U_L is function of the load current I_L for the SP and PP topology. One can note that for the two controls at imposed currents, an additional closed-loop control must be used.

4.5 Frequency response of the compensated transformer

In most literature and in all the development presented above, it is assumed that the transformer is excited at its "resonant frequency" ω_0. However, under specific conditions which are the object of the

study in this section, more than one resonant frequencies appear. This is the so-called bifurcation phenomenon. Although it is not well-studied, it is very important since the frequency response of the transformer is completely different when it works under bifurcation mode. Existing research has been investigated in [70] in order to determine the bifurcation conditions for the four main compensation topologies studied in the previous sections. However, several assumptions on the quality factor of the system have been made which restrict the domain of validity of these conditions. The aim of this section is to draw up general criteria without this lack of generality.

The extrema of the transmitted power P_L can be determined solving (4.64). However, this equation is very complex to solve in practice. Assuming that no losses are present in the transformer (i.e $R_1 \rightarrow 0$ and $R_2 \rightarrow 0$), it can be shown that alternatively, (4.65) is equivalent and easier to compute. The equivalence of these two equations is detailed in [70].

$$\frac{\mathrm{d}P_L}{\mathrm{d}\omega} = 0 \qquad (4.64) \qquad\qquad\qquad \mathrm{Im}(\underline{Z_t}) = 0 \qquad (4.65)$$

In order to determine the maxima of the load power when bifurcation phenomena occurs, (4.66) can be solved.

$$\frac{\mathrm{d}^2 P_L}{\mathrm{d}^2\omega} > 0 \qquad\qquad\qquad\qquad (4.66)$$

4.5.1 Study of the bifurcation phenomenon for the four topologies

The mode of operation depends on the number of solutions of (4.65). For "normal" operation (only one resonant frequency), the load power P_L has one extremum which is a maximum at the well-known resonant frequency. For bifurcation operation, the load power, function of the operating frequency, has three extrema. In this case, the second extremum is a minimum while the first and the third ones are the maxima. This is studied in this section.

The reflected impedance, function of the operating frequency and neglecting the resistance of the secondary coil R_2 is given in (4.67). It can be rewritten using the capacitance values computed in Section 4.3.

$$\underline{Z_R} = \begin{cases} \dfrac{C_2 M^2 \omega^3}{-\mathrm{j} + C_2\omega(R_L + \mathrm{j}\omega L_2)} & \text{for SS and PS} \\[2ex] \mathrm{j}\omega L_2 + \dfrac{\mathrm{j}R_L}{\mathrm{j} - \omega C_2 R_L} & \text{for SP and PP} \end{cases} \qquad (4.67)$$

$$\underline{Z_R} = \begin{cases} \dfrac{M^2 \omega^3}{R_L\omega + \mathrm{j}L_2(\omega^2 - \omega_0^2)} & \text{for SS and PS} \\[2ex] \mathrm{j}\omega L_2 + \dfrac{\mathrm{j}L_2 R_L \omega_0^2}{-R_L\omega + \mathrm{j}\omega_0^2 L_2} & \text{for SP and PP} \end{cases} \qquad (4.68)$$

In the upcoming development, the quality factors of the transformer are used. For a given impedance Z_i, it is defined as the ratio of its imaginary part and its real one, as suggested in (4.69). Indeed, the primary quality factor Q_1 and the secondary one Q_2 depends on the compensation topologies. Their expressions are given in Table 4.5.

$$Q_i = \frac{\text{Im}(Z_i)}{\text{Re}(Z_i)} \tag{4.69}$$

Table 4.5: Determination of the bifurcation criteria

Serial secondary	$Q_1 = \dfrac{L_1 R_L}{\omega_0 M^2}$	$Q_2 = \dfrac{\omega_0 L_2}{R_L}$
Parallel secondary	$Q_1 = \dfrac{\omega_0 L_1 L_2^2}{M^2 R_L}$	$Q_2 = \dfrac{R_L}{\omega_0 L_2}$

Development for SS topology

For the SS topology, the imaginary part of the equivalent impedance of the transformer $\underline{Z_t}$ is given in (4.70). The imaginary part of the numerator of this expression is then called the characteristic polynomial for bifurcation criteria determination.

$$\text{Im}(\underline{Z_t}) = \frac{(L_1 L_2^2 - L_2 M^2)\omega^6 + (L_1 R_L^2 - 3L_1 L_2^2 \omega_0^2 + L_2 M^2 \omega_0^2)\omega^4 + (3L_1 L_2^2 \omega_0^4 - L_1 R_L^2 \omega_0^2)\omega^2 - L_1 L_2^2 \omega_0^6}{\cdots} \tag{4.70}$$

One can see that the numerator of (4.70) is a polynomial of degree six but the odd terms are zero. Since only the positive pulsations ω are considered, it can be rewritten as follow ($\omega^2 \rightarrow X$) :

$$aX^3 + bX^2 + cX + d = 0 \tag{4.71}$$

$$\begin{cases} a = (L_1 L_2^2 - L_2 M^2) \\[2mm] b = (L_1 R_L^2 - 3L_1 L_2^2 \omega_0^2 + L_2 M^2 \omega_0^2) \\[2mm] c = (3L_1 L_2^2 \omega_0^4 - L_1 R_L^2 \omega_0^2) \\[2mm] d = -L_1 L_2^2 \omega_0^6 \end{cases} \tag{4.72}$$

The number of roots of (4.71) gives the bifurcation criteria. Since it is a polynomial of degree three, the Cardan's formulas are used to determine the number of real roots [3]. The discriminant for a polynomial

of degree three is given in (4.73). If this latter is positive, the polynomial has three real roots. Otherwise, it has one real root and two complex ones.

$$\Delta = -4(\frac{c}{a} - \frac{b^2}{3a^2})^3 - 27(\frac{b}{27a}(\frac{2b^2}{a^2} - \frac{9c}{a}) + \frac{d}{a})^2 \tag{4.73}$$

After development and simplification, applying (4.73) to (4.70) leads to (4.74).

$$\Delta = L_1\omega_0^4(L_1R_L^2 - L_2M^2\omega_0^2)^2(4L_2^3M^2\omega_0^4 + L_1(R_L^4 - 4L_2^2R_L^2\omega_0^2)) \tag{4.74}$$

Obviously, the sign of the discriminant is given by its third term, as suggested in (4.75).

$$\Delta > 0 \Leftrightarrow 4L_2^3M^2\omega_0^4 + L_1(R_L^4 - 4L_2^2R_L^2\omega_0^2) > 0 \tag{4.75}$$

Since the load R_L is positive, this condition can be expressed as a second order polynomial function of R_L, as suggested in (4.76) ($R_L^2 - > R\prime_L$).

$$L_1R\prime_L^2 - 4L_1L_2^2\omega_0^2R\prime_L + 4L_2^3M^2\omega_0^4 > 0 \tag{4.76}$$

Finally, the conditions on the load R_L for bifurcation phenomena for SS topology is given in (4.77).

$$R_L^2 < 2L_2^2\omega_0^2(1 - \frac{\sqrt{(L_1L_2 - M^2)}}{\sqrt{L_1L_2}}) \text{ or } R_L^2 > 2L_2^2\omega_0^2(1 + \frac{\sqrt{(L_1L_2 - M^2)}}{\sqrt{L_1L_2}}) \tag{4.77}$$

This condition can also be expressed in terms of quality factors. This is done in [69]. It leads to (4.78). The equivalence of (4.76) and (4.78) can be made by identification.

$$Q_1 < \frac{4Q_2^3}{4Q_2^2 - 1} \text{ with } Q_1 = \frac{L_1R_L}{\omega_0M^2} \text{ and } Q_2 = \frac{\omega_0L_2}{R_L} \tag{4.78}$$

Development for PS topology

For the PS topology, the imaginary part of the equivalent impedance of the transformer $\underline{Z_t}$ is given in (4.79).

$$\text{Im}(\underline{Z_t}) = \frac{a\omega^7 + b\omega^5 + c\omega^3 + d\omega}{\cdots} \tag{4.79}$$

One can see that the numerator of (4.70) is a polynomial of degree seven but it can be rewritten as a polynomial of degree three, as suggested in (4.80).

$$aX^3 + bX^2 + cX + d = 0 \tag{4.80}$$

$$
\begin{cases}
a = -L_1^5 L_2^2 R_L^4 \omega_0^2 + 2L_1^4 L_2 M^2 R_L^4 \omega_0^2 - L_1^3 M^4 R_L^4 \omega_0^2 - L_1^3 L_2^2 M^4 R_L^2 \omega_0^4 + 2L_1^2 L_2 M^6 R_L^2 \omega_0^4 - L_1 M^8 R_L^2 \omega_0^4 \\[4pt]
b = -L_1^5 R_L^6 \omega_0^2 + 3L_1^5 L_2^2 R_L^4 \omega_0^4 - 3L_1^4 L_2 M^2 R_L^4 \omega_0^4 - L_1^3 M^4 R_L^4 \omega_0^4 + 4L_1^3 L_2^2 M^4 R_L^2 \omega_0^6 - 4L_1^2 L_2 M^6 R_L^2 \omega_0^6 + \\[4pt]
\qquad L_1 L_2^2 M^8 \omega_0^8 - L_2 M^{10} \omega_0^8 \\[4pt]
c = L_1^5 R_L^6 \omega_0^4 - 3L_1^5 L_2^2 R l^4 \omega_0^6 + L_1^4 L_2 M^2 R_L^4 \omega_0^6 + 2L_1^3 M^4 R_L^4 \omega_0^6 - 5L_1^3 L_2^2 M^4 R_L^2 \omega_0^8 + 2L_1^2 L_2 M^6 R_L^2 \omega_0^8 + \\[4pt]
\qquad L_1 M^8 R_L^2 \omega_0^8 - 2L_1 L_2^2 M^8 \omega_0^{10} + L_2 M^1 0 \omega_0^{10} \\[4pt]
d = L_1^5 L_2^2 R_L^4 \omega_0^8 + 2L_1^3 L_2^2 M^4 R_L^2 \omega_0^{10} + L_1 L_2^2 M^8 \omega_0^{12}
\end{cases}
\tag{4.81}
$$

The methodology is thus the same than the one detailed for the SS topology. The discriminant using Cardan's formulas is given, after simplification in (4.82).

$$
\begin{aligned}
\Delta = {} & 64 L_1^4 L_2^6 (-L_1 L_2 + M^2)^2 R_L^2 \omega_0^{50} (L_1^2 R_L^2 + M^4 \omega_0^2)^{15} (L_1^3 R_L^4 + L_1 M^2(-L_1 L_2 + 2M^2) R_L^2 \omega_0^2 + L_2 M^6 \omega_0^4)^4 \\[4pt]
& [L_1^6 R_L^8 - 2L_1^4 (L_1 L_2 - M^2)(2L_1 L_2 + M^2) R_L^6 \omega_0^2 + L_1^2 M^2 (4L_1^3 L_2^3 - 9L_1^2 L_2^2 M^2 + 4L_1 L_2 M^4 + M^6) R_L^4 \omega_0^4 + \\[4pt]
& 2L_1 L_2 M^6 (-L_1 L_2 + M^2)^2 R_L^2 \omega_0^6 + L_2^2 M^8 (-L_1 L_2 + M^2)^2 \omega_0^8]^2
\end{aligned}
$$

$$\tag{4.82}$$

A sign analysis of (4.82) reveals that this discriminant can not be negative. Thus, it has three real roots when it is strictly positive and one root when it is zero. This condition is given in (4.83).

$$
\Delta = 0 \Leftrightarrow
\begin{cases}
M = \sqrt{L_1 L_2} \\[6pt]
0 = L_1^3 R_L^4 + L_1 M^2(-L_1 L_2 + 2M^2) R_L^2 \omega_0^2 + L_2 M^6 \omega_0^4 \\[6pt]
0 = L_1^6 R_L^8 - 2L_1^4 (L_1 L_2 - M^2)(2L_1 L_2 + M^2) R_L^6 \omega_0^2 + L_1^2 M^2 (4L_1^3 L_2^3 - 9L_1^2 L_2^2 M^2 + 4L_1 L_2 M^4 + M^6) R_L^4 \omega_0^4 + \\[4pt]
\qquad 2L_1 L_2 M^6 (-L_1 L_2 + M^2)^2 R_L^2 \omega_0^6 + L_2^2 M^8 (-L_1 L_2 + M^2)^2 \omega_0^8
\end{cases}
$$

$$\tag{4.83}$$

The conditions of bifurcation for this topology, expressed in (4.83) are quite complex to describe but do not suffer of lack of generality. In [70], a simplification has been made to simplify these conditions. It is restricted to $1 < Q_1 < 10$ and $1 < Q_2 < 10$. It leads to (4.84).

$$Q_1 > Q_2 \tag{4.84}$$

Development for SP topology

For the SP topology, the imaginary part of the equivalent impedance of the transformer $\underline{Z_t}$ is given in (4.85).

$$\operatorname{Im}(\underline{Z_t}) = \frac{1}{\cdots}[(L_1 L_2 R_L^2 - M^2 R_L^2)\omega^6 + (-3L_1 L_2 R_L^2 \omega_0^2 + 2M^2 R_L^2 \omega_0^2 + L_1 L_2^3 \omega_0^4 - L_2^2 M^2 \omega_0^4)\omega^4 +$$
$$(3L_1 L_2 Rl^2 \omega_0^4 - 2M^2 Rl^2 \omega_0^4 - L_1 L_2^3 \omega_0^6 + L_2^2 M^2 \omega_0^6)\omega^2 + R_L^2 \omega_0^6 (M^2 - L_1 L_2)] \tag{4.85}$$

One can see that the numerator of (4.85) is a polynomial of degree six but it can be rewritten as a polynomial of degree three ($\omega^2 \to \omega$). Its discriminant is given in (4.86).

$$\Delta = 64(-L_1 L_2 + M^2)^2 R_L^4 \omega_0^{30}((-4L_1 L_2 + 3M^2)R_L^2 + L_2^2(L_1 L_2 - M^2)\omega_0^2)^2(L_1 L_2^3 \omega_0^2 - M^2(R_L^2 + L_2^2 \omega_0^2))^6 \tag{4.86}$$

Like the PS topology, an analysis of the sign of (4.86) reveals that this function can be positive (bifurcation criteria, (4.87)) or zero (bifurcation-free criteria).

$$\Delta = 0 \Leftrightarrow \begin{cases} M = \sqrt{L_1 L_2} \\ 0 = L_1 L_2^3 \omega_0^2 - M^2(R_L^2 + L_2^2 \omega_0^2) \\ 0 = (-4L_1 L_2 + 3M^2)R_L^2 + L_2^2(L_1 L_2 - M^2)\omega_0^2 \end{cases} \tag{4.87}$$

Restricted to $1 < Q_1 < 10$ and $1 < Q_2 < 10$, the following condition has been established for this topology in [69].

$$Q_1 > Q_2 + \frac{1}{Q_2} \tag{4.88}$$

Development for PP topology

For the PS topology, the imaginary part of the equivalent impedance of the transformer $\underline{Z_t}$ is given in (4.89).

$$\text{Im}(\underline{Z_t}) = \frac{a\omega^7 + b\omega^5 + c\omega^3 + d\omega}{\dots} \tag{4.89}$$

One can see that the numerator of (4.89) is a polynomial of degree seven but it can be rewritten as a polynomial of degree three, as suggested in (4.90).

$$aX^3 + bX^2 + cX + d = 0 \tag{4.90}$$

$$
\begin{cases}
a = L_1^3 L_2^5 M^4 R_L^4 - 3L_1^2 L_2^4 M^6 R_L^4 + 3L_1 L_2^3 M^8 R_L^4 - L_2^2 M^1 0 R_L^4 + L_1^5 L_2^9 R_L^2 \omega_0^2 - 5L_1^4 L_2^8 M^2 R_L^2 \omega_0^2 + \\
\qquad 10 L_1^3 L_2^7 M^4 R_L^2 \omega_0^2 - 10 L_1^2 L_2^6 M^6 R_L^2 \omega_0^2 + 5L_1 L_2^5 M^8 R_L^2 \omega_0^2 - L_2^4 M^1 0 R_L^2 \omega_0^2 \\[4pt]
b = -L_1 L_2 M^8 R_L^6 + M^1 0 R_L^6 - 4L_1^3 L_2^5 M^4 R_L^4 \omega_0^2 + 10 L_1^2 L_2^4 M^6 R_L^4 \omega_0^2 - 8L_1 L_2^3 M^8 R_L^4 \omega_0^2 + \\
\qquad 2L_2^2 M^1 0 R_L^4 \omega_0^2 - 3L_1^5 L_2^9 R_L^2 \omega_0^4 + 13 L_1^4 L_2^8 M^2 R_L^2 \omega_0^4 - 21 L_1^3 L_2^7 M^4 R_L^2 \omega_0^4 + \\
\qquad 15 L_1^2 L_2^6 M^6 R_L^2 \omega_0^4 - 4L_1 L_2^5 M^8 R_L^2 \omega_0^4 + L_1^5 L_2^1 1 \omega_0^6 - 5L_1^4 L_2^{10} M^2 \omega_0^6 + \\
\qquad 10 L_1^3 L_2^9 M^4 \omega_0^6 - 10 L_1^2 L_2^8 M^6 \omega_0^6 + 5L_1 L_2^7 M^8 \omega_0^6 - L_2^6 M^{10} \omega_0^6 \\[4pt]
c = 2L_1 L_2 M^8 R_L^6 \omega_0^2 - M^1 0 R_L^6 \omega_0^2 + 5L_1^3 L_2^5 M^4 R_L^4 \omega_0^4 - \\
\qquad 11 L_1^2 L_2^4 M^6 R_L^4 \omega_0^4 + 7L_1 L_2^3 M^8 R_L^4 \omega_0^4 - L_2^2 M^{10} R_L^4 \omega_0^4 + 3L_1^5 L_2^9 R_L^2 \omega_0^6 - \\
\qquad 12 L_1^4 L_2^8 M^2 R_L^2 \omega_0^6 + 17 L_1^3 L_2^7 M^4 R_L^2 \omega_0^6 - 9L_1^2 L_2^6 M^6 R_L^2 \omega_0^6 + L_2^4 M^{10} R_L^2 \omega_0^6 - \\
\qquad L_1^5 L_2^1 1 \omega_0^8 + 5L_1^4 L_2^{10} M^2 \omega_0^8 - 10 L_1^3 L_2^9 M^4 \omega_0^8 + 10 L_1^2 L_2^8 M^6 \omega_0^8 - \\
\qquad 5L_1 L_2^7 M^8 \omega_0^8 + L_2^6 M^1 0 \omega_0^8 \\[4pt]
d = -L_1 L_2 M^8 R_L^6 \omega_0^4 - 2L_1^3 L_2^5 M^4 R_L^4 \omega_0^6 + 4L_1^2 L_2^4 < M^6 R_L^4 \omega_0^6 - 2L_1 L_2^3 M^8 R_L^4 \omega_0^6 - \\
\qquad L_1^5 L_2^9 R_L^2 \omega_0^8 + 4L_1^4 L_2^8 M^2 R_L^2 \omega_0^8 - 6L_1^3 L_2^7 M^4 R_L^2 \omega_0^8 + 4L_1^2 L_2^6 M^6 R_L^2 \omega_0^8 - L_1 L_2^5 M^8 R_L^2 \omega_0^8
\end{cases} \tag{4.91}
$$

The methodology is thus the same than the one detailed for the others topologies. The discriminant

using Cardan's formulas is given, after simplifications in (4.82).

$$\Delta = 64 L_1^3 L_2^5 (L_1 L_2 - M^2)^7 R_L^8 \omega_0^{20} \left(M^4 R_L^2 + L_2^2 (-L_1 L_2 + M^2)^2 \omega_0^2 \right)^{15} \left(M^6 R_L^4 - L_2^2 M^2 (-L_1 L_2 + M^2)^2 R_L^2 \omega_0^2 + \right.$$

$$\left. L_2^4 (L_1 L_2 - M^2)^3 \omega_0^4 \right)^4 \left(M^8 R_L^8 + 2 L_2^4 (2 L_1 L_2 - M^2)(-L_1 L_2 M + M^3)^2 R_L^4 \omega_0^4 + 4 L_1 L_2^7 (-L_1 L_2 + M^2)^3 R_L^2 \omega_0^6 + \right.$$

$$\left. L_2^8 (-L_1 L_2 + M^2)^4 \omega_0^8 \right)^2$$

$$(4.92)$$

An analysis of the sign of (4.92) reveals that this discriminant can not be negative. Thus, it has three real roots when it is strictly positive and one root when it is zero. This condition is given in (4.93).

$$\Delta = 0 \Leftrightarrow \begin{cases} M = \sqrt{L_1 L_2} \\ 0 = M^6 R_L^4 - L_2^2 M^2 (-L_1 L_2 + M^2)^2 R_L^2 \omega_0^2 + L_2^4 (L_1 L_2 - M^2)^3 \omega_0^4 \\ 0 = M^8 R_L^8 + 2 L_2^4 (2 L_1 L_2 - M^2)(-L_1 L_2 M + M^3)^2 R_L^4 \omega_0^4 + \\ \qquad 4 L_1 L_2^7 (-L_1 L_2 + M^2)^3 R_L^2 \omega_0^6 + L_2^8 (-L_1 L_2 + M^2)^4 \omega_0^8 \end{cases}$$

$$(4.93)$$

Restricted to $1 < Q_1 < 10$ and $1 < Q_2 < 10$, the following condition has been established for this topology in [70].

$$Q_1 > Q_2 + \frac{1}{Q_2} \qquad\qquad (4.94)$$

4.5.2 Conclusion

The bifurcation criteria studied in this section is function of the compensation topology. General criteria have been developed for the four topologies. Unlike the results described in [70], the ones developed in this study are not dependant of any condition on the quality factors of the transformer, which restricts the domain of validity of the study.

The simplified conditions described in [70] are summarized below. The quality factors Q_1 and Q_2 of the primary and secondary coil respectively are summarized in Table 4.6 for the four compensation topologies.

As an example, a typical response of the transformer working at normal mode and bifurcation mode is illustrated in Fig. 4.11. For the normal mode, there is only one resonant frequency which corresponds to a maximum power transmitted. For the bifurcation mode, there is three resonant frequencies and two maxima regarding the power transmitted.

Table 4.6: Determination of the simplified bifurcation criteria ($1 < Q_{1,2} < 10$)

Topology	Bifurcation criterion
SS	$Q_1 < \dfrac{4Q_2^3}{4Q_2^2 - 1}$
SP, PP	$Q_1 < Q_2 + \dfrac{1}{Q_2}$
PS	$Q_1 < Q_2$
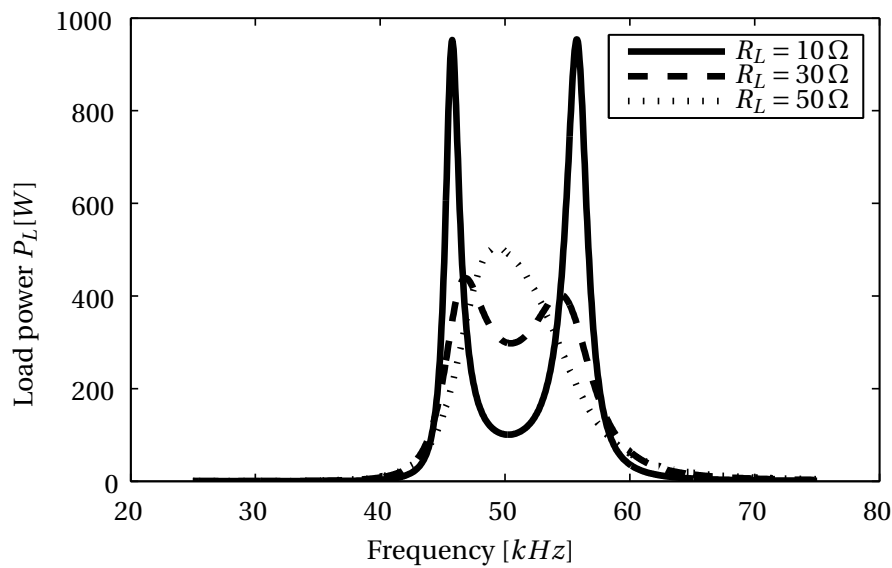
Figure 4.11: Comparison of normal mode and bifurcation operation for different load resistances

The bifurcation phenomenon could be used in order to regulate the transmitted power of the transformer acting on the frequency while keeping the supply voltage constant. However, as demonstrated in Section 3, the self and mutual inductances are function on the frequency when conductive parts are placed in the proximity of the transformer. The frequency is often kept constant and the supply voltage is adapted to control the transmitted power in this case.

Moreover, the bifurcation phenomenon depends on the coupling factor of the transformer, as illustrated in Fig. 4.12. If the bifurcation occurs, the transmitted power can be increased. The conductors should be designed according to this possible phenomenon if the transformer works at different frequencies.
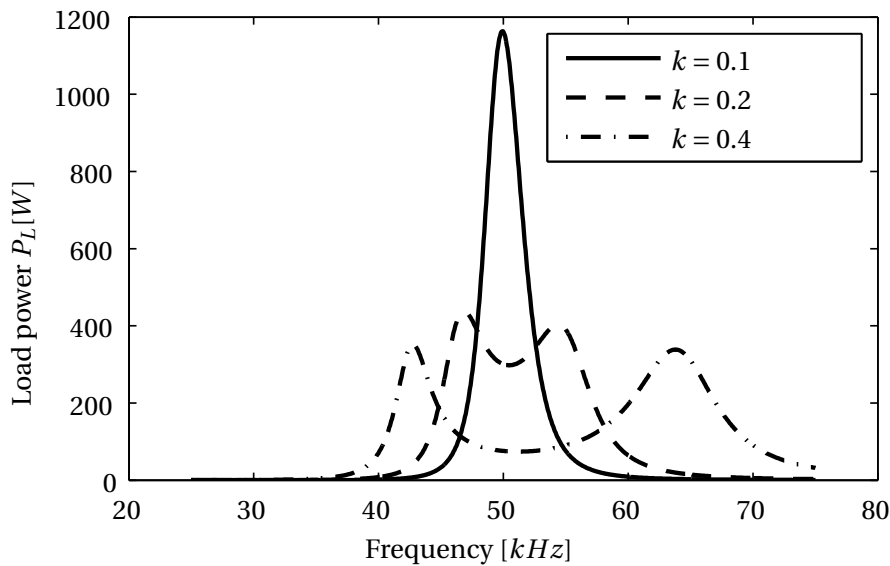
Figure 4.12: Comparison of normal mode and bifurcation operation for different coupling factors

4.6 Conclusion

This chapter presents and performs an analysis of four capacitive compensation topologies of the transformer. It shows that the transmitted power and the efficiency of the transformer can be widely improved using compensation capacitances at both primary and secondary side if a proper design is made. Indeed, using a compensation capacitance at the secondary side aims to increase the efficiency of the transformer because the current in the coils is decreased for a given load power. The total equivalent reactance of the transformer can be cancelled if a capacitance is inserted in the primary part of the transformer. In literature, the resistances are generally neglected to compute the value of the capacitances. A general development is made in this work including these resistances because their impact can generally not be neglected when the transformer is used in presence of conductive parts.

Moreover, the determination of the two compensation capacitances leads to two degrees of freedom in this system. This means that two conditions can be met. The compensation methodology used in the literature, called the "efficiency-oriented compensation" aims to maximize the efficiency and cancel the equivalent reactance of the transformer. However, depending on the compensation topology, the value of the compensation capacitances depends on the load value which is very often variable. For this purpose, a novel compensation methodology called "control-oriented compensation" is proposed. The aim is to cancel the reactance of the transformer and to get the value of the capacitances independently of the load value. Although the efficiency is not maximimal, a high value is still required.

The load characteristic of the transformer working at the resonant frequency is studied in this chapter. It is shown that the behaviour of the transformer regarding load variations depends on the compensation topology and on the type of the power supply. The computation of the load characteristics is made for the four topologies and for the three different type of power supplies (constant input voltage, constant input current and constant current in the primary coil).

A frequency response analysis of the transformer is also performed in this chapter. This modelling

is very important to predict the behaviour of the transformer when the frequency changes and/or when the transformer is detuned. Depending on the parameter values such as the inductances and the load resistance, the frequency response changes and three resonant frequencies appears. It is called the bifurcation phenomenon. In literature, an approximation of the bifurcation criteria has been performed but the domain of validity of the results is restricted to high power transfer. In this chapter, general bifurcation criteria are developed. Especially when the transformer is detuned or when the operating frequency is variable, the bifurcation criteria should be carefully studied because it can bring the transformer into an over power state.

Finally, a list of criteria in order to choose the compensation topology can be drawn up :

- The topology can be chosen if a special load characteristics is required by the specifications.

- A parallel compensation should be adopted if the specifications require a maximum voltage across the coils (the voltage across the primary/secondary coil equals the supply/load voltage whereas a larger voltage is generated for serial compensation.

- The current flowing in the primary/secondary coil equals the supply/load current using a serial compensation, whereas it is larger for a parallel compensation. This should be taken into account during the choice of the compensation.

- A parallel compensation leads to an additional choke inductance (its function is detailed in Section 3). This increases costs, especially for high power applications.

Innovative contribution to the chapter
The different capacitive compensation topologies are studied in detail in this chapter. A novel compensation methodology which aims to simplify the control of the transformer is proposed and compared to the existing one. Using this compensation methodology, the primary compensation capacitance is load-independent. The load characteristics are also developed for the different topologies. This concept is not so discussed in literature but can be a very important point in order to avoid an additional power converter at the output of the transformer. Then, the frequency response and the associated bifurcation phenomenon is studied. The bifurcation criteria are investigated in literature but are limited to a reduced range of quality factors. In this study, a general approach is used and general criteria for the different compensation topologies are developed.

Relative publications to the chapter

- D. Ladas, Y. Perriard, C. Auvigne and P. Germano, Energy conversion system, July 2 2014, EP Patent App. EP20,130,181,857

- C. Auvigne, P. Germano, D. Ladas, Y. Perriard, "About tuning capacitance in inductive coupled power transfer", Power Electronics and Applications (EPE 2013), Proceedings of the 2011-15th European Conference on, September 2013

- C. Auvigne, P. Germano, D. Ladas, Y. Perriard, "A dual-topology ICPT applied to an electric vehicle battery charger", Electrical Machines 2012, XXth International Conference On, sept. 2012

5 Shielding of the transformer

Contents

5.1   Introduction

As studied in Chapter 3, Joule losses are induced in any conductive plate in presence of an alternative magnetic field. Therefore, if the transformer is made of two coils in the air, its efficiency is very low if a conductive plate is placed close to the transformer. The inductance values changes and the transformer is detuned. In this case, the performances decrease, as studied in Chapter 4. Moreover, the Joule losses induced in the conductive plate(s) generate heating which can bring theses parts to very high temperatures.

Unfortunately, conductive parts are present in the proximity of the transformer in most applications. For electric vehicles inductive charging systems, the secondary coil is situated just under the iron chassis. For desktop peripherals or smartphone contactless chargers, the print circuit board has a ground plate which is a copper plate. Therefore, an efficient shielding is necessary to highly reduce the magnetic field in the conductive parts.

Another advantage in using a shielding is to reduce the radiated magnetic field at proximity of the transformer. This is a crucial point to fulfil the the ICNIRP rules, especially for high power applications [29].

In this chapter, several principles of shielding are investigated. The first one consists in inserting some ferromagnetic parts in order to guide the magnetic field. Ferrite bars are generally used for this purpose because the relative permeability μ_r is high compared to other materials (about 2000), and the electric resistivity is very high (typically $3\,\Omega\,\mathrm{m}$). The advantage of these specifications is that only few Eddy currents flow in these materials. However, the magnetic saturation is quite low (typically around $0.4\,\mathrm{T}$) compared to iron parts. If the magnetic flux density is higher in these regions, the ferrite does not guide the magnetic flux any more. The second principle consists in inserting some conductive parts using a material where the depth penetration is high, such as aluminium or copper. The main advantage of this technique is that most of the magnetic field is cancelled by the conductive parts if its thickness is higher than the depth penetration. Another advantage compared to the ferromagnetic parts is that there is no saturation effect in these conductive parts. However, this shielding technique is based on Eddy currents which generate Joule losses due to the resistivity of the material, as studied in Chapter 3. The system efficiency is decreased and these losses can bring the conductive parts to high temperatures, depending of the configuration. In this chapter, ferromagnetic and conductive parts are combined to realise the shielding. One implementation has been proposed in [9]. In this work, several scenarios are investigated and compared.

5.2   Description of the study

In order to study the performances of different shielding topologies, several scenarios are investigated. The geometry of the system is presented in Fig. 5.1. Two criteria of performances are investigated. The first one is the efficiency of the transformer. This means that the losses induced in the iron plate and the shielding are to be minimised. The second criterion is the radiated magnetic field outside the transformer. It is also to be minimised.

The geometry of the system is axis-symmetric. It is composed of two circular coils. An iron plate which represents the environment (the vehicle chassis for example) is placed above the secondary coil. The distance between the iron plate and the secondary power pad is supposed to be imposed by the specifications. Otherwise, it is obvious that the longer the distance is, the smaller the losses are. A first
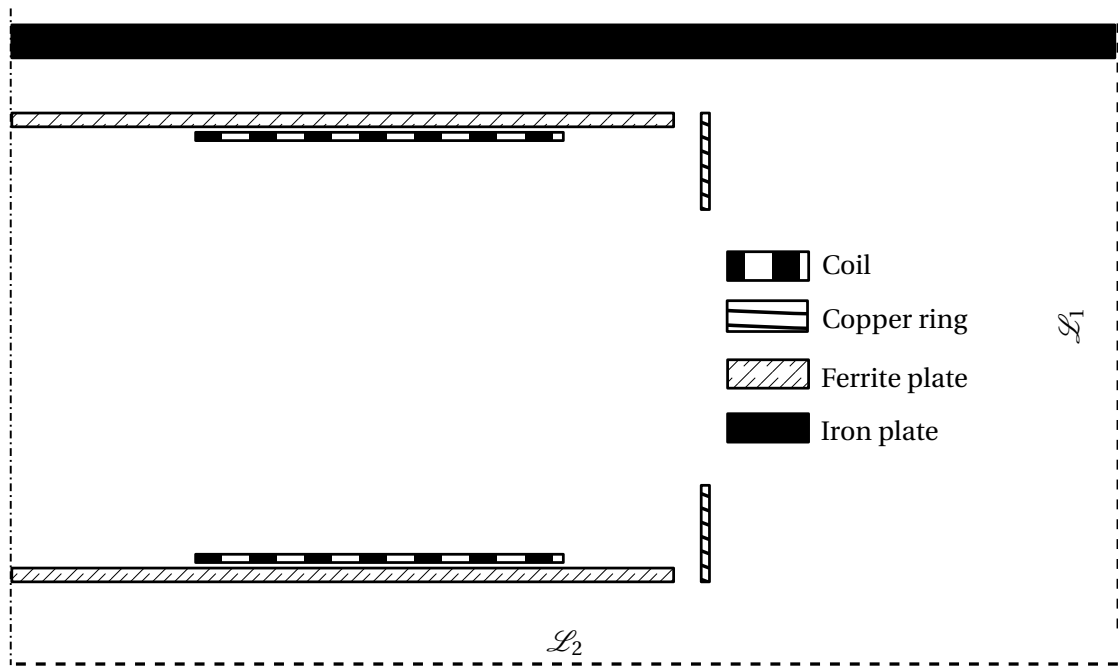
Figure 5.1: Geometry of the shielding (cross-section)

part of the shielding is composed of two ferrite plates placed under the two coils. The aim of these parts is to focus the magnetic field near the coils and to limit the flux in the iron plate. The second part of the shielding is made of two copper rings. The aim of these parts is to decrease the radiated magnetic field outside of the transformer.

In the scope of this study, it is assumed that the primary and the secondary parts are aligned to the symmetry axis. In order to highlight the effect of each part, different scenarios are studied and are presented in Fig. 5.2.

For all the investigated scenarios, the iron plate is present because it is a part of the environment of the transformer.

- Scenario sc_1 : No shielding is used in this scenario. The transformer is only made of the primary and secondary coil. The aim of this scenario is to study the performances of the transformer without any shielding.

- Scenario sc_2 : Compared to the previous scenario, two ferrite plates (one at the primary side and the other at the secondary side) are used. The aim of this shielding is to increase the magnetic coupling between the two coils and to reduce the magnetic field into the iron plate in order to increase the efficiency.

- Scenario sc_3 : As the previous scenario, two ferrite plates are used. In this scenario, a copper ring is inserted at the primary side of the transformer. The aim of this part is to decrease the radiated magnetic field.

- Scenario sc_4 : In this scenario, the two ferrite plates are used and a copper ring is introduced at the secondary side of the transformer. The aim of this part is to decrease the radiated magnetic

(a) Scenario sc_1

(b) Scenario sc_2

(c) Scenario sc_3

(d) Scenario sc_4
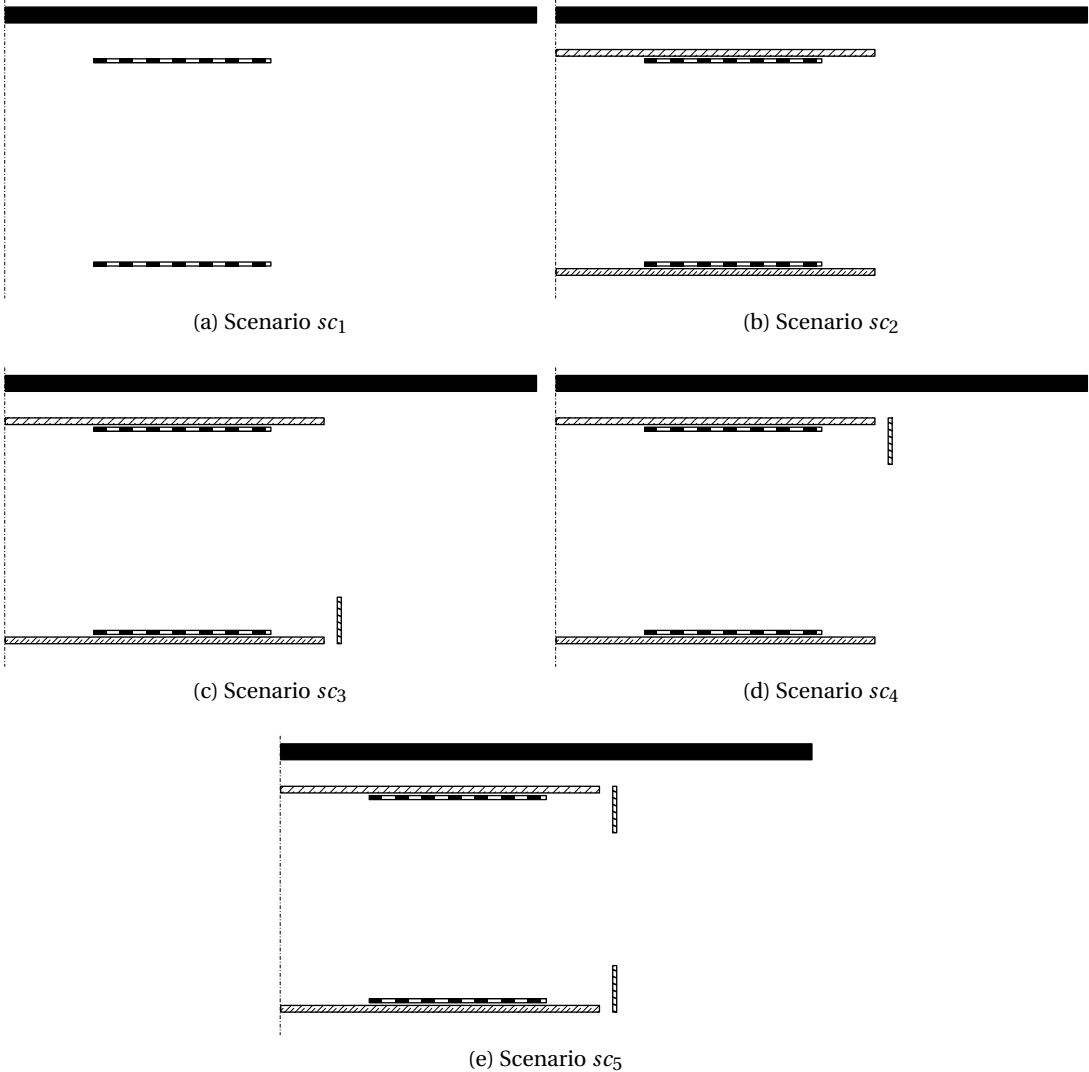
(e) Scenario sc_5

Figure 5.2: Description of the scenarios investigated

field and to reduce the magnetic flux in the iron plate.

- Scenario sc_5 : In this scenario, the two ferrite plates are used and the two copper rings are inserted. The aim of this scenario is to combine the advantage of each part of the shielding.

The geometric parameters of the transformer set for this study are summarized in Table 5.1.

Table 5.1: Geometrical parameters chosen for this study

Parameter	Value
External radius of the primary coil	250 mm
External radius of the secondary coil	250 mm
Internal radius of the primary coil	83 mm
Internal radius of the secondary coil	83 mm
radius of the primary ferrite	350 mm
radius of the secondary ferrite	350 mm
Distance between the pads	150 mm
Distance between the ferrite and the plate	20 mm
Position of the primary ring (x-axis)	400 mm
Position of the secondary ring (x-axis)	400 mm

For each scenario listed above, the different quantities of the system are computed using 2D finite element method, assuming that the system is linear. This means that no saturation is present in the ferrite plates and the non-linear behaviour of the hysteresis effect in the ferrite is neglected.

This study is divided into three parts. The first one, called preliminary study, consists in applying a voltage across the primary coil and in computing the different elements of interest of the transformer modelled in Chapter 3. The number of the coil turns is fixed. The second one consists in choosing the number of turns of each scenario to transfer an imposed load power. The last one consists in performing an optimisation on the shielding geometries.

5.3 Preliminary study

For this study, the primary voltage is set to 300 V and the operating frequency is set to 50 kHz. The turn numbers for both primary and secondary coil is set to 15 turns. For the five investigated scenarios, the equivalent resistances, inductances and the magnetic coupling factor are computed. The results of the simulations undertaken are presented in Table 5.2. The isolines are presented in Fig. 5.3 without and with the copper rings.

Several relevant conclusions can be drawn from these results.

- As studied in Chapter 3, the value of the resistances R_1 and R_2 reflects the Joule losses in the transformer. It means that for a given mutual inductance M, the smaller these resistances are, the better the efficiency is. Since the number of turns is the same for all the scenarios, the mutual inductance depends on the scenario. However, without any shielding (scenario sc_1), the resistance R_2 is very large compared to the other scenarios (about 10 to 100 times larger). The mutual inductance is also lower, leading to a very low efficiency.

- The complete shielding (scenario sc_5) leads to the smallest values of the resistances.

(a) Scenario sc_2 (b) Scenario sc_5
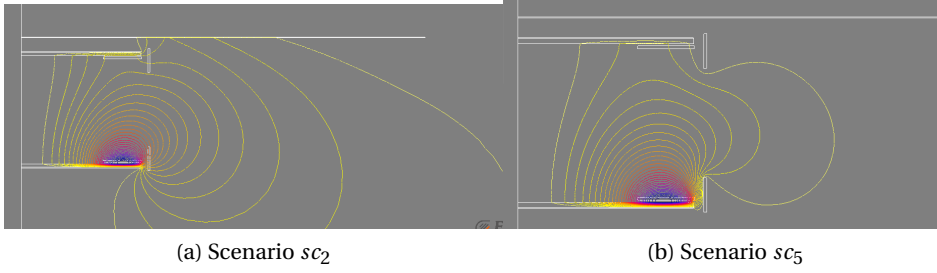
Figure 5.3: Repartition of the magnetic field

Table 5.2: Results for the preliminary study

	sc_1	sc_2	sc_3	sc_4	sc_5
$R_1[m\Omega]$	164.22	126.95	61.97	28.74	20.49
$R_2[m\Omega]$	1939.81	149.17	90.43	28.70	21.85
$L_1[\mu H]$	32.66	67.16	63.44	64.53	61.94
$L_2[\mu H]$	25.70	66.99	64.08	63.68	61.93
$M[\mu H]$	5.52	25.96	20.40	20.74	16.63
k	0.19	0.39	0.32	0.32	0.27

- Although the aim of the rings is to reduce the leakage flux, the best magnetic coupling factor is obtained for the scenario sc_4 (without the primary ring).

- Adding the ring at the primary side reduces the resistances, but this effect is more pronounced at the secondary side. Adding a ring at both sides leads to the smallest values of resistance but the coupling factor decreases. More investigations are necessary to determine the advantage of two rings on the efficiency of the transformer.

5.4 Study according to the electrical specifications

The preliminary study presented above compares the five scenarios for a given geometry, number of turns and primary voltage. It means that the load power and the load voltage depends on the scenario. Mostly, specifications let free the geometry but the electrical specifications are imposed. This study is now undertaken according to the specifications given in Table 5.3.

To fulfil these specifications, the design of the transformer is split into two parts. It consists in separating the electrical design using the electric equivalent circuit presented in Chapter 3 and the magnetic design.

The first step of the electrical design is to choose a compensation topology. The SS topology is used for this study. According to Section 4.4, assuming that the transformer is working at its resonant frequency, the mutual inductance is imposed by the supply voltage, the load power and the load voltage, as suggested in (4.28). One can see that the value of the self inductances L_1 and L_2 does not change the

Table 5.3: Electrical parameters chosen for this study

Parameter	Value
Load voltage	$U_L = 300\,\text{V}$
Supply voltage (AC)	$U_{in} = 350\,\text{V}$
Operating frequency	$f_0 = 50000\,\text{Hz}$
Load power	$P_L = 6\,\text{kW}$

load power and voltage by using this compensation topology.

In this study, the geometry is unchanged, except the number of turns of the coils. An infinity of combinations exists to obtain the desired mutual inductance M. To simplify the understanding of the system and the design, the number of turns is the same at both primary and secondary sides ($N = N_1 = N_2$). The solution is now unique (only one N gives the desired mutual inductance). The different parameters of the transformers are given in Table 5.4. The electric characteristics of the transformer for each scenario, such as the efficiency η, the load voltage U_L and the load power P_L are presented in Table 5.5.

Table 5.4: Parameter of the transformers with M imposed

	sc_1	sc_2	sc_3	sc_4	sc_5
N_1, N_2	34	16	18	18	20
$R_1\,[m\Omega]$	1877	309	190	86	75
$R_2\,[m\Omega]$	22290	363	279	85	80
$L_1\,[\mu H]$	375	164	197	197	236
$L_2\,[\mu H]$	295	164	199	195	236
$M\,[\mu H]$	63.50	63.57	63.58	63.57	63.59
k	0.19	0.39	0.32	0.32	0.27

Some relevant conclusions can be made out from the results presented in Table 5.5 :

- As expected from the results shown in Table 5.2, the efficiency obtained without shielding is very low.

- Due to the large value of the resistances, the transmitted power is lower than the specifications. The simplified formulas described in (4.28) are no more valid; the general formula developed in (4.27) should be used in this case in order to obtain more accurate results.

- The transmitted power P_L is coherent with the specifications (the maximal difference is 2%)

Table 5.5: Results obtained with M imposed

	sc_1	sc_2	sc_3	sc_4	sc_5
η	0.34	0.96	0.97	0.98	0.98
U_L[V]	253	296	297	298	298
P_L[W]	4276	5852	5900	5949	5946
$ERR\,U_L$[%]	15.57	1.24	0.83	0.42	0.45
$ERR\,P_L$[%]	28.72	2.46	1.66	0.84	0.90

for the different shielded configurations. The smaller the resistances R_1 and R_2 are, the more accurate the load power is.

- Although the magnetic coupling factor k is maximal for the scenario sc_2, the best efficiency is obtained for the scenarios sc_4 and sc_5. For the geometry used in this study, the secondary ring is very important to reduce the emission in the iron plate.

The amplitude of the magnetic flux density on the lines $\mathscr{L}_1$ and $\mathscr{L}_2$ is plotted for the five scenarios investigated in Fig. 5.4.

Some relevant conclusions can be made from Fig. 5.4.

- As expected, the emission along $\mathscr{L}_1$ is maximum for the scenario sc_2. The rings decrease the emission by a factor 7. Using this geometry, the ring at the primary side is very important to minimize the emission (the emission increases by a factor 3 without this primary ring) according to Fig. 5.4a.

- As expected, the emission along $\mathscr{L}_2$ is maximum for the scenario sc_1 since no ferrite plates focus the magnetic flux density. With this geometry, the primary ring reduces the emission by a factor 3. As expected, the secondary one is not useful to reduce the field along $\mathscr{L}_2$.

- The emission on $\mathscr{L}_2$ is bigger than the one on $\mathscr{L}_1$. To reduce it, a simple solution consists in inserting a conductive plate (e.g an aluminium plate) under the ferrite.

5.5   Optimisation of the shielding

In the previous section, the impact of the shielding topology regarding the performances of the transformer is investigated. However, the geometry if fixed. The aim of this section is to optimise the performances of the transformer dealing with the shielding geometry and the operating frequency. As enunciated before, the results are computed using FEM. Therefore, a numerical algorithm of optimisation must be used. A description of optimisation problem definitions and algorithms is presented in Appendix A. In this section, an implementation of the Genetic algorithms (GA) is used.
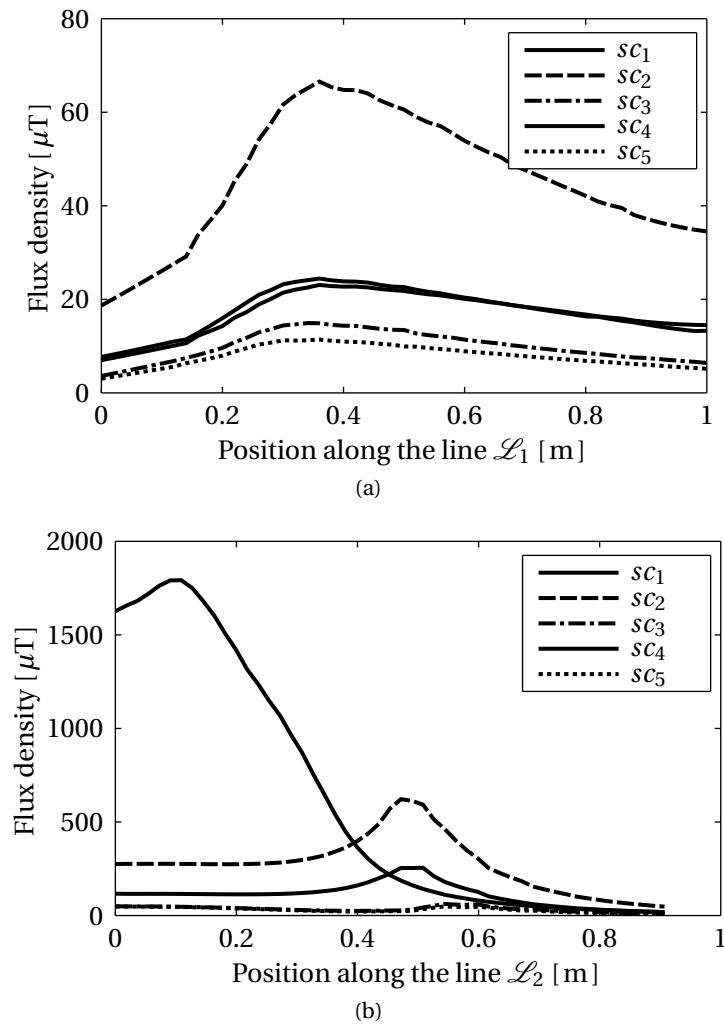
Figure 5.4: Study of the magnetic field emission

5.5.1 Description of the optimisation

In the scope of this optimisation, the input and electrical characteristics are imposed. The specifications are listed in Table 5.6. The operating frequency is let free.

Table 5.6: Electrical specifications

Parameter	Value
Supply voltage (RMS)	$U_{in} = 360\,\text{V}$
Load voltage (RMS)	$U_L = 270\,\text{V}$
Load power	$P_L = 6000\,\text{W}$

As for the previous studies, the compensation topology used for this study is the SS one. It is assumed

that the transformer is fully compensated as developed in Section 4.4.1, working at its main resonant frequency and that the resistance of the coils is negligible. Thus, the gain $\frac{I_L}{U_{in}}$ of the transformer is given by the mutual inductance M and the pulsation ω_0.

The geometrical parameters to be optimised are listed in Table 5.8 and illustrated in Fig. 5.5. The fixed parameters which generally come from the specifications are listed in Table 5.7.
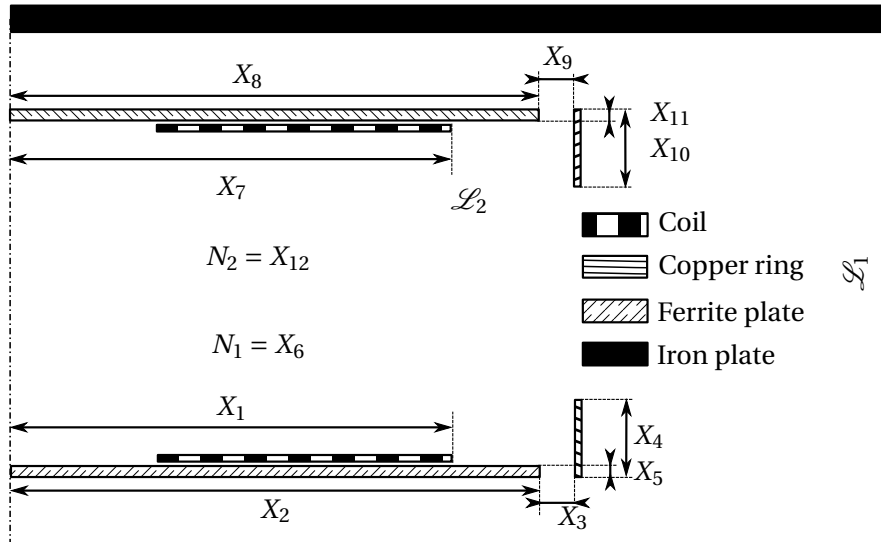
Figure 5.5: Description of the parameters to be optimised

Table 5.7: Fixed parameters for the optimisation process

Parameter	Value
Distance between the pads	150 mm
Distance between the ferrite and the plate	20 mm
Radius of the iron plate	600 mm
Internal radius of the coils	computed
Thickness of the coils	computed
Current density in the coils	$3\,\text{A}\cdot\text{mm}^{-2}$
Fill factor of the coils	0.4

The internal radius of the coils and its thickness are computed to obtain a desired current density. The coil made of one or more identical layer(s). If it is possible, the coil is made of one layer. If the number of turns is too high, an additional layer is added to the first one. The methodology to compute the number of layers for both the primary and secondary side is explained below.

- The surface of the coil, depending on the current I_1, the turn numbers N_1 and the fill factor of the coil ff, is computed to obtain the current density according to (5.1).

- The number of layer(s) needed is computed according to (5.2).

Table 5.8: Optimisation parameters

Parameter	Primary	Secondary	Range
External radius of the coil	X_1	X_7	$[150, 250]$ mm
Radius of the ferrite	X_2	X_8	$[150, 350]$ mm
Position of the ring (x-axis)	X_3	X_9	$[5, 50]$ mm
Position of the ring (y-axis)	X_5	X_{11}	$[-20, 20]$ mm
Ring height	X_5	X_{11}	$[10, 35]$ mm

• The internal radius of the coil is (are) computed.

If the transformer is symmetric (i.e the primary and secondary are the same), the surface of the conductors are determined with the largest current flowing in the transformer.

$$S_{needed} = \frac{I_1 N_1}{J_{max} ff} \tag{5.1}$$

$$N_{layer} = \text{Floor}(\frac{S_{needed}}{S_{layer}}) + 1 \tag{5.2}$$

The optimisation is done for the scenarios sc_2 to sc_5 presented in the study of the shielding. For each scenario, the frequency is set to 30 kHz, 50 kHz, 90 kHz and 150 kHz.

The objective functions of these optimisations are the power losses P_{loss} and the maximum radiated flux density along the line $\mathscr{L}_1$ B_{max}. The two objective functions are to be minimised. As studied in the previous section, the mutual inductance value of the transformer gives the load values. In this optimisation, it is defined as a constraint on the optimisation, as suggested in (5.3).

$$C_1 = \begin{cases} 0 \text{ if } \dfrac{|M_{targ} - M_{mes}|}{M_{targ}} \leqslant 0.1 \\ 100 \text{ if } \dfrac{|M_{targ} - M_{mes}|}{M_{targ}} > 0.1 \end{cases} \tag{5.3}$$

5.5.2 Results of the optimisations

The Pareto fronts for the optimisations classified by scenarios are shown in Fig. 5.6.

One can see that for the four scenarios investigated, a higher frequency leads to a smaller radiated field.

(a) Scenario sc_2

(b) Scenario sc_3

(c) Scenario sc_4
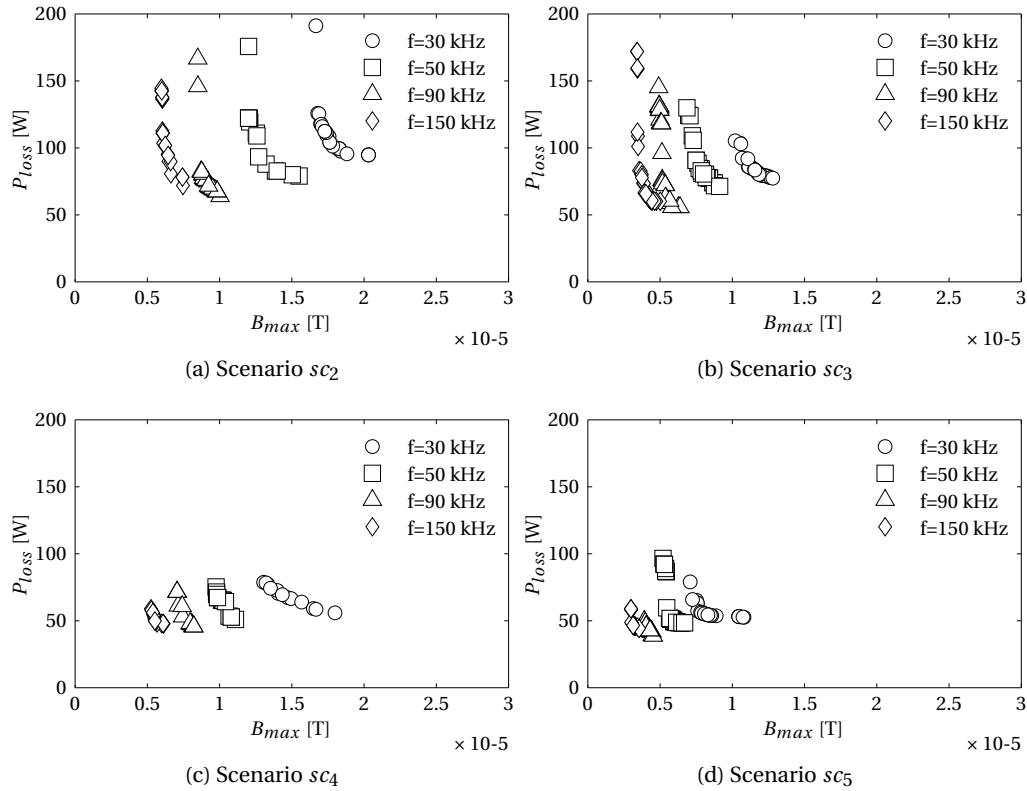
(d) Scenario sc_5

Figure 5.6: The Pareto fronts sorted by scenarios

This results is expected because increasing the frequency leads to a smaller target mutual inductance M_{targ}. Indeed, the self inductances are smaller and the magnetic flux necessary to transmit the required power is smaller. Moreover, one can note that the losses are always smaller at 50 kHz than 30 kHz and smaller at 90 kHz than 50 kHz. However, increasing the operating frequency at 150 kHz does not reduce the power losses. In fact, although the mutual inductance decreases when the frequency increases, the losses induced by Eddy currents in the conductive parts increase.

Finally, one can see that the maximum power losses of the Pareto front for the scenarios sc_4 and sc_5 is smaller (about 100 W) than the losses for the scenarios sc_2 and sc_3 (about 200 W). This means that the presence of the ring at the secondary side reduces the sensitivity of the other parameters regarding the power losses.

The Pareto fronts for the optimisations classified by frequencies are shown in Fig. 5.7.

One can note that for all the frequencies studied, the presence of the ring(s) reduce the radiated magnetic field and the power losses. Moreover, for each frequency, the scenario which leads to the best results is the scenario sc_5 (rings at both primary and secondary side). The presence of the ring at the primary side (scenario sc_2) aims to reduce the magnetic field while the losses are smaller with a ring at the secondary side (scenario sc_3). This observation is intuitive since the ring at the secondary side reduces the magnetic field in the iron plate, and thus the losses induced by Eddy currents.

For each frequency studied, an optimal solution is drawn in Fig. 5.8 for the scenario sc_4. Similar
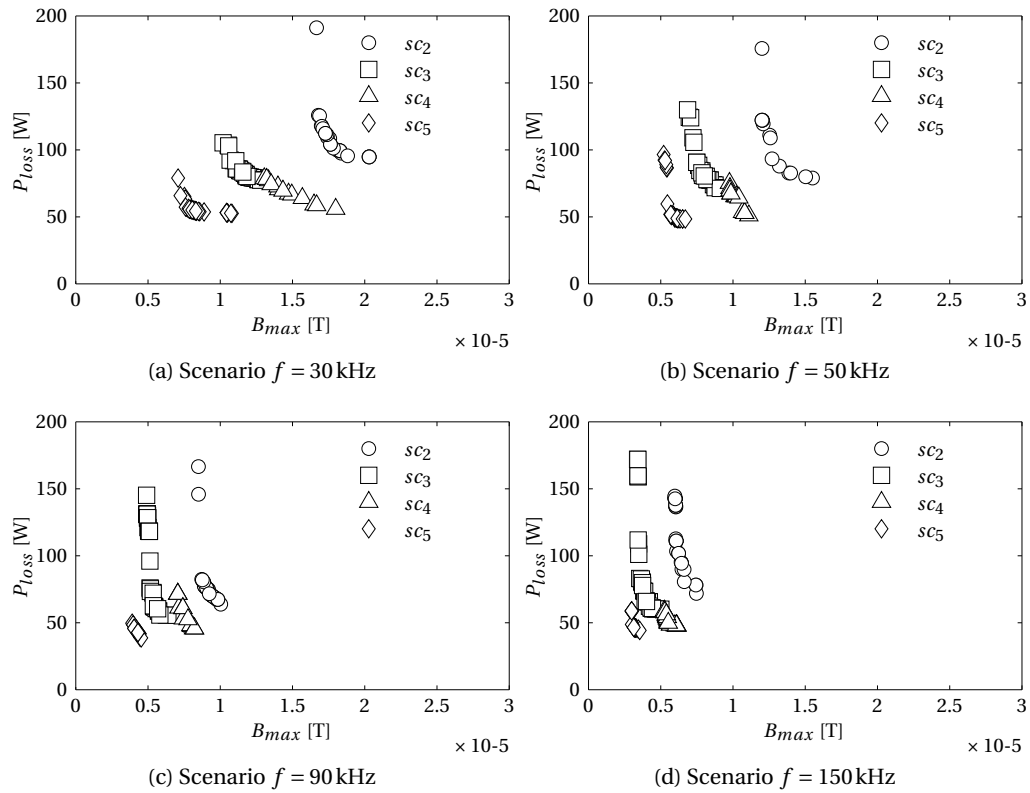
Figure 5.7: The Pareto fronts sorted by frequency

results can be found for the other scenarios. Its corresponding parameters are reported in and its corresponding results are detailed in Table 5.10. One can see that about 40% of the total losses are due to the hysteresis losses in the ferrite plates. Another 40% comes from the coils. The other 20% comes from the other parts of the shielding.

Table 5.9: Optimisation parameters

Frequency		30 kHz	50 kHz	90 kHz	150 kHz
Parameter name	Parameter				
Number of turns	$N_1 = N_2$	48	35	26	12
External radius of the coil [mm]	$X_1 = X_7$	150	150	150	150
radius of the ferrite [mm]	$X_2 = X_8$	346	340	325	322
Position of the ring (x-axis) [mm]	$X_3 = X_9$	30	50	33	39
Position of the ring (y-axis) [mm]	$X_5 = X_{11}$	18	18	17	12
Ring height[mm]	$X_5 = X_{11}$	30	26	25	16

One can see that for the four chosen optimal solutions, the external radius of the coil is the lowest value of its range. This means that reducing the radius of the coils and increasing the number of turns to

(a) Scenario sc_4, $f = 30\,\text{kHz}$

(b) Scenario sc_4, $f = 50\,\text{kHz}$

(c) Scenario sc_4, $f = 90\,\text{kHz}$

(d) Scenario sc_4, $f = 150\,\text{kHz}$
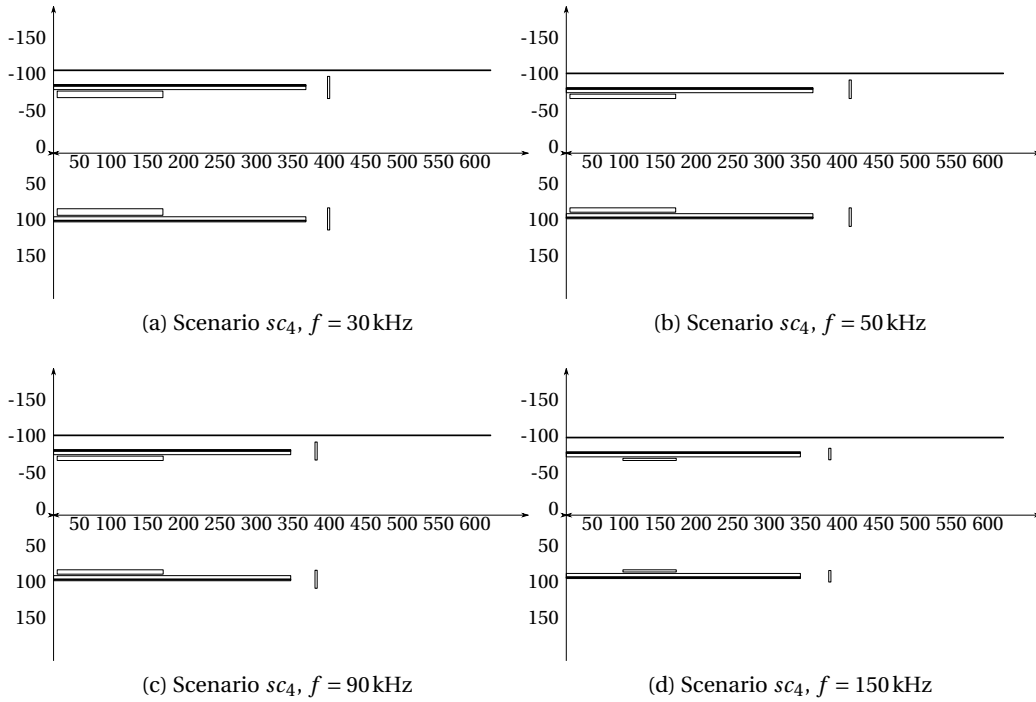
Figure 5.8: The geometries of the optimal solutions

Table 5.10: Optimisation results, scenario sc_5

Frequency	f	30 kHz	50 kHz	90 kHz	150 kHz
Radiated field	B_{max} [μT]	9	6	4.5	3.5
Total losses	P_{loss} [W]	54	50	39	44
Losses prim ferrite	P_{f1} [W]	9	8	8	10
Losses sec ferrite	P_{f2} [W]	11	12	11	12
Losses prim coil	P_{c1} [W]	10	8	4.5	5
Losses sec coil	P_{c2} [W]	14	11	6.5	8
Losses plate	P_{plate} [W]	4	4	4	5
Losses prim ring	P_{r2} [W]	2	1	1	1
Losses sec ring	P_{r2} [W]	2	1	1	1

get the target mutual inductance is better than increasing the radius of the coils and decreasing the number of turns. As expected, the number of turns decreases when the frequency increases. This can be easily explained because the target mutual inductance decreases when the frequency increases while the radius of the coils is the same.

The performances of the transformer given in Table 5.10 for the four frequencies studied leads to very

interesting results. One can note that the emitted radiated field decreases when the frequency increases. However, the losses decrease until 90 kHz but increase again from 150 kHz. This means that an optimal operating frequency exists which minimize the Joule losses. Its value depends on the topology and the geometry of the shielding. However, the associated power electronics introduced in Chapter 3 is not taken into account in this optimisation, which address only the magnetic part of the conversion chain.

5.6 Conclusion

This chapter addresses different shielding topologies for contactless power transfer. As a first step, a preliminary study highlights the necessity of using a shielding structure in order to increase the performances of the transformer. Indeed, the radiated magnetic field is decreased which is a crucial point, especially for high power transfer to ensure the safety of the user. Moreover, a proper shielding decreases the power losses induced in the conductive parts present in the proximity of the transformer. A precise determination of these losses is very important in order to be able to achieve a good efficiency of the system and to avoid a rising of the temperature of the conductive parts.

As a second step, a systematic methodology to design a transformer according to imposed specifications is presented. It consists in splitting the design into two parts. The first one is the electrical part, which consists in determining the inductance values to obtain the required specifications. Then, the geometry and the number of turns of the coils can be determined to meet these values and to achieve the desired performances. This methodology is applied for different shielding topologies. The obtained results confirm that combining ferromagnetic and conductive parts for the shielding increases the efficiency of the transformer and decreases the radiated magnetic field. However, the geometry of the coil and the shielding is fixed in this part.

As a third part, this chapter addresses an optimisation of the shielding geometries. To this purpose, a well-known stochastic optimisation algorithm called GA is introduced. This is a powerful algorithm for multi-objective optimisation under constraints. This algorithm is then implemented in order to optimise the shielding of the transformer presented in the previous sections. Several configurations of the transformer working at different frequencies are optimised regarding two objectives. The first one is to minimise the Joule losses for an imposed transmitted power while the second one is to minimise the radiated magnetic field. The Pareto fronts are plotted for each optimisation undertaken and compared. As a result, increasing the frequency aims to reduce the radiated magnetic field. However, an optimal frequency to reduce the joule losses exists. It means that increasing the frequency does not necessarily leads to a decrease of the losses. Moreover, the presence of the rings at both primary and secondary side increases the performances and reduces the required volume of ferrite plates. However, the modelling does not take into account the power electronics performance, in which the efficiency decreases if the frequency increases.

Innovative contribution to the chapter
In most literature, the transformer for contactless power transfer is only made of two coils. This is suitable when the radiated magnetic field is not a critical point (generally when the transferred power is low) and when there is no conductive parts in the proximity of the transformer. This chapter has addressed different shielding principles and topologies in order to reduce the radiated field and the losses in the conductive parts present in the proximity of the transformer. A preliminary study has

highlighted the increased performances using a shielding. After that, a systematic methodology which consists in separating the electrical and magnetic part has been proposed. As a third part, the different topologies proposed has been optimised using an implementation of the genetic algorithms. Unlike the results found in literature using air transformer without any shielding, the results reveal that increasing the operating frequency does not necessary lead to enhanced performances.

Relative publications to the chapter

- C. Auvigne, F. Copt, C. Winter, Y. Perriard, "Study of Various Winding Topologies for Self-Shielding Induction Cookers", Journal of International Conference on Electrical Machines and Systems (JICEMS), Volume 2, Number 4, December 2013

- D. Shi, C. Auvigne, R. Besuchet, C. Winter, Y. Civet, Y. Perriard, "Optimal design of inductive coupled power transfer systems with applications to electric cars", International Conference on Electrical Machines and Systems (ICEMS) 2013, October 2013

6 Experimentations

Contents

6.1 Introduction

This chapter addresses the different implementations using the theoretical aspects studied in the previous chapters.

The first section presents the implementation of a voltage resonant inverter and its associated control using the full bridge topology. A theoretical modelling of the principle has been presented in Chapter 3. The practical aspects are also addressed in this section.

Contactless power transfer is widely used for contactless battery charger as detailed in Chapter 2. The second section of this chapter addresses a novel concept to provide a battery load cycle. For this purpose, two different compensation topologies studied in Chapter 4 are combined. In the third section, the non-linear behaviour of the battery is used to simplify the design and the control of the transformer.

Finally, an implementation of the control-oriented compensation introduced in Chapter 4 has been made and the performances are compared to an efficiency-oriented one.

6.2 Power electronics

The power resonant inverter can be divided into several parts. A block diagram of the inverter is presented in Fig. 6.1. The power supply brings the electrical energy to transfer the power. The power
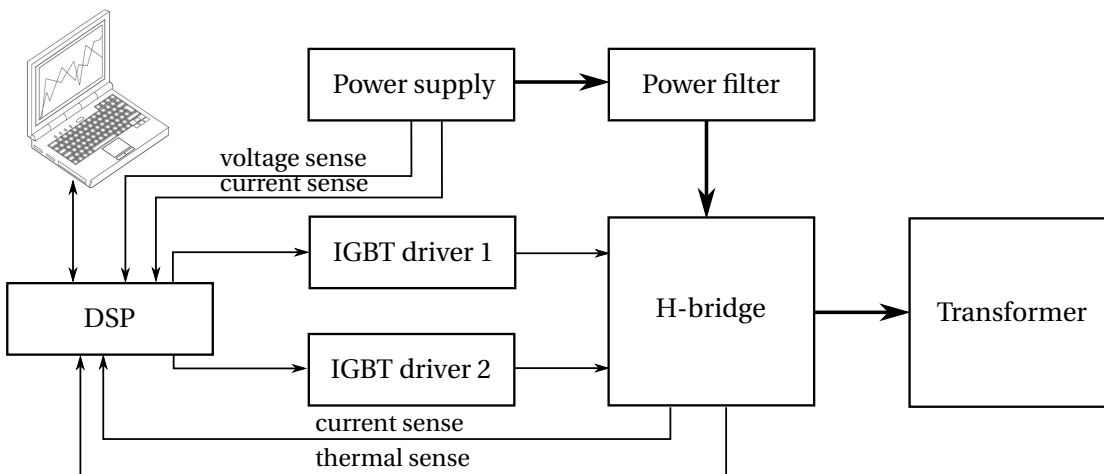
Figure 6.1: Functional diagram of the inverter

filter ensures that the voltage and current at the output of the power supply are continuous. If needed, a power factor corrector can be integrated into this stage. It is useful if the reactive power of the transformer is not fully compensated and the power supply is unidirectional. The H-bridge is made of four switches as presented in Fig. 3.4. In this implementation, the used switches are insulated gate bipolar transistors (IGBT). The driver stage converts the signal from the DSP controller and converts them to drive the gate of the IGBTs. In order to compute the input power and to prevent from overvoltages and overcurrents, the voltage and the current are measured and computed in the

controller. A thermal sensor is also placed in the inverter in order to prevent this latter from possible damages. Finally, the controller is connected to a computer to send the measured parameters and to choose the desired input power.

A picture of the implementation is presented in Fig. 6.2 and Fig. 6.3.

1. Cooling system

2. H-bridge board

3. Driver board

4. Compensation capacitors board

5. Acquisition board

6. DSP board
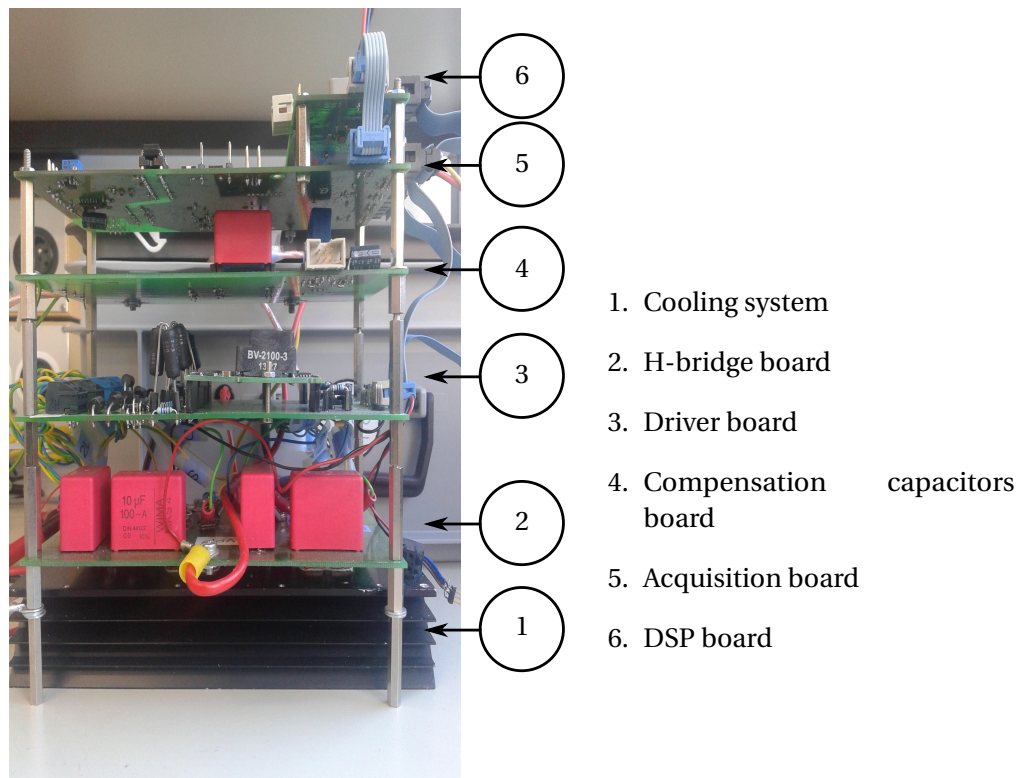
Figure 6.2: Picture of the electronics of the inverter

Command of the inverter

The command signals delivered to the power switches are generated by the controller. The inverter is driven using the phase shift modulation technique introduced in Chapter 3. The command signal of each switch is presented in Fig. 6.4.

In order to avoid any short-circuit of the power supply, the switches S_1 and S_2 must not be enabled at the same time. The principle is the same for the switches S_3 and S_4. For this purpose, a dead time is introduced. During this duration, both S_1 and S_2 (S_3 and S_4) are switched off. As detailed in Chapter 3, the delay T_{shift} between the two legs of the bridge is used to control the power injected into the transformer.

Figure 6.3: Picture of the inverter in its box
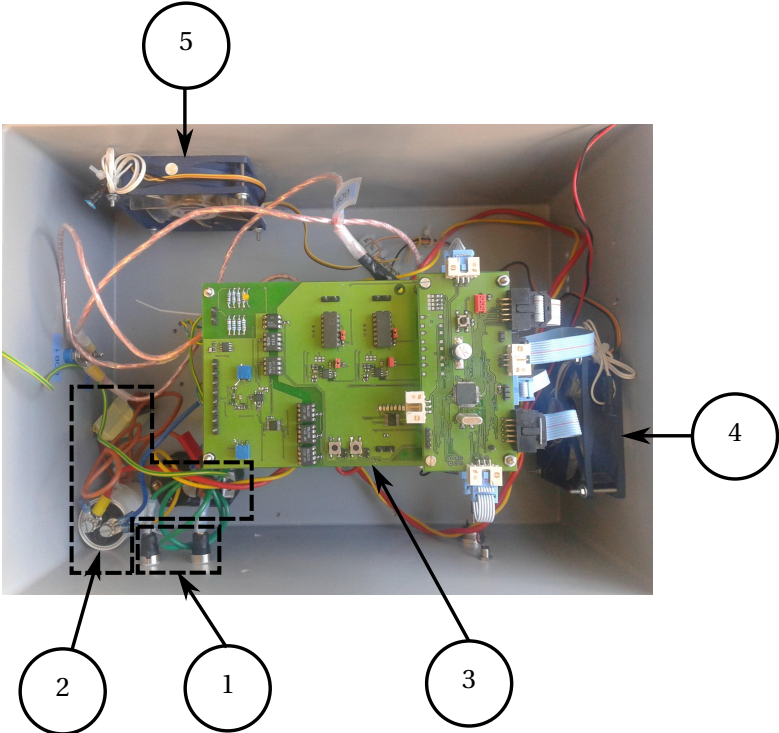
1. Input power connector

2. Power input filter

3. Stack of electronic boards detailed in Fig. 6.2

4. Cooling fan 1

5. Cooling fan 2
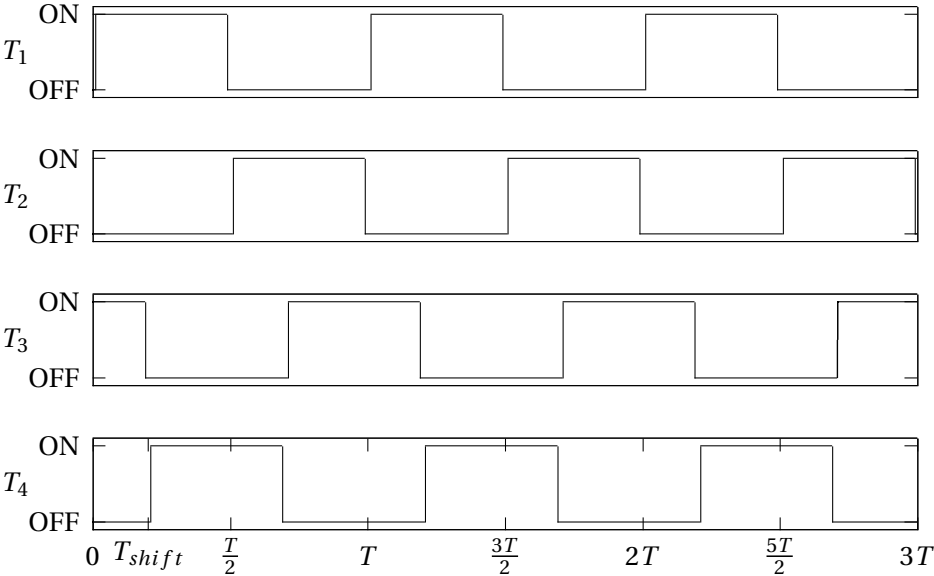
Figure 6.4: Command of the switches for phase shift modulation operation

Acquisition

The measured signals of the power inverter are represented in Fig. 6.5. The quantities U_{DC} and I_{DC} are
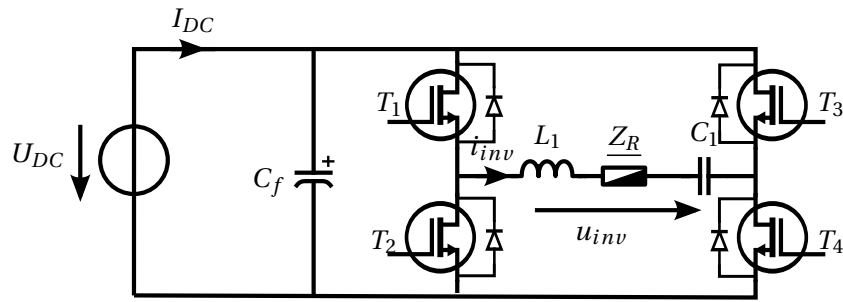
Figure 6.5: Functional diagram of the inverter

DC values so the sampling frequency is not critical. The frequency of the signals u_{inv} and i_{inv} is the one of the inverter (from 20 kHz to 80 kHz in this implementation). Moreover, the inverter voltage u_{inv} is a square-wave so the sampling frequency should be high (at least 10 times the operating frequency) to get a good precision in the acquisition. In order to avoid a high speed acquisition system, it is assumed that the Joule losses in the inverter can be neglected compared to its output power. The input power, which is supposed to equal the output power P_{inv} is defined in (6.1), where φ_{inv} is the phase between u_{inv} and i_{inv}.

$$P_{DC} = U_{DC} I_{DC} = \frac{u_{inv}\,\hat{i}_{inv}\,\cos\varphi_{inv}}{\sqrt{2}} \tag{6.1}$$

The value $\hat{i}_{inv}$ is computed by hardware, as suggested in Fig. 6.6. The voltage V_{in} is given by a current
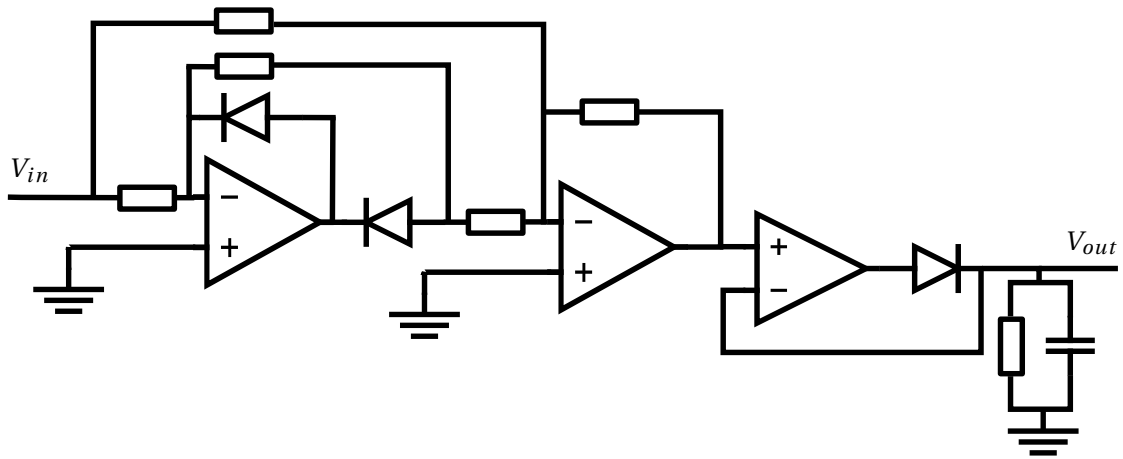
Figure 6.6: Circuitry used for the measurement of $\hat{i}_{inv}$

sensor. The first stage is used to rectify this sine-wave signal. The second stage is to extract the amplitude of the rectified signal using a peak detector. The voltage V_{out} is proportional to the peak current $\hat{i}_{inv}$.

The value u_{inv} can be deduced from the value U_{DC} and the shift angle α using the relation presented

in (6.2).

$$u_{inv} = \frac{2\sqrt{2}}{\pi} U_{DC} \sin(\frac{\alpha}{2})$$

(6.2)

Finally, the power factor of the transformer $\cos\varphi_{inv}$ can be computed combining (6.1) and (6.2), as suggested in (6.3).

$$\cos\varphi_{inv} = \pi \frac{U_{DC} I_{DC}}{\hat{i}_{inv} U_{DC} 2 \sin(\frac{\alpha}{2})}$$

(6.3)

The computation of the power factor $\cos\varphi_{inv}$ is very important because it reveals if the transformer is tuned or not. For instance, if a conductive plate is accidentally placed between the primary and the secondary coil, the transformer is detuned and the value $\cos\varphi_{inv}$ changes. When it occurs, the inverter is switch off for safety reasons.

Hardware protections

In order to prevent any damage to the power electronics, several hardware protections are present and disable the power switches when one of more fault occurs. The different source of faults are summarized in Fig. 6.7. If one or more fault occurs, the inverter is immediately switched off.

- The temperature of the primary coil and switches is acquired. If it is too high, the associated fault occurs.

- The current in the primary coil (sine-wave) is measured. The peak value is extracted and the fault occurs if it is higher than the reference value. The principle is the same for the overvoltage flag.

- The drivers of the power switches of the inverter measure the voltage across the switches and the current to drive the gates. If these values are abnormal, the inverter fault occurs.
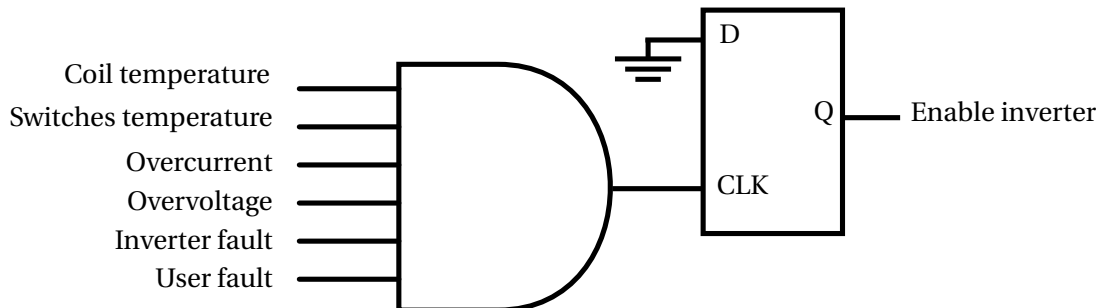
Figure 6.7: The different hardware faults

Efficiency of the inverter

The inverter efficiency is computed in this section in order to be able to compute the efficiency of all the conversion chain from the DC power supply to the load. However, a detailed study of the different effects in presence is beyond the scope of this chapter. Some relevant informations can be found in [21].

The input power of the inverter is defined in (6.4). The output power of the inverter is defined in (6.5).

$$P_{in} = U_{DC} I_{DC} \tag{6.4}$$

$$P_{inv} = \frac{2\pi}{\omega} \int_0^{\frac{2\pi}{\omega}} u_{inv}(t) i_{inv}(t) \tag{6.5}$$

The efficiency of the inverter can be easily deduced combining (6.4) and (6.5), as suggested in (6.6).

$$\eta_{inv} = \frac{\frac{2\pi}{\omega} \int_0^{\frac{2\pi}{\omega}} u_{inv}(t) i_{inv}(t)}{U_{DC} I_{DC}} \tag{6.6}$$

The inverter losses are mainly due to two effects of the switches. The first one is called static losses and is due to the voltage $V_{CE,SAT}$ across the IGBTs. It is defined in (6.7). The second one is due to the commutation of the switches and is called switching losses. It is defined in (6.8) (t_0 represents the beginning of the switching of the switches and t_1 the end of the switching). The switching losses can be cancelled if the phase between the current and the voltage is positive (this is called "soft switching").

$$P_{V,COND} = 2 V_{CE,SAT} I_{inv} \tag{6.7}$$

$$P_{V,SW} = 2 \int_{t_0}^{t_1} v_{CE}(t) i_{inv}(t) \cdot dt \tag{6.8}$$

In order to highlight these different losses, the input voltage is regulated to obtain $300\,\mathrm{W}$ at the output of the inverter. The frequency is a little bit shifted around the resonant frequency of the transformer. As a first step, the inverter is placed in a hard switching configuration (the working frequency is smaller than the resonant one). As a second step, it is placed in a soft switching configuration (the working frequency is higher than the resonant one). The results are listed in Table 6.1. As expected, the inverter efficiency is higher using the soft switching configuration.

Table 6.1: Measurement effectuated on the inverter

Parameters	Soft switching	Hard switching
U_{DC} (V)	31	31
I_{DC} (A)	5.2	5.6
P_{out} (W)	300	300
P_{in} (W)	320	360
η	0.94	0.83

6.3 Improving robustness dealing with several compensation topologies

The aim of this application is to use the load characteristics of several compensation topologies in order to generate a battery load cycle.

Battery manufacturers provide a load profile. Basically, one load cycle is based on two phases:

- A constant current mode, until the battery reaches a given voltage;

- A constant voltage mode, until the current decreases almost to zero.

In order to ensure such a profile, using only one transformer with one compensation topology is not enough. However, several solutions could be adopted:

1. Add a DC/DC converter with a ballast load at the secondary side. Then, the supply voltage could remain constant during the whole charging cycle since the DC/DC and the ballast load ensures the load profile itself. This solution is implemented in [75]. Thus, the supply voltage remains constant. This solution is not investigated since it requires an additional power converter;

2. Adapt the supply voltage in order to change the power transferred to the battery. The inconvenient of this method is the need of a large range of the input voltage. Phase Shift Modulation (PSM) technique avoids the use of an additional DC/DC converter at the primary side but switching losses are increased because of the large range of voltage to generate. This is done in [77];

3. Design the transformer according to load characteristics. As developed in Section 4.4, Eq. (4.25) shows that a SS topology is suitable for the constant-current mode, while (4.49) shows that a SP topology is suitable for the the constant-voltage mode.

Using this last scenario, transition from SS topology to SP topology can be achieved as illustrated in Fig. 6.8. When a SS topology is needed, the secondary is connected as shown in Fig. 6.8a. Thus, the compensation capacitance $C_{2;ss}$ is connected in series with the whole secondary coil. When a SP topology is needed, the compensation capacitance $C_{2;sp}$ is then connected in parallel with only part of the secondary coil which was split into two asymmetrical windings (Fig. 6.8b). The power must be switched off before the transition.

(a) SS connection

(b) SP connection
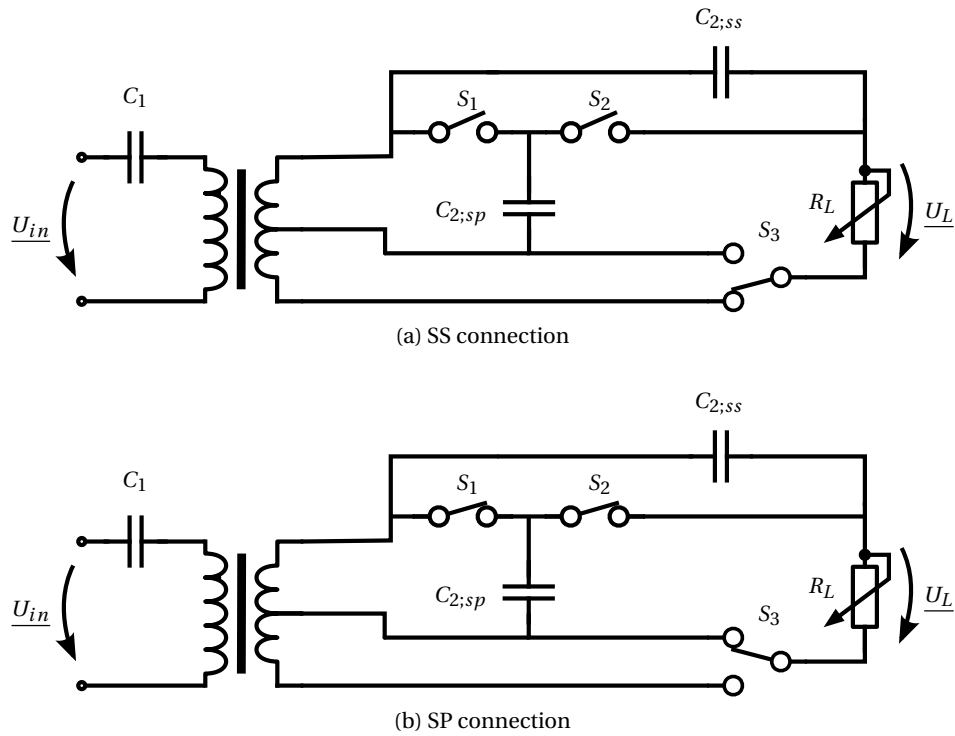
Figure 6.8: Schematic of the transformer with secondary switching circuitry

Implementation

In order to validate the development presented above, an ICPT featuring a switchable topology between SS and SP (Fig. 6.8) has been build (Fig. 6.9). The overall conversion chain of the prototype realised is shown in Fig. 6.10. In order to simulate the battery, an electronic load is used.
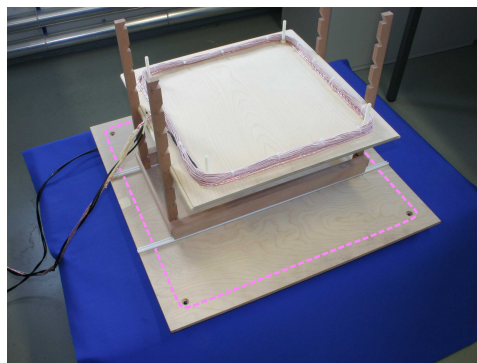
Figure 6.9: Transformer used for the measurements

The geometrical parameters of the transformer are given in Table 6.2. Fig. 6.11 presents the geometry of the transformer with some of its main parameters. Its corresponding electrical parameters of the transformer are presented in Table 6.3.

Since no dynamical properties are required, basic electromechanical relays are suitable to this purpose.
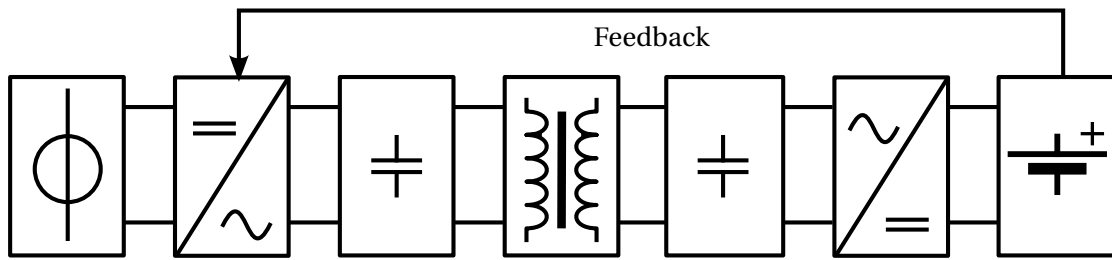
Figure 6.10: Overview of the overall conversion chain
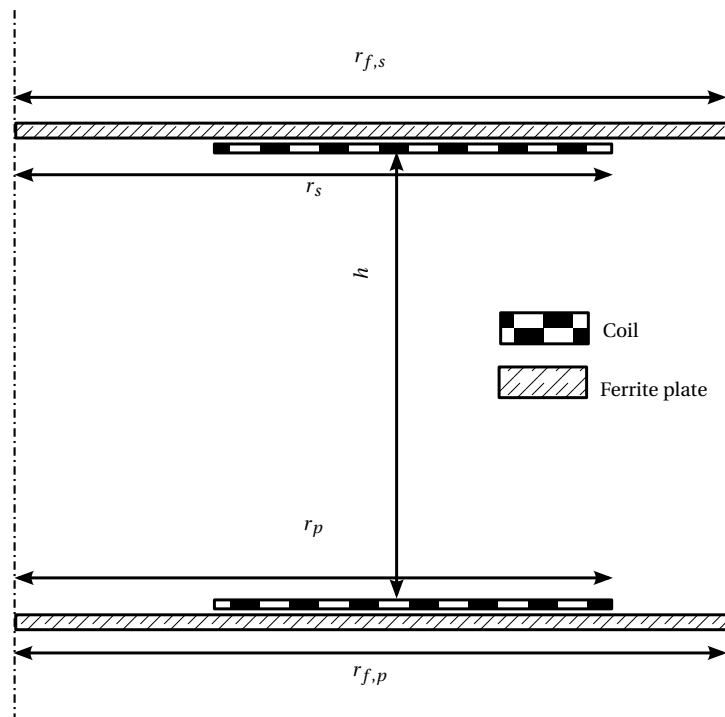
Figure 6.11: Geometry of the transformer

Table 6.2: geometric parameters of the transformer

Parameters	Values
Size of coils [mm]	$W_1 = 600$; $W_2 = 400$
airgap [mm]	$h = 280$
Number of turns	$N_1 = 30$; $N_{2;ss} = 30$; $N_{2;sp} = 3$
Radius of wires (SS) [mm] [1]	$a_1 = 0.55$; $a_{2;ss} = 0.55$
Radius of wires (SP) [mm] [1]	$a_1 = 0.55$; $a_{2;sp} = 2.4$

[1] Equivalent radius of 100 strands of Litz Wire

Table 6.3: Electrical parameters of the transformer

Parameters	Values
Frequency [kHz]	50
Inductances [uH]	$L_1 = 1200$; $L_{s;ss} = 1090$; $L_{s;sp} = 14$; $M_{ss} = 115.5$; $M_{sp} = 11$
Resistances [Ω]	$R_1 = 1.87$; $R_{2;ss} = 1.51$; $R_{2;sp} = 0.013$
Capacitances [nF]	$C_1 = 8.4$; $C_{2;ss} = 9.03$; $C_{2;sp} = 749$
Dissipation factor	$\tan\delta_{C_1} = 0.1\%$; $\tan\delta_{C_{2;ss}} = 0.1\%$; $\tan\delta_{C_{2;sp}} = 0.1\%$
Relays resistance	$R_r = 60$ mΩ
Battery load specifications	$30 < U_{bat} < 80$ $I_{bat} = 1.6$A

The minimal nominal currents required for the switches are presented in Table 6.4.

Table 6.4: Minimal requirements for the switches

- Switch number	Nominal current ratings
S_2, S_3	$I_L = 2$A
S_1	$I_{2,SP} = 20$A

In order to validate the models developed in the previous sections, several measurements have been made for both SS and SP topologies.

At this step, only the transformer and its associated compensation capacitances are taken into account in order to compare the models presented in Chapter 4 and the measurements undertaken. Fig. 6.12 and Fig. 6.13 compare theoretical and measured load characteristics and efficiency for both SS and SP topologies.

According to the load characteristics presented in Section 4.4.5, the SS topology leads to a current source while the SP topologies leads to a voltage source. One can see that the efficiency is higher for the SS topology than for the SP one. Finally, the maximal error between the model and the measurements is 10%.

The voltage and current in the rectifier are shown in Fig. 6.14 for the SS topology and Fig. 6.15 for the SP topology. Since the SS topology leads to a current source, the current is a sine-wave and the voltage is square. Since the SP topology leads to a voltage source, the current is square while the voltage is a sine-wave.

When the battery is discharged, the battery voltage is $U_{bat} \approx 30$V. The battery under test is charged with a current of $I_{bat} = 1.6$A until its voltage reaches $U_{bat} = 80$V, while using the SS topology. Then, the secondary is switched to SP topology in order to begin the constant-voltage phase, until battery
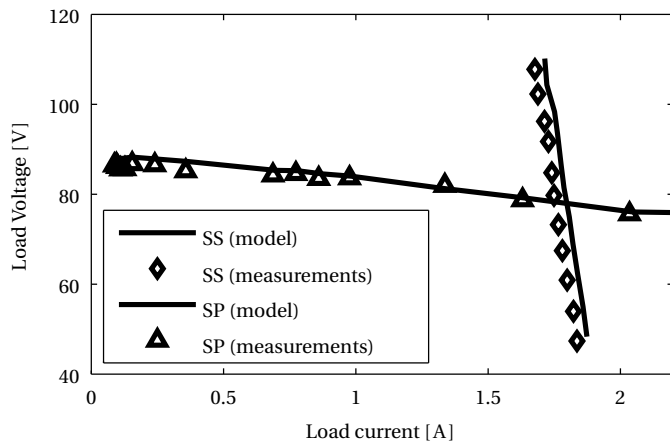
Figure 6.12: Load characteristics for SS and SP topologies for U_{in} imposed
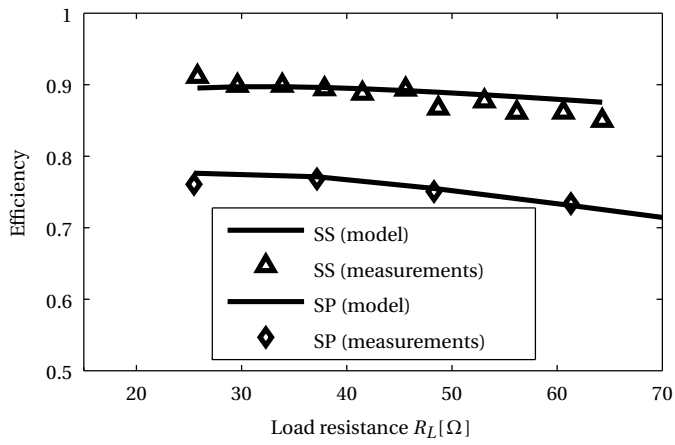
Figure 6.13: Transformer efficiency for SS and SP topologies
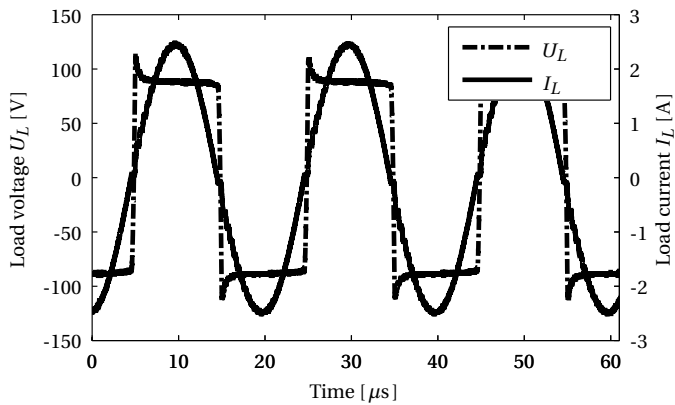
Figure 6.14: Load voltage U_L and current I_L for SS topology represented in time domain

current decreases to $I_{bat} < 0.03 I_c$. The battery is then fully recharged.

The primary voltage is adapted to provide the theoretical charge cycle (a constant current mode

110
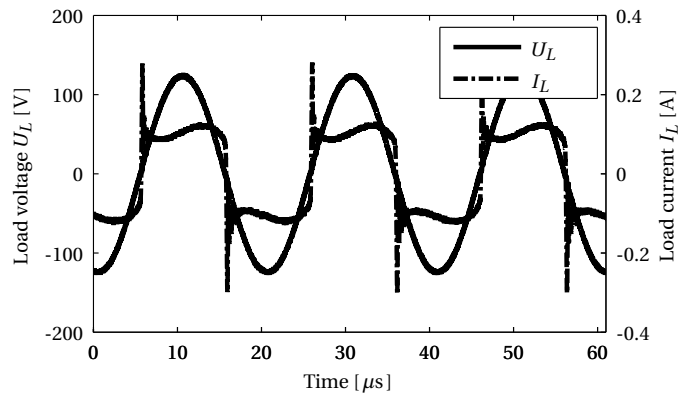
Figure 6.15: Load voltage U_L and current I_L for SP topology represented in time domain

followed by a constant voltage mode). This experiment is undertaken for the following three scenarios :

- Using SS topology for the constant current mode and switching to SP topology for the constant voltage mode,

- Using SS topology for the whole charging cycle,

- Using SP topology for the whole charging cycle.

For these two last scenarios, the primary voltage is adapted in order to provide the theoretical load profile (an ideal current source and an ideal voltage source). The results are shown in Fig. 6.16. For SS or SP topology only, the primary voltage should be adapted from $U_{in} = 60\,\text{V}$ to $U_{in} = 80\,\text{V}$. Combining these two topologies, $U_{in} = 78\,\text{V}$ to $U_{in} = 81\,\text{V}$, due to the serial resistances of the coils.

The efficiency, function of the charge state, is shown in Fig. 6.17.
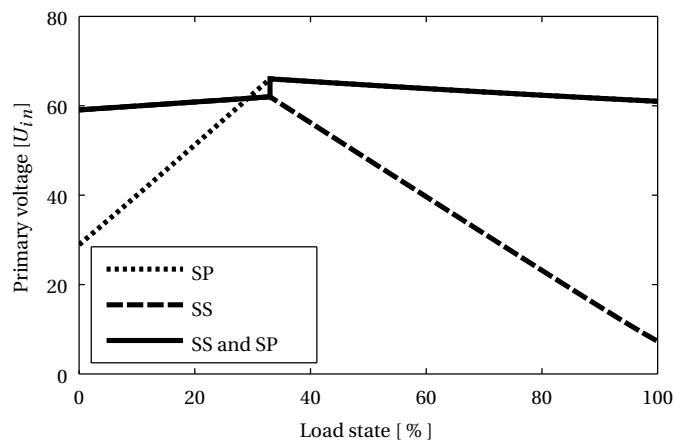
Figure 6.16: Primary voltage function of the charge state to obtain an ideal current and voltage source

One can note that with this prototype, the efficiency of the SP topology gives a lower efficiency (about 10%) than the SS topology.
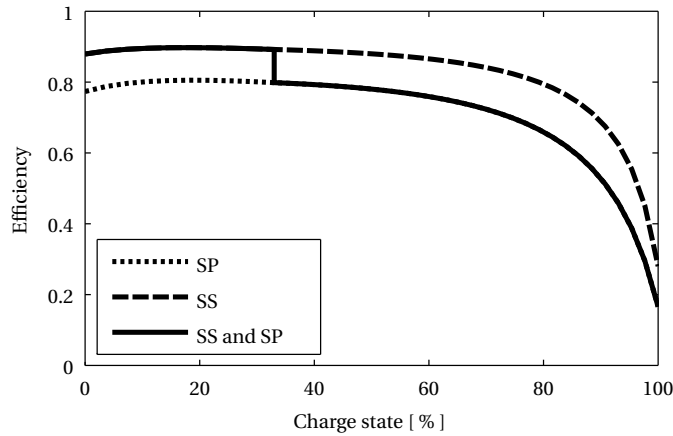
Figure 6.17: Transformer efficiency, function of the charge state

As a result, the main advantage of the switching topology solution is to simplify the control of the system since it can be driven by a constant supply. The transition from SS to SP topology is made by disconnecting the secondary coil L_2 and shorts the secondary compensation capacitance $C_{2;ss}$. Thus, the power supply must be turned off before the switching sequence to ensure that no energy remains in the system during the switching sequence.

Although the power electronics at the primary part is simplified since the supply voltage remains constant during all the charge cycle, three relays are added at the secondary part to perform the switching sequence. Additional serial resistances in the system are introduced affecting the efficiency. Since the resistance of the relays is negligible compared to the serial resistance $R_{2;ss}$ of the secondary coil (for SS mode), the relays do not affect the efficiency of SS mode. However, the switch S_1 is placed into a parallel resonant loop. The current through this switch is ten times higher than for SS topology. As a result, the efficiency of the transformer prototyped is 10% lower for the SP topology than for the SS topology. In order to study the impact of the resistance of this switch and the capacitors dissipation factor, the efficiency as a function of the quality factor of the secondary part Q is shown in Fig. 6.18.
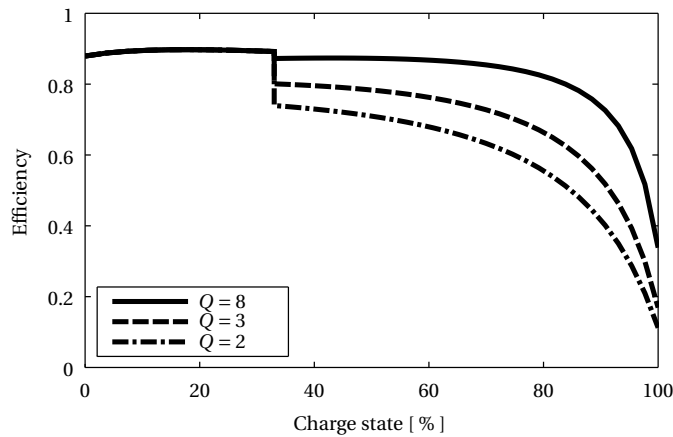
Figure 6.18: Transformer efficiency for several quality factors of the secondary part

The prototype has a quite low quality factor ($Q = 2$). The same efficiency as the one for the SS topology can be achieved with a higher quality factor($Q = 8$). This can be achieved using $\tan\delta_{C_{2;sp}} = 0.1\%$,

$R_r = 10$ mΩ and $R_{2;sp} = 5$ mΩ, which is an easy solution to implement.

6.4   Simplifying control of a non-linear load

In order to validate the development undertaken in Chapter 4, a prototype has been set-up as illustrated in Fig. 6.19. The characteristics of the transformer are shown in Table 6.5 and Table 6.6. The DC supply voltage is set to 40 V and the phase shift modulation technique is used in order to change the effective voltage of the input of the transformer. An electronic load set in a constant voltage mode is used in order to simulate the behaviour of the battery. The battery voltage U_{bat} is changed from 30 V to 60 V. Three different charging sequences consisting in changing the battery current I_{bat} are made. A first-harmonic methodology is used for the measurements. This means that only the first harmonic of the signals is taken into account. The practical results are shown in Fig. 6.20.

(a)   Cross-section   of   the   transformer   (axis-symmetric)

(b) Picture of the transformer

(c) Picture of the power electronics
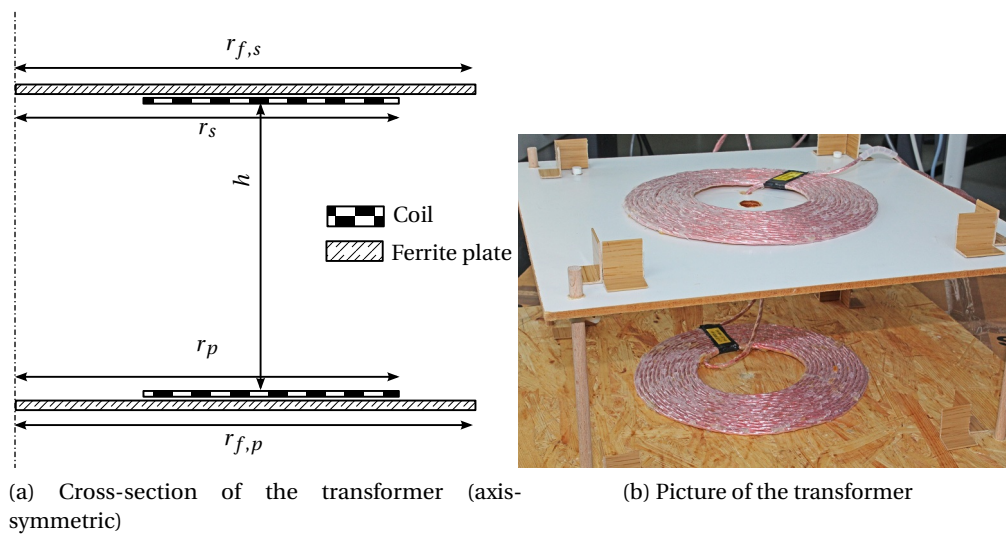
Figure 6.19: Achieved prototype

The value of the equivalent resistance R_L when the transformer is loaded by both the rectifier and the battery can be determined solving (6.9).

Table 6.5: Main geometric parameters of the transformer

Parameter	Value
Radius of the coils	$r_p = 100\,\text{mm}$, $r_s = 100\,\text{mm}$
Radius of the ferrite	$r_{f,p} = 140\,\text{mm}$, $r_{f,s} = 140\,\text{mm}$
Airgap	$h = 60\,\text{mm}$
Number of turns	$N_1 = 15$, $N_2 = 15$
Radius of wires[1]	$r_{eq} = 1.8\,\text{mm}$

[1] Equivalent radius of 90 strands ($r_w = 0.12\,\text{mm}$) of Litz-wire.

Table 6.6: Electrical parameters of the transformer

Parameter	Value
Frequency	$50\,\text{kHz}$
Self inductances	$L_1 = 65\,\mu\text{H}$, $L_2 = 65\,\mu\text{H}$
Mutual inductances	$M = 22\,\mu\text{H}$
Coupling factor	$k = 0.34$
Resistances	$R_1 = 80\,\text{m}\Omega$, $R_2 = 80\,\text{m}\Omega$
Capacitances	$C_1 = 150\,\text{nF}$, $C_2 = 150\,\text{nF}$

$$
\begin{cases}
\underline{U_{in}} = -\text{j}\omega_0 M \underline{I_L} \\
\text{j}\omega_0 M \underline{I_1} = \underline{U_L} \exp^{\text{j}\arg \underline{I_L}} \\
R_L = \dfrac{\underline{U_L}}{\underline{I_L}}
\end{cases}
\tag{6.9}
$$

Solving (6.9) leads to (6.10).

$$
R_L = \frac{\omega_0 M U_L}{U_{in}}
\tag{6.10}
$$

The relation between the load voltage U_L and the DC battery voltage U_{bat} is given in (6.11).

$$
U_L = \frac{\pi}{2\sqrt{2}} U_{bat}
\tag{6.11}
$$

The transmitted power for SS topology is given in (6.12).

115

(a) Equivalent load

(b) Primary current

(c) Load currentt

(d) Efficiency
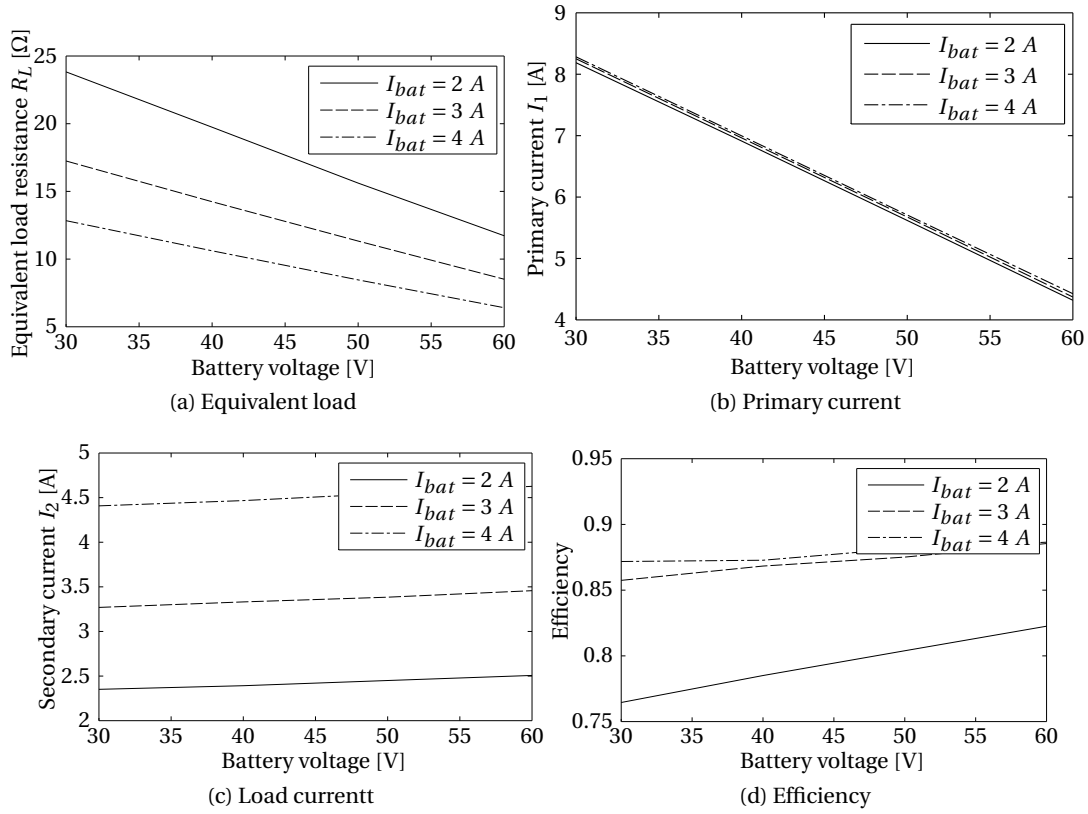
Figure 6.20: Results obtained from the undertaken experiments

$$P_L = \frac{2\sqrt{2}U_{bat}}{\pi\omega_0 M} \cdot U_{in} \qquad (6.12)$$

$$I_1 = \frac{2\sqrt{2}}{\pi\omega_0 M} \cdot U_{bat} \qquad (6.13)$$

The measured equivalent resistance R_L is shown in Fig. 6.20a. According to (6.10), the resistance value is proportional to the battery voltage U_{bat} and the battery current I_{bat}.

The primary current, being a function of the battery voltage and current is shown in Fig. 6.20b. One can see that the primary current remains constant while the battery current changes. This result is in agreement with (6.13).

The secondary current I_2, function of the battery voltage and current, is shown in Fig. 6.20c. According to the load characteristics studied in Chapter 4, the load current barely depends on the battery voltage. This confirms that the SS topology behaves as a current source. The small slope is due to the internal resistances of the different elements of the transformer. A more accurate formula, taking into account the coil resistances, is presented in [2].

Finally, the efficiency of the transformer itself is presented in Fig. 6.20d. The efficiency does not take into account the losses in the power electronics (the inverter and the rectifier). However, one can see that it increases as the transmitted power increases. This can be explained because a first harmonic analysis has been made for these results. Indeed, the non-linear losses in the IGBT and the diodes affect the efficiency of the transformer itself.

6.5   Implementation of the control-oriented compensation

The aim of this section is to compare the efficiency-oriented compensation and the control-oriented one. For this purpose, a transformer using PS topology has been realised. Fig. 6.21 shows the realisation of the transformer in presence of its associated electronics. Its main geometrical and electrical parameters are listed in Table 6.7 and Table 6.8.
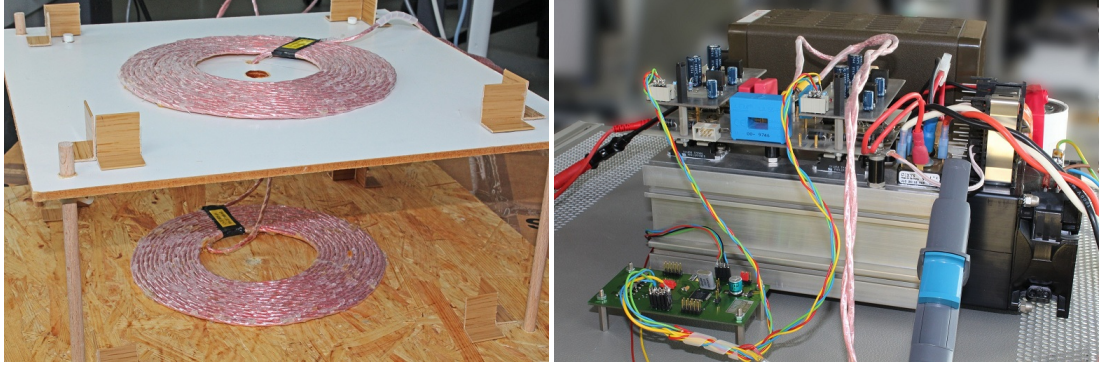
Figure 6.21: Transformer used for the validation and its associated electronics

Table 6.7: Geometric parameters of the transformer

Parameter	Value
Radius of the coils	$R_1 = 200\,\text{mm}$, $R_2 = 200\,\text{mm}$
Airgap	$h = 30\,\text{mm}$
Number of turns	$N_1 = 15$, $N_2 = 15$
Radius of wires[1]	$r_{eq} = 1.8\,\text{mm}$

[1] Equivalent radius of 90 strands ($r_w = 0.12\,\text{mm}$) of Litz-wire.

Table 6.8: Electrical parameters of the transformer

Parameter	Value
Frequency	$50\,\text{kHz}$
Self inductances	$L_1 = 40.5\,\mu\text{H}$, $L_2 = 39\,\mu\text{H}$
Mutual inductances	$M = 30\,\mu\text{H}$
Coupling factor	$k = 0.4$
Resistances	$R_1 = 70\,\text{m}\Omega$, $R_2 = 66\,\text{m}\Omega$
Capacitances (efficiency compensation)	$C_1 = 248\,\text{nF}$, $C_2 = 260\,\text{nF}$
Capacitances (control compensation)	$C_1 = 250\,\text{nF}$, $C_2 = 318\,\text{nF}$

According to Section 4.4, the primary capacitance C_1 set for an efficiency-oriented compensation depends on the load resistance R_L for PS topology. Since the capacitance C_1 is designed for the nominal load value, the resonant pulsation ω_0 changes regarding load variations.

In order to highlight this phenomenon, the transformer is tuned for a nominal load of $30\,\Omega$ for the efficiency-oriented compensation, and then for the control-oriented one. The primary voltage U_{in} is

set to 80 V. Different resistances R_L are then connected to the transformer for the two compensations. The equivalent reactance of the whole transformer $\text{Im}(\underline{Z_t})$ is compared in Fig. 6.22.
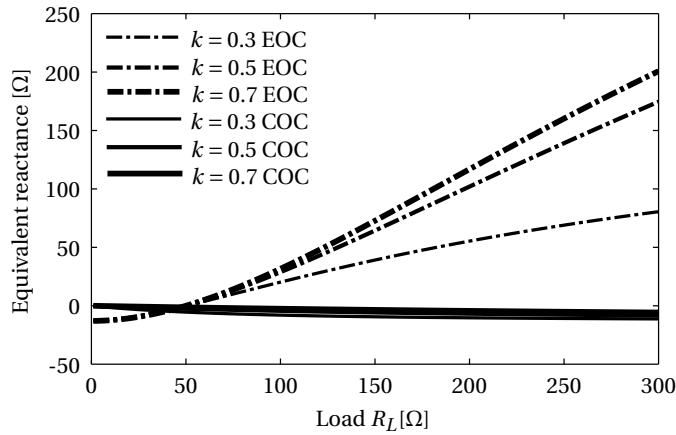
Figure 6.22: Comparison of the equivalent reactance of the whole transformer for different coupling factors k for efficiency-oriented compensation (EOC) and control-oriented compensation (COC)

As expected, the equivalent reactance of the whole transformer is strongly dependant on the load resistance R_L and the coupling factor k for the efficiency-oriented compensation. It is quasi independent for the control-oriented one. The weak dependency of the latter is due to the serial resistances of the coils and the capacitances.

The current flowing in the primary coil I_1 is shown in Fig. 6.23a. As expected, this current is smaller with the efficiency-oriented compensation for small load values R_L. For larger values of R_L, the primary current I_1 is the same for both compensations. The transmitted power is shown in Fig. 6.23b. As expected, it is about 15% higher using the COC for small values of R_L while it is almost the same for both compensations for larger values of R_L. The others main results are listed in Table 6.9.

(a) Primary current I_1 function of the load R_L (b) Transmitted power P_L function of the load R_L
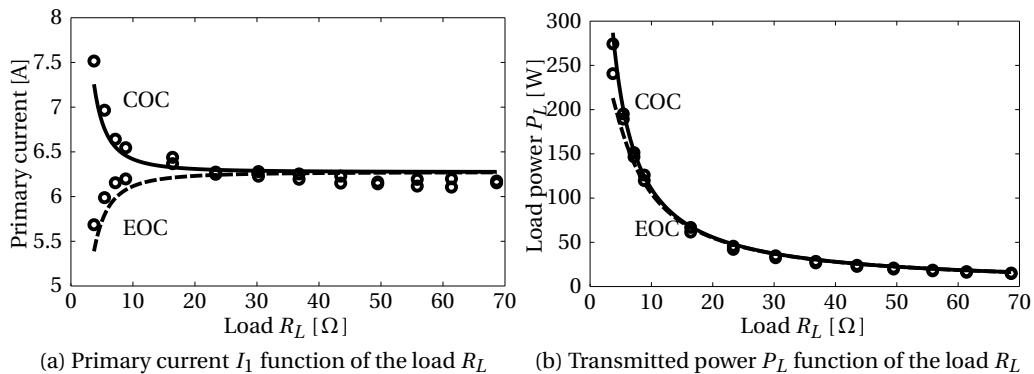
Figure 6.23: Efficiency and transmitted power

According to Fig. 6.23a, Fig. 6.23b and Table 6.9, the measurements undertaken are coherent with the modelling presented in Section 4.4.2 since the maximal error is about ten percent.

Table 6.9: Comparison between theoretical model
and measurements

Parameter	Theoretical value	Measured value
$f_0 [kHz]$	50	50.1
$U_p [V]$	80	80
$\frac{\Delta U}{\Delta I} [\Omega]^1$	-0.75	-0.6
$\frac{\Delta U}{\Delta I} [\Omega]^2$	-0.1	-0.09
$\eta_{EOC} [-]$	0.95	0.92
$\eta_{COC} [-]$	0.95	0.92

[1] For efficiency-oriented compensation.
[2] For control-oriented compensation.
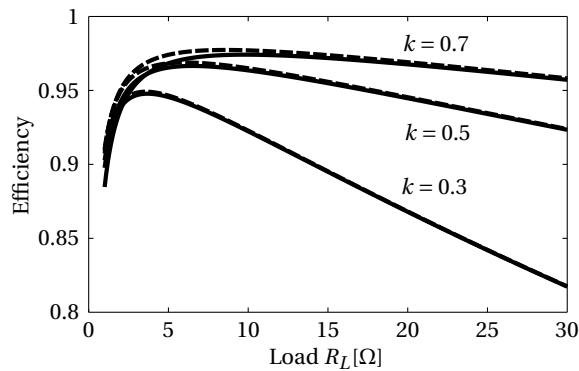
Figure 6.24: Comparison of the efficiency for different coupling factors k for efficiency-oriented compensation (dashed-line) and control-oriented compensation (plain line)

6.6 Conclusion

Unlike the previous chapters, this one addresses practical considerations and implementations. The implementation of the voltage resonant inverter is introduced. The power stage is first presented. Then, the driver stage and the hardware protections are presented in order to immediately switch off the inverter as soon as a fault occurs.

This chapter also presents contactless power transfer for a battery charger. A load battery cycle must be provided for this purpose. Generally, an additional power converter is introduced between the secondary part of the transformer and the battery in order to provide a current source for the first step of the charging and a voltage source for the second step. This work presents a novel methodology which consists in dealing with several compensation topologies studied in Chapter 4. Indeed, the additional power electronics can be avoided and the battery is directly connected to the secondary part of the transformer. The secondary part features switches which allow to switch between SS and SP topologies to get a current source for the first step and a voltage source for the second one.

Moreover, connecting the battery directly to the secondary part of the transformer introduces a non linearity into the system. As studied in this chapter, the battery and its associated rectifier can be modelled by a resistance which depends on the input voltage and the operating frequency. In literature, a power converter is introduced in order to compensate this non linearity. In this work, a modelling of this non linearity is made. Moreover, this non-linearity is used in order to simplify the design and the control of the transformer. It is shown that for the SS compensation topology, the current in the primary coil remains constant when the supply voltage changes. This is a very important result because the size of the conductor of the primary coil can be designed independently of the transferred power. A prototype has been set up to validate these results.

Finally, a transformer using the PS compensation topology has been built. The performances of the two compensation methodologies studied in Chapter 4 are compared. According to the modelling, the efficiency-oriented compensation leads to a higher efficiency than the control-oriented one, especially for high magnetic coupling and small load values. However, the magnetic coupling for contactless power transfer purpose is generally low ($k < 0.2$). Therefore, the difference of the transformer efficiency is small ($\Delta\eta < 1\%$). Moreover, when the load value changes, the transformer using the efficiency-oriented compensation is detuned while the one using the control-oriented one remains tuned. As a result, the novel compensation methodology is very useful for variable loads. As an example, the PS topology is used with the efficiency-oriented compensation in [23]. To compensate the load variations, the frequency changes. However, the efficiency is decreased in this case because the operating frequency does not match the secondary resonant frequency.

Innovative contribution to the chapter

The different implementations undertaken have been presented in this chapter. In order to simplify the control of a contactless battery charger, two different implementations dealing with the behaviour of the compensation topologies have been presented. A novel solution which consists in combining two different compensation topologies for their different load characteristics have been studied and realised. This innovative concept has been patented [37]. Moreover, the novel compensation methodology introduced in Chapter 4 called "control-oriented compensation" has been implemented and is compared with the "efficiency-oriented compensation" methodology.

Relative publications to the chapter

- D. Ladas, Y. Perriard, C. Auvigne and P. Germano, Energy conversion system, July 2 2014, EP Patent App. EP20,130,181,857

- C. Auvigne, P. Germano, D. Ladas, Y. Perriard, "About tuning capacitance in inductive coupled power transfer", Power Electronics and Applications (EPE 2013), Proceedings of the 2011-15th European Conference on, September 2013

- C. Auvigne, P. Germano, D. Ladas, Y. Perriard, "A dual-topology ICPT applied to an electric vehicle battery charger", Electrical Machines 2012, XXth International Conference On, sept. 2012

- C. auvigne, P. Germano, Y. Civet, Y. Perriard, "Design considerations for a contactless battery charger", Power Electronics and Applications (EPE 2014), Proceedings of the 2011-15th European Conference on, September 2014

7 Conclusion

Contents

7.1 General conclusion

This work addressed the modelling and design considerations on inductive couplers for contactless power transfer purpose. As a first step, a state of the art on inductive coupled power transfer systems was made. The different applications of this technology for different power ranges have been introduced. The different challenges, which depend on the power in presence have been highlighted. The topology of the system, the operating frequency and the geometry of the coils depend on the application.

In order to guarantee the success of an appropriate design of such a system, an accurate modelling is mandatory. A modelling of the transformer and its constitutive components has been made to this purpose. An analytical approach which depends on the environment complexity has been proposed. The different electric equivalent models of the transformer have been presented. The domain of validity of each representation has been studied. Then, these representations have been generalized for an environment containing conductive and ferromagnetic parts. In this context, the Eddy currents in the conductive parts and hysteresis losses in the ferromagnetic parts have been studied, resulting in the proposition of a FEM modelling.

Unlike conventional transformers, the leakage magnetic flux is high for inductive couplers. The operating frequency is thus increased but the reactance values increases too. The performance of low-coupled transformer can be greatly increased if the reactive power due to the self inductance is capacitively compensated. The main compensation topologies have been presented in Chapter 4. The corresponding load characteristics have been developed. It allows splitting the system design into two parts : the magnetical one and the electrical one. The well-known compensation methodology which consists in maximising the efficiency of the transformer has been studied. It suffers from the load value and the coupling factor dependencies for several compensation topologies. A novel compensation methodology which consists in designing the compensation independently of these parameters has been proposed. As a result, the efficiency is almost the same than for the classical compensation, but the dependencies are partially or totally cancelled. Finally, the frequency response of the compensated transformer for the different topologies has been studied.

The magnetic design of the transformer has been then investigated in order to improve its performance. Indeed, the proximity of conductive parts induces additional losses in the system. Furthermore, the radiated magnetic field emission next to the transformer has been studied in order to be reduced. This is a very important point to ensure the safety of the user. Several shielding topologies have been proposed for this purpose. A systematic approach to design a system has been developed and applied. Finally, an optimizer based on a genetic algorithm is implemented with the FEM model of the transformer and adapted for constraint multi-objective optimisation. The efficiency and maximum radiated magnetic field for different transformers are to be minimized. It has been shown that increasing the operating frequency does not lead to increase the transformer efficiency.

Finally, the practical realisations prototyped in the scope of the work have been presented. The practical results obtained have been compared to the modelling presented in the previous chapter.

7.2 Summary of the main contributions of this work

- *Determination of the load characteristics for the different compensation topologies :* The load characteristics of the transformer represent the variation of the load current and the load voltage when the load value changes. In literature, some information is available on the general

behaviour of the transformer for specific topologies and control. In this work, the load characteristics are developed for the four compensation topologies and for three different types of control of the transformer. For each case, the nature of the load characteristics and the exact equation are given. This development is very useful to choose the most suitable topology for given specifications and design the electrical part of the system. Moreover, the load characteristics are used to generate a load battery cycle combining two different compensation topologies.

- *Novel compensation methodology :* in literature, almost each inductive coupled system uses compensation capacitances at both primary and secondary side in order to increase the performances. However, in most compensation topologies, the value of these capacitances depends on the load value. Indeed, the transformer is detuned when the load changes. To compensate this effect, two solutions can generally be used. The first one consists in tracking the frequency to retune the system. However, this new "optimal" working point leads to altered performances. The second one consists in adding a power converter to keep the apparent load constant. In this solution, an additional power stage is required. In this work, a novel compensation which aims to choose the values of compensation capacitances independently of the load value for PS topology is proposed. The obtained efficiency is nearly not altered compared to the conventional compensation and the transformer is still tuned regarding load variations. However, it is detuned when the mutual inductances value changes.

- *Determination of general criteria for the bifurcation phenomenon :* the main investigations of the behaviour of the capacitive compensated transformer focuses on the characteristics when the latter is working at the resonant frequency. However, the response of the transformer is completely different when it is working at a different frequency or when it is detuned. Depending on the parameter values of the transformer, the impedance can dramatically decrease, which leads to very high currents in the transformer. In literature, this phenomenon is called the "bifurcation operation". Existing research has been investigated to determine the criteria of the bifurcation operation. However, the development are restricted to very high power applications since the results are available for coils which have a very low quality factor (between 1 and 10). In this work, general criteria are given for the four compensation topologies based on Cardan's formula.

- *Study of transformer shielding using ferromagnetic and conductive parts :* in most applications, the transformer is operating in presence of conductive and ferromagnetic parts, which are present in the environment. For example, if the application is the charging of electric vehicles, the secondary part is placed near the iron chassis of the vehicle. If the transformer is not shielded, its performances are severely decreased since Joule losses are induced in the conductive parts. Moreover, using a shielding aims to decrease the radiated magnetic field. This is a very important point, especially for high power transfer, to meet the guidelines regarding the safety of the user. In the scope of this work, several shielding topologies combining ferromagnetic and conductive parts are introduced. A systematic design approach, which consists in separating the electrical and the magnetical design into two independent parts is presented and applied. An optimisation of the geometry of the shielding based on genetic algorithms is performed ans the main results are discussed.

- *Modelling of the transformer loaded by a battery :* the electrical modelling of the transformer generally assumes that it is loaded by a linear resistance. However, when a battery is connected, the response of the transformer is different since the battery imposes the secondary voltage. Using the SS compensation topology simplifies the design of the transformer. As a result, the primary current is totally independent of the power transmitted to the battery. This phenomenon

is due to the non-linearity of the system, it is not possible to obtain similar results using linear resistance.

7.3   Outlook and perspectives

- *Interoperability* : In an industrial context, the company which provides one part of the transformer is not necessary the same than the one which provides the other part. As a result, the interoperability between the two parts is a crucial point. It is studied for the electrical specifications. In power electronics, a current supply is to be loaded with a voltage one and vice-versa. Dealing with the compensation topologies and the control of the transformer, this criterion can be met even if one compensation of the two parts is imposed. However, the geometry of the coils must be able to be magnetically coupled with the other one. This point is a good perspective for a future development.

- *Integration of the efficiency of the power electronics in the choice of the operating frequency* : The efficiency of the transformer is computed without taking into account the efficiency of its electronics. However, the efficiency of the power inverter and rectifier is also function of the frequency. In order to enhance the validity of the modelling and in particular the choice of the operating frequency, these elements could be integrated in the study.

- *Thermal modelling* : In this work, the current density in the optimisation is limited in order to avoid heating the system. Although the losses in the shielding are computed, a thermal modelling seems to be suitable in order to prevent the system from overheating. Moreover, such a multi-physics modelling could be integrated in the optimisation process.

A Optimisation Algorithms

A.1 Introduction

The aim of this section is to introduce several optimization methodologies in order to find the minimum of a function defined by the modelling.

A general optimisation problem can be expressed as suggested in (A.1). The n free variables are contained in the vector $\vec{X}$. The n dimensional domain of optimisation vector is defined as $\mathbb{D}^n$. The objective function F is always to be minimized in an optimisation problem under the p inequalities and equality constraints defined by the function C_i. If the objective function is to be optimized, the simple transformation $F := -F$ is very often used.

$$
\begin{cases}
\vec{X}_{opt}|F(\vec{X}_{opt}) = \min(F(\vec{X})) \text{ with } \vec{X} = \{x_1 \cdots x_n\} \, , \, \vec{X} \in \mathbb{D}^n \\[2mm]
\quad C_i(\vec{X}) = 0 \text{ with } i \in [0, p - p'] \\[2mm]
\quad C_i(\vec{X}) \leq 0 \text{ with } i \in [p - p', p]
\end{cases}
\tag{A.1}
$$

An example of an unidimensional optimisation problem is illustrated in Fig. A.1. The objective function F can be evaluated on the domain $\mathbb{D}$. Indeed, the parameter x_1 is comprised between X_{min} and X_{max}. This example function has three local minima and one global minimum. The aim of an optimisation algorithm is to find the global minimum despite the eventual local minima.

Since the values and ranges of the free parameters can be widely different, they are normalised between 0 and 1. The used normalisation transformation is shown in (A.2).

$$
x_i := \frac{x_i - X_{min,i}}{X_{max,i} - X_{min,i}}
\tag{A.2}
$$

Sometimes, more than one function is to be minimized. This is the so-called multi-objective optimisation. Two main ways exist to generalize the mono-objective optimisation into a multi-objective
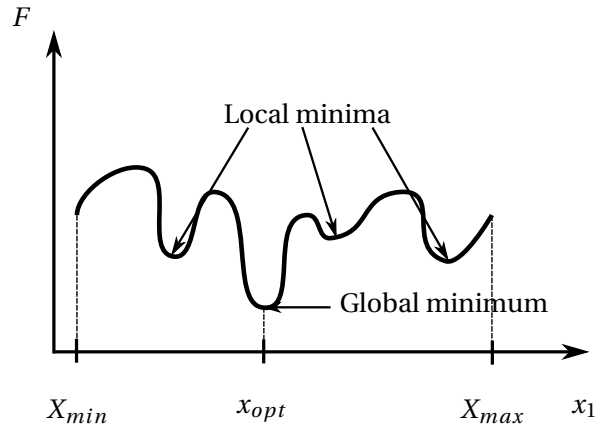
Figure A.1: A one dimensional example of function to optimise

one.

The first methodology consists in combining all the objectives functions into a single one. The transformation is proposed in (A.3). All the objectives function F_i are first normalized with a reference value $F_{i,ref}$ in order to be able to be compared. Then, all the normalized objectives functions are multiplied by a coefficient α_i. This latter sorts the objective functions by their importance. If all the objectives functions have the same importance, $\alpha_i = \frac{1}{m} \forall i \in [1, m]$.

$$F = \sum_{i=1}^{m} \alpha_i \frac{F_i}{F_{i,ref}} \quad \text{with} \quad \sum_{i=1}^{m} \alpha_i = 1 \tag{A.3}$$

The main advantages of this solution is its simplicity. However, the convergence depends on the choice of the coefficient α_i. The importance of all the objectives functions has to be quantified before running the optimisation process.

Another solution consists in ranking the solutions keeping all the objectives functions. This is the so-called Pareto optimality. An example of pareto optimality with two objective functions F_1 and F_2 is given in Fig. A.2. Each square represents a solution evaluated by the optimizer. The black ones represent the set of optimal solutions.

The black line represents the so-called Pareto frontier. It means that all the points in this frontier can not be dominated by any other point.

In terms of Pareto optimality, a solution A dominates a solution B only if the solution A gives better results for all objective functions. Obviously, a solution B dominates a solution A if the solution B gives better results for all objectives functions.

Basically, an optimisation tool is based on two main parts. The first one, called the builder, evaluates the solution for the parameters received. The second part is the optimisation tool, which consists in generating the set of parameters to be evaluated by the builder. This is illustrated in Fig. A.3.

126

Figure A.2: An example of Pareto optimality
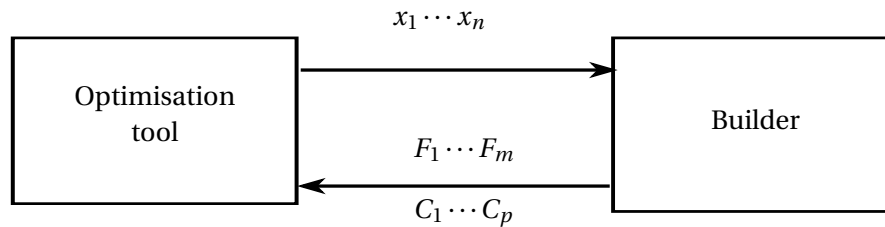
Figure A.3: The main parts of an optimisation process

The optimisation techniques can be divided into two main classes. The first one is called deterministic methods. The results of such a method is strongly dependant of the initial conditions. It generally requires less number of evaluations of the objective function, but it is sensitive to the local minima. The most well-known algorithm of this family is the gradient method. The second family is called stochastic methods. Each execution of such a method leads to a different way to the optimal solution. Some well-know algorithm are the Genetic Algorithm, Particular Swarm Optimisation, ...

A.2 Description of the genetic optimisation algorithm

The main algorithm used for the optimisations undertaken is the Genetic Algorithm. The main phases of this algorithm are shown in Fig. A.4.

1. The initial population is first created. It is generally randomly generated.

2. The initial population is then evaluated by the builder which returns, for each individual, the evaluation of the objective functions ($\vec{F}$), and the constraints vector ($\vec{C}_1$).

3. The evaluated solutions are classified. The genetic operators are applied and leads to a new population.

4. The new population generated by the reproduction process is evaluated by the builder and returns the objective functions and the constraints vector. If the stopping criteria are met, the optimisation is finished. Otherwise, the process runs again the step 4.

127

In order to get the Pareto frontier at the end of the optimisation, all the individuals of each generation are saved.
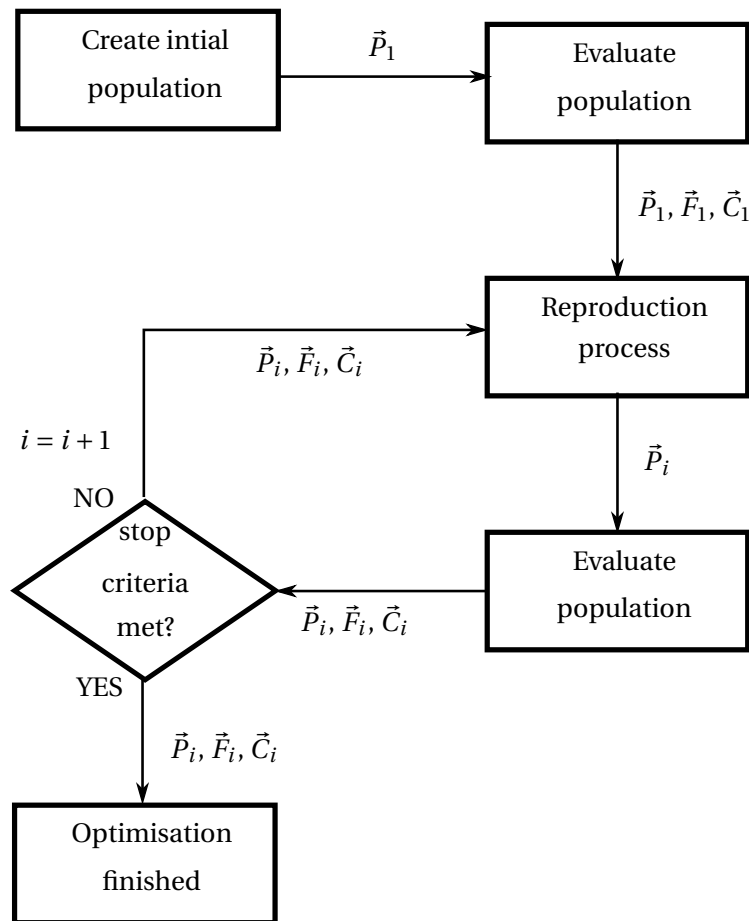
Figure A.4: The main steps of the genetic algorithm

B Methodologies to measure mutual inductances

In this section, two well-known methodologies to measure the mutual inductance of a transformer are presented.

The first one is used when the mutual inductance is measured with a LCR-meter. It can be divided in two steps :

1. The two coils are plugged in series as suggested in Fig. B.1a. The equivalent inductance L_A is measured.

2. The two coils are plugged in series but inverted compared to the previous step as suggested in Fig. B.1b. The equivalent inductance L_B is measured.

(a) Measurement of L_A (b) Measurement of L_B
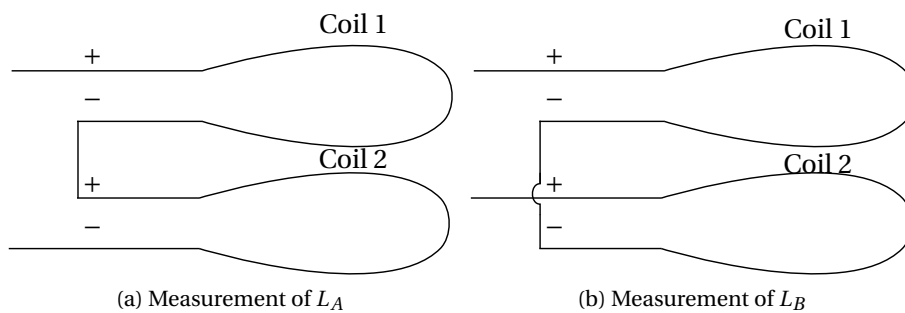
Figure B.1: Connections to measure the mutual inductance

The expressions of L_A and L_B are given in (B.1). The expression of the mutual inductance M can be directly deduced from L_A and L_B, as suggested in (B.2).

$$\begin{cases} L_A = L_1 + L_2 + 2M \\ L_B = L_1 + L_2 - 2M \end{cases} \tag{B.1}$$

$$M = \frac{L_A - L_B}{4} \tag{B.2}$$

The second one is generally used directly on the transformer plugged on its associated electronics. The load is disconnected and the voltage across the secondary coil is measured. The expression of the mutual inductance is given in (B.3).

$$M = \frac{U_{in}}{\omega I_1} \tag{B.3}$$

Nomenclature

List of symbols

Symbol	Unit	Description
α	-	Phase shift for PSM command.
δ	m	Skin depth.
R'_2	Ω	Reflected secondary coil resistance.
μ_0	$H \cdot m^{-1}$	Vacuum permeability.
μ_r	-	Relative magnetic permeability.
μ	$H \cdot m^{-1}$	magnetic permeability.
ω_0	$rad \cdot s^{-1}$	Resonant pulsation.
ω	$rad \cdot s^{-1}$	Pulsation.
Φ	Wb	Magnetic flux.
Ψ	Wb	Total magnetic flux.
$\tan\delta$	-	Dissipation factor of a capacitance.
ρ	$\Omega \cdot m$	Electrical resistivity.
φ_{inv}	-	Phase between the inverter current and voltage .
a_1	m	Radius of the primary wire.
a_2	m	Radius of the secondary wire.
B_{sat}	T	Magnetic flux saturation value.
B	T	Magnetic flux density.
C_1	F	Primary compensation capacitance.
C_2	F	Secondary compensation capacitance.
C_f	F	Filter capacitance.
$C_{2;sp}$	F	Secondary compensation capacitance, SP topology.
$C_{2;ss}$	F	Secondary compensation capacitance, SS topology.

Nomenclature

D		Displacement field.
e_p	m	Thickness of the iron plate.
E	V·m^{-1}	Electric field.
f_0	Hz	Resonant frequency.
ff	-	Fill factor of the coil.
f	Hz	Frequency.
H	A·m^{-1}	Magnetic field.
I_{bat}	A	Battery DC current.
I_{DC}	A	DC supply current.
i_{inv}	A	Inverter current.
J_{max}	A·m^2	Maximal admissible current density.
J	A·m^2	Current density.
K	-	Gain of the ideal transformer.
k	-	Magnetic coupling factor.
L_1	H	Primary self inductance.
L_2	H	Secondary self inductance.
$L_{2;sp}$	H	Secondary self inductance, SP topology.
$L_{2;ss}$	H	Secondary self inductance, SS topology.
L_{eq}	H	Equivalent inductance.
L_f	H	Filter inductance.
l	m	Length of the conductor.
M	H	Mutual inductance.
m	kg	Mass.
N_1	-	Number of turns of the primary coil.
N_2	-	Number of turns of the secondary coil.
$N_{2;sp}$	-	Number of turns of the secondary coil, SP topology.
$N_{2;ss}$	-	Number of turns of the secondary coil, SS topology.
N_{layer}	-	Number of coil layers.
N	-	Number of turns.
P_L	W	Load power.
P_{DC}	W	Supply power.

P_{inv}	W	Inverter power.
P_{in}	W	Input power.
$P_{loss,eddy}$	W	Eddy current losses.
$P_{loss,hyst}$	W	Hysteresis losses.
$P_{LOSS,STAT}$	W	Static losses of the switch.
P_{loss}	W	Joule losses.
Q_1	-	Quality factor of the primary side.
Q_2	-	Quality factor of the secondary side.
Q	-	Quality factor.
R_1	Ω	Primary serial resistance.
R_2	Ω	Secondary serial resistance.
R_L	Ω	Load resistance.
R_r	Ω	Resistance of the relay.
$R_{2;sp}$	Ω	Secondary serial resistance, SP topology.
$R_{2;ss}$	Ω	Primary serial resistance, SS topology.
R_{eq}	Ω	Equivalent resistance.
r_f	m	Radius of the ferrite plate.
r_{int}	m	Internal radius of circular coil.
r_p	m	Radius of the iron plate.
R	Ω	Electrical resistance.
r	m	Radius of the conductor.
S	m^2	Surface of the conductor.
T_{shift}	s	Shift time.
T	s	Period.
t	s	Time.
U_{bat}	V	Battery DC voltage.
u_{inv}	V	Inverter voltage.
$V_{CE,SAT}$	V	Collector-Emitter saturation voltage.
V	m^3	Volume.
η	-	Efficiency.
$\cos(\phi)$	-	Power factor.

Mathematical operators

Symbol	Description
$\underline{x}$	complex number.
$\mathrm{Im}(x)$	Imaginary part of x.
$\hat{x}$	peak value of the function $x(t)$.
$\mathrm{Re}(x)$	Real part of x.
Δ	Discriminant.
e	Euler's number.
j	Complex imaginary unit.
$\vec{\nabla}\cdot$	Divergence.
$\vec{\nabla}\times$	Rotational.

Bibliography

[1] http://www.epcos.com.

[2] C. Auvigne, P. Germano, D. Ladas, and Y. Perriard. A dual-topology icpt applied to an electric vehicle battery charger. In *Electrical Machines (ICEM), 2012 XXth International Conference on*, pages 2287 –2292, sept. 2012.

[3] E.J. Barbeau. *Polynomials.* Problem Books in Mathematics. Springer New York, 2003.

[4] T. Bieler, M. Perrottet, V. Nguyen, and Y. Perriard. Contactless power and information transmission. In *Industry Applications Conference, 2001. Thirty-Sixth IAS Annual Meeting. Conference Record of the 2001 IEEE*, volume 1, pages 83–88 vol.1, Sept 2001.

[5] T. Bieler, M. Perrottet, V. Nguyen, and Y. Perriard. Contactless power and information transmission. *Industry Applications, IEEE Transactions on*, 38(5):1266 – 1272, sep/oct 2002.

[6] W. Brown, J. Mims, and N. Heenan. An experimental microwave-powered helicopter. In *IRE International Convention Record*, volume 13, pages 225–235, March 1965.

[7] William C. Brown. Experiments involving a microwave beam to power and position a helicopter. *Aerospace and Electronic Systems, IEEE Transactions on*, AES-5(5):692–702, Sept 1969.

[8] M. Budhia, G. Covic, and J. Boys. A new ipt magnetic coupler for electric vehicle charging systems. In *IECON 2010 - 36th Annual Conference on IEEE Industrial Electronics Society*, pages 2487–2492, 2010.

[9] M. Budhia, G.A. Covic, and J.T. Boys. Design and optimization of circular magnetic structures for lumped inductive power transfer systems. *Power Electronics, IEEE Transactions on*, 26(11):3096 –3108, nov. 2011.

[10] M. Budhia, G.A. Covic, J.T. Boys, and Chang-Yu Huang. Development and evaluation of single sided flux couplers for contactless electric vehicle charging. In *Energy Conversion Congress and Exposition (ECCE), 2011 IEEE*, pages 614–621, 2011.

[11] Xia Chen-yang, Li Chao-wei, and Zhang Juan. Analysis of power transfer characteristic of capacitive power transfer system and inductively coupled power transfer system. In *Mechatronic Science, Electric Engineering and Computer (MEC), 2011 International Conference on*, pages 1281–1285, 2011.

[12] Byungcho Choi, Jaehyun Nho, Honnyong Cha, Taeyoung Ahn, and B. Choi. Design and implementation of low-profile contactless battery charger using planar printed circuit board windings as energy transfer device. *Industrial Electronics, IEEE Transactions on*, 51(1):140–147, 2004.

[13] Wireless Power Consortium. http://www.wirelesspowerconsortium.com/.

Bibliography

[14] G.A. Covic, M.L.G. Kissin, D. Kacprzak, N. Clausen, and Hao Hao. A bipolar primary pad topology for ev stationary charging and highway power by inductive coupling. In *Energy Conversion Congress and Exposition (ECCE), 2011 IEEE*, pages 1832–1838, 2011.

[15] Vernez D. *Analyse de risque lors de la conception de projets novateurs; application au swissmetro.* PhD thesis, Swiss Federal Institute of Technology of Lausanne, 1999.

[16] R. M. Dickinson. Wireless power transmission technology state of the art the first bill brown lecture. *Acta Astronautica*, 53(4-10):561–570, 2003.

[17] Thuc Phi Duong and Jong-Wook Lee. Experimental results of high-efficiency resonant coupling wireless power transfer using a variable coupling method. *Microwave and Wireless Components Letters, IEEE*, 21(8):442–444, 2011.

[18] Jamelot E. *Résolution des équations de Maxwell avec des éléments finis de Galerkin continus.* PhD thesis, Ecole nationale Supérieure des Techniques Avancées, 2015.

[19] EPCOS. http://www.epcos.com/inf/85/ds/00160017.pdf.

[20] Huang Fan and Wang Jianqiang. Investigation on full bridge inductively coupled power transfer system. In *Power Electronics and Motion Control Conference (IPEMC), 2012 7th International*, volume 3, pages 1737–1740, 2012.

[21] J.P. Ferrieux and F. Forest. *Alimentations à découpage, convertisseurs à résonance: principes, composants, modélisation.* Collection Sciences sup. Dunod, 2006.

[22] Alliance for Wireless Power. http://www.rezence.com/technology/technical-specification.

[23] P Germano and M Jufer. Contactless power transmission: Frequency tuning by a maximum power tracking method. *EPE*, 1997.

[24] P. Germano, I. Stefanini, and Y. Perriard. Contactless system dedicated to colic stimulation. In *Electrical Machines, 2008. ICEM 2008. 18th International Conference on*, pages 1–5, 2008.

[25] Yuantai Hu, X. Zhang, Jiashi Yang, and Qing Jiang. Transmitting electric energy through a metal wall by acoustic waves using piezoelectric transducers. *Ultrasonics, Ferroelectrics and Frequency Control, IEEE Transactions on*, 50(7):773–781, 2003.

[26] S.Y. Hui. Planar wireless charging technology for portable electronic products and qi. *Proceedings of the IEEE*, 101(6):1290–1301, 2013.

[27] S.Y.R. Hui and W.W.C. Ho. A new generation of universal contactless battery charging platform for portable consumer electronic equipment. *Power Electronics, IEEE Transactions on*, 20(3):620–627, 2005.

[28] Stefanini I. *Méthodologie de conception et optimisation d'actionneurs intégrés sans fer.* PhD thesis, Swiss Federal Institute of Technology of Lausanne, 2006.

[29] ICNRP. Icnirp guidelines for limiting exposure to time-varying electric, magnetic and electromagnetic fields (up to 300 ghz), 1998.

[30] Radio Frequency identification standards. http://www.impinj.com/resources/about-rfid/rfid-standards/.

[31] Jian-Ming Jin. *The finite element method in electromagnetics.* IEEE Press, 2014.

[32] M. Jufer. *Traité d'électricité: électromécanique.* Traité d'électricité. Presses Polytechniques Romandes, 1995.

[33] M.P. Kazmierkowski and A.J. Moradewicz. Contactless energy transfer (cet) systems; a review. In *Power Electronics and Motion Control Conference (EPE/PEMC), 2012 15th International*, pages Session 3–1–Session 3–6, 2012.

[34] M.L.G. Kissin, J.T. Boys, and G.A. Covic. Interphase mutual inductance in polyphase inductive power transfer systems. *Industrial Electronics, IEEE Transactions on*, 56(7):2393–2400, 2009.

[35] M.L.G. Kissin, G. A. Covic, and J. T. Boys. Estimating the output power of flat pickups in complex ipt systems. In *Power Electronics Specialists Conference, 2008. PESC 2008. IEEE*, pages 604–610, 2008.

[36] M. Kline, I. Izyumin, B. Boser, and S. Sanders. Capacitive power transfer for contactless charging. In *Applied Power Electronics Conference and Exposition (APEC), 2011 Twenty-Sixth Annual IEEE*, pages 1398–1404, 2011.

[37] D. Ladas, Y. Perriard, C. Auvigne, and P. Germano. Energy conversion system, July 2 2014. EP Patent App. EP20,130,181,857.

[38] R. Laouamer, M. Brunello, J.P. Ferrieux, O. Normand, and N. Buchheit. A multi-resonant converter for non-contact charging with electromagnetic coupling. In *Industrial Electronics, Control and Instrumentation, 1997. IECON 97. 23rd International Conference on*, volume 2, pages 792–797 vol.2, nov 1997.

[39] T.J. Lawry, K.R. Wilt, J.D. Ashdown, H.A. Scarton, and G.J. Saulnier. A high-performance ultrasonic system for the simultaneous transmission of data and power through solid metal barriers. *Ultrasonics, Ferroelectrics and Frequency Control, IEEE Transactions on*, 60(1):194–203, 2013.

[40] J.L.-W. Li. Wireless power transmission: State-of-the-arts in technologies and potential applications (invited paper). In *Microwave Conference Proceedings (APMC), 2011 Asia-Pacific*, pages 86–89, Dec 2011.

[41] Chao Liu, A.P. Hu, and N.C. Nair. Coupling study of a rotary capacitive power transfer system. In *Industrial Technology, 2009. ICIT 2009. IEEE International Conference on*, pages 1–6, 2009.

[42] D.C. Ludois, J.K. Reed, and K. Hanson. Capacitive power transfer for rotor field current in synchronous machines. *Power Electronics, IEEE Transactions on*, 27(11):4638–4645, 2012.

[43] M. Markovic and Y. Perriard. Eddy current power losses in a toroidal laminated core with rectangular cross section. In *Electrical Machines and Systems, 2009. ICEMS 2009. International Conference on*, pages 1–4, 2009.

[44] H. Matsuki, M. Shiiki, K. Murakami, K. Nadehara, and T. Yamamoto. Flexible transcutaneous transformer for artificial heart system. *Magnetics, IEEE Transactions on*, 26(5):1548–1550, Sep 1990.

[45] H. Matsuki, M. Shiiki, K. Murakami, and T. Yamamoto. Investigation of coil geometry for transcutaneous energy transmission for artificial heart. *Magnetics, IEEE Transactions on*, 28(5):2406–2408, 1992.

[46] R. Mecke, C. Rathge, A Ecklebe, and A Lindemann. Bidirectional switches for matrix converter in contactless energy transmission systems. In *Power Electronics and Applications, 2005 European Conference on*, pages 10 pp.–P.10, 2005.

[47] B. Multon. Modeles electriques du transformateur electromagnetique.

[48] OLEV. http://olevtech.com/.

Bibliography

[49] Meyer P. *Modeling of Inductive Contactless Energy Transfer Systems*. PhD thesis, Swiss Federal Institute of Technology of Lausanne, 2012.

[50] Mi-Hyun Park, Eun-Gyeong Shin, Heung-Reol Lee, and In-Soo Suh. Dynamic model and control algorithm of hvac system for olev; application. In *Control Automation and Systems (ICCAS), 2010 International Conference on*, pages 1312–1317, Oct 2010.

[51] Power By Proxy. http://powerbyproxi.com/.

[52] S. Raabe, G. A J Elliott, G. A. Covic, and J. T. Boys. A quadrature pickup for inductive power transfer systems. In *Industrial Electronics and Applications, 2007. ICIEA 2007. 2nd IEEE Conference on*, pages 68–73, 2007.

[53] D.E. Raible, D. Dinca, and T.H. Nayfeh. Optical frequency optimization of a high intensity laser power beaming system utilizing vmj photovoltaic cells. In *Space Optical Systems and Applications (ICSOS), 2011 International Conference on*, pages 232–238, 2011.

[54] Hassani S. *Integration de l'hysteresis magnetique dans un calcul elements finis en vue de l'estimation des pertes dans les toles de machines electriques*. PhD thesis, Universite Mouloud Mammerie, Tizi-ouzou, 2010.

[55] A. Sahai and D. Graham. Optical wireless power transmission at long wavelengths. In *Space Optical Systems and Applications (ICSOS), 2011 International Conference on*, pages 164–170, 2011.

[56] B. Schmuelling, S.G. Cimen, T. Vosshagen, and F. Turki. Layout and operation of a non-contact charging system for electric vehicles. In *Power Electronics and Motion Control Conference (EPE/PEMC), 2012 15th International*, pages LS4d.4–1–LS4d.4–7, 2012.

[57] Jaegue Shin, Boyune Song, Seokhwan Lee, Seungyong Shin, Yangsu Kim, Guho Jung, and Seongjeub Jeon. Contactless power transfer systems for on-line electric vehicle (olev). In *Electric Vehicle Conference (IEVC), 2012 IEEE International*, pages 1–4, March 2012.

[58] Naoki Shinohara. *Wireless power transfer via radiowaves*. ISTE. Wiley, Hoboken, NJ, 2014.

[59] Z. Sienkiewicz. Biological effects of electromagnetic fields and radiation. In *Electromagnetic Compatibility, 1994., Ninth International Conference on*, pages 17–21, 1994.

[60] Boyune Song, Jaegue Shin, Sanghoon Chung, Seungyong Shin, Seokhwan Lee, Yangsu Kim, Guho Jung, and Seongjeub Jeon. Design of a pickup with compensation winding for on-line electric vehicle (olev). In *Wireless Power Transfer (WPT), 2013 IEEE*, pages 60–62, May 2013.

[61] Boyune Song, Jaegue Shin, Seokhwan Lee, Seungyong Shin, Yangsu Kim, Sungjeub Jeon, and Guho Jung. Design of a high power transfer pickup for on-line electric vehicle (olev). In *Electric Vehicle Conference (IEVC), 2012 IEEE International*, pages 1–4, March 2012.

[62] C. Sonntag, E.A. Lomonova, and J.L. Duarte. Variable-phase contactless energy transfer desktop part i: Design. In *Electrical Machines and Systems, 2008. ICEMS 2008. International Conference on*, pages 4460–4465, 2008.

[63] C. Sonntag, E.A. Lomonova, J.L. Duarte, and A. J A Vandenput. Specialized receivers for three-phase contactless energy transfer desktop applications. In *Power Electronics and Applications, 2007 European Conference on*, pages 1–11, 2007.

[64] Christoph Sonntag. *Contactless Energy Transfer Platform using Air-cored Planar Inductors*. PhD thesis, Eindhoven University of Technology, 2010.

[65] STmicroelectronics. A single plate induction cooker, an2383.

[66] R.L. Stoll. *The analysis of eddy currents*. Monographs in electrical and electronic engineering. Clarendon Press, 1974.

[67] D. van Wageningen and T. Staring. The qi wireless power standard. In *Power Electronics and Motion Control Conference (EPE/PEMC), 2010 14th International*, pages S15–25–S15–32, 2010.

[68] J.L. Villa, A. Llombart, J.F. Sanz, and J. Sallan. Practical development of a 5 kw icpt system ss compensated with a large air gap. In *Industrial Electronics, 2007. ISIE 2007. IEEE International Symposium on*, pages 1219–1223, 2007.

[69] Chwei-Sen Wang, G.A. Covic, and O.H. Stielau. General stability criterions for zero phase angle controlled loosely coupled inductive power transfer systems. In *Industrial Electronics Society, 2001. IECON '01. The 27th Annual Conference of the IEEE*, volume 2, pages 1049 –1054 vol.2, 2001.

[70] Chwei-Sen Wang, O.H. Stielau, and G.A. Covic. Power transfer capability and bifurcation phenomena of loosely coupled inductive power transfer systems. *Industrial Electronics, IEEE Transactions on*, 51(1):148 – 157, feb. 2004.

[71] C. Winter, C. Auvigne, and Y. Perriard. Design of a resonant power inverter for a piezoelectric actuator. In *IECON 2012 - 38th Annual Conference on IEEE Industrial Electronics Society*, pages 345–349, 2012.

[72] WiTricity. http://www.witricity.com/.

[73] Di Wu, Hao Chen, T. Das, and D.C. Aliprantis. Bidirectional power transfer between hevs and grid without external power converters. In *Energy 2030 Conference, 2008. ENERGY 2008. IEEE*, pages 1–6, Nov 2008.

[74] H.H. Wu, AP. Hu, P. Si, D. Budgett, C. Tung, and S. Malpas. A push-pull resonant converter with dual coils for transcutaneous energy transfer systems. In *Industrial Electronics and Applications, 2009. ICIEA 2009. 4th IEEE Conference on*, pages 1051–1056, May 2009.

[75] Yong Xiang Xu, J.T. Boys, and G.A. Covic. Modeling and controller design of icpt pick-ups. In *Power System Technology, 2002. Proceedings. PowerCon 2002. International Conference on*, volume 3, pages 1602 – 1606 vol.3, 2002.

[76] Zhongming Ye, P.K. Jain, and P.C. Sen. Dual-edge phase-shift-modulation for circulating current control in full-bridge resonant converters. In *Applied Power Electronics Conference and Exposition, 2008. APEC 2008. Twenty-Third Annual IEEE*, pages 1041–1047, 2008.

[77] Z.M. Ye, P.K. Jain, and P.C. Sen. A full bridge resonant inverter with modified phase shift modulation. In *Power Electronics Specialists Conference, 2005. PESC '05. IEEE 36th*, pages 642 –649, june 2005.

[78] H. Zheng, K. Tnay, N. Alami, and A. P. Hu. Contactless power couplers for respiratory devices. In *Mechatronics and Embedded Systems and Applications (MESA), 2010 IEEE/ASME International Conference on*, pages 155–160, 2010.

[79] Wenxing Zhong, Chi Kwan Lee, and S. Y R Hui. General analysis on the use of tesla's resonators in domino forms for wireless power transfer. *Industrial Electronics, IEEE Transactions on*, 60(1):261–270, Jan 2013.

Curriculum Vitae

Christophe AUVIGNE

Born November 6th, 1987

French Citizen

christophe.auvigne@a3.epfl.ch

Studies and professional experience

2011 - 2015	Teaching assistant and PhD student at the Integrated Actuators Laboratory (LAI), École polytechnique fédérale de Lausanne, Switzerland
2009 - 2011	Master of Science in Microengineering, École polytechnique fédérale de Lausanne, Switzerland
2006 - 2009	Bachelor of Science in Microengineering, École polytechnique fédérale de Lausanne, Switzerland
2003 - 2006	Bac scientifique, Lycée international de Ferney Voltaire, France

Personal skills and experiences

- Programming : C,C++,C-sharp, java, python, jython, assembly, VHDL, visual basic

- Hobbies : electronics hacking, trail running (2014 ultra trail of Verbier finisher, 2014 SainteLyon finisher,...), mountaineering, ski touring, climbing, swimming, cycling, playing the guitar and the saxophone

Publications

- C. Auvigne, F. Copt, C. Winter, Y. Perriard, "Study of Various Winding Topologies for Self-Shielding Induction Cookers", Journal of International Conference on Electrical Machines and Systems (JICEMS), Volume 2, Number 4, December 2013

- R. Besuchet, C. Auvigne, D. Shi, C. Winter, Y. Civet, Y. Perriard, "Optimisation of an Inductive Power Transfer Structure", Journal of International Conference on Electrical Machines and Systems (JICEMS), Volume 2, Number 3, September 2013

- C. Auvigne, P. Germano, D. Ladas, Y. Perriard, "About tuning capacitance in inductive coupled power transfer", Power Electronics and Applications (EPE 2013), Proceedings of the 2011-15th European Conference on, September 2013

- C. Auvigne, P. Germano, D. Ladas, Y. Perriard, "A dual-topology ICPT applied to an electric vehicle battery charger", Electrical Machines 2012, XXth International Conference On, sept. 2012

- C. auvigne, P. Germano, Y. Civet, Y. Perriard, "Design considerations for a contactless battery charger", Power Electronics and Applications (EPE 2014), Proceedings of the 2011-15th European Conference on, September 2014

- F. Copt, C. Auvigne, C. Winter, Y. Perriard, "A Novel winding topology applied for a self-shielding induction cooker", International Conference on Electrical Machines and Systems (ICEMS) 2013, October 2013

- D. Shi, C. Auvigne, R. Besuchet, C. Winter, Y. Civet, Y. Perriard, "Optimal design of inductive coupled power transfer systems with applications to electric cars", International Conference on Electrical Machines and Systems (ICEMS) 2013, October 2013

- C. Winter, C. Auvigne, Y. Perriard, "Design of a resonant power inverter for a piezoelectric actuator", IECON 2012 - 38th Annual Conference on IEEE Industrial Electronics Society, Pages 345-349, October 2012

Patent

- D. Ladas, Y. Perriard, C. Auvigne and P. Germano, Energy conversion system, July 2 2014, EP Patent App. EP20,130,181,857